OSAKA UNIVERSITY

DOCTORAL THESIS

Development of Current Noise Measurement System and Non-equilibrium Transport in Quantum Hall Effect

Author:
Sanghyun LEE

Supervisor:
Dr. Kensuke KOBAYASHI

A thesis submitted in fulfillment of the requirements for the degree of Doctor of Physics

in the

Kobayashi Group
Department of Science

Acknowledgments

First, I wish to express my deepest gratitude to Professor Kensuke Kobayashi for his unending guidance and scientific discussions since I belong to his group. I also want to appreciate Professor Yasuhiro Niimi for his encouragement and suggestions. I would like to thank to Professor Tomonori Arakawa for his discussion of physics and technical support.

Quantum Solid State Physics Research Group in NTT Basic Research Laboratories in Japan and Quantum Nano-electronics Laboratories in POSTECH in the Republic of Korea have helped overall research. I appreciate the Interactive Materials Science CADET Program at Osaka University for these collaboration.

The research described in Chapter 5 is collaborated with Quantum Solid State Physics Research Group. I wish to extend my special thanks to Dr. Koji Muraki, who permits the collaboration, and Dr. Masayuki Hashisaka, who helps the research and inspires me. I want to thank the members of the group.

Researchers at Quantum Nano-electronics Laboratories have supported me the fabrication of high-quality graphene for the studies in the Chapter 6. I wish to extend my special thanks to Professor Hu-Jong Lee and Professor Gil-Ho Lee. I greatly appreciated the assistance provided by Mr. SeungHyun Shin. I want to thank the members of the group.

I am grateful to those whom I have had the pleasure of noise measurement, especially Professor Meydi Ferrier, Dr. Hata, and Fujiwara-san.

Finally, I would like to thank the Kobayashi group members in the Department of Physics, Graduate School of Science, Osaka University.

Contents

Chapter 1

Foreword

Mesoscopic systems have served as an important experimental platform for studying the quantum and correlated nature of electronic systems. Various quantum effects have been investigated by measuring their transport properties. In particular, since Klaus von Klitzing observed the quantum Hall effect (QHE) [1], many researchers have focused on the effect to investigate numerous physical characteristics, such as edge states and topological insulators. The quantum Hall effect breakdown (QHEBD), which occurs when a high electric field or bias current is applied to the sample, is a significant effect to understand the non-equilibrium state of the effect. More experimental results are necessary for complete understanding.

Conductance, G, is often evaluated by measuring dc current that corresponds to the time average of electron number passing through a device. Besides, the current noise, which corresponds to the fluctuation of the current, is useful for gaining more in-depth insight into quantum transport [2–4]. For example, the noise measurements have successfully revealed the fractional charge of tunneling quasiparticles in fractional quantum Hall systems [5–8] and correlated electron transport through Kondo impurities [9–12]. The measurement method is suggested to probe novel mesoscopic phenomena, such as anyonic correlations in fractional quantum Hall systems [13, 14] and violation of Bell inequalities in an electronic interferometer [15].

In this Thesis, we studied the current noise from two perspectives: measurement technique and physics. First, we developed a noise measurement system for future physical experimental measurements. We succeeded in increasing the gain of the signal from the sample and reducing the external noise. Also, the quantum Hall effect breakdown in a monolayer graphene Hall bar was studied. It is a more potential material than the GaAs/AlGaAs heterostructure because graphene can adjust the carrier type and carrier density. Further, we observed the increases in the temperature of the electrons by analyzing the current noise, which supports one of the theoretical QHEBD models.

This thesis consists of seven chapters. In Chapter 2, we introduce several backgrounds about our research: mesoscopic physics, Landauer-Büttiker formula. We elucidate the theoretical background of the current noise in Chapter 3 and expound on the method of how to measure the current noise in Chapter 4. While Chapter 5 shows our achievement of developing a noise measurement system, Chapter 6 shows the study of a non-equilibrium transport in quantum Hall effect on the graphene Hall bar. The sample comprises

a hBN/monolayer graphene/hBN. In Chapter 7, we summarize the Thesis.

Chapter 2

Mesoscopic Transport

A mesoscopic system is a conductor whose size is shorter than the mean free path or the coherence length of the electrons. In this regime, we study quantum mechanics by manipulating electronic circuits. Here, we briefly introduce Landauer formula, two-dimensional electron gas, and the phenomena in the mesoscopic world.

2.1 Landauer Formula

We briefly introduce the Landauer formula according to Ref. [16].

We consider two-terminal measurement for convenience, as shown in Fig. 2.1. We assume that $+k$ states exist in a single transverse mode according to

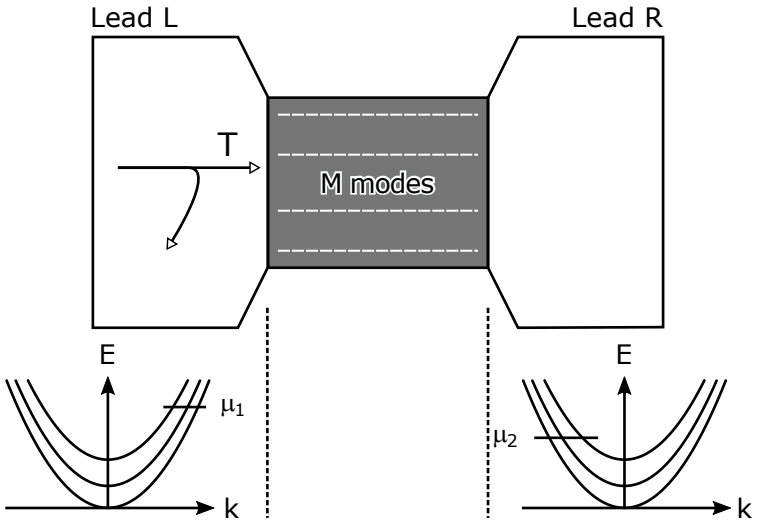

FIGURE 2.1: Schematic diagram for understanding the Landauer formula. A conductor has a transmission probability of $\mathcal{T}$ and M transverse modes [16].

arbitrary function $g(E(+k))$. The current per unit length in a conductor is expressed as

$$I = env, \tag{2.1}$$

where e is the elementary charge, n is the carrier density, and v is the drift velocity. Since the charge density in a conductor of length $\mathcal{L}$ for a single $+k$

state equal to $g(E(+k))/\mathcal{L}$, Eq. (2.1) is expressed as

$$I_{+k} = \frac{e}{\mathcal{L}} \sum_k v g(E(+k)). \tag{2.2}$$

By replacing the sum with the integral, the current is given by

$$I_{+k} = \frac{2e}{h} \int_{\mu_1}^{\infty} g(E(+k)) dE. \tag{2.3}$$

When the M transverse modes exist in the mesoscopic conductor, the current is given by

$$I_{+k} = \frac{2e}{h} \int_{-\infty}^{\infty} g(E(+k)) M(E) dE. \tag{2.4}$$

When the transverse modes are independent of the energy for $\mu_1 < E < \mu_2$, the current is expressed as

$$I = \frac{2e}{h} M \left(\mu_1 - \mu_2\right). \tag{2.5}$$

Assuming the mesoscopic conductor has the transmission probability $\mathcal{T}$, then the transmitted current is expressed as

$$I_{\mathcal{T}} = \frac{2e}{h} M\mathcal{T} \left(\mu_1 - \mu_2\right). \tag{2.6}$$

The conductance is given by

$$G = \frac{I}{\left(\mu_1 - \mu_2\right)/|e|} = \frac{2e^2}{h} M\mathcal{T}. \tag{2.7}$$

Equation (2.7) is called the Landauer Formula.

2.2 Two-Dimensional Electron Gas System

The two-dimensional electron gas (2DEG) is a useful stage for a mesoscopic system, such as the quantum point contact and the quantum Hall effect. The 2DEG appears when the electron is confined in z-direction for some reason. We deal with two types of 2DEG: a semiconductor heterostructure and graphene.

2.2.1 Semiconductor Heterostructure

One of the most used semiconductor heterostructures with a 2DEG system is GaAs/AlGaAs. It was invented by Takashi Mimura and Satoshi Hiyamizu, who researched GaAs high-electron-mobility transistors in Fujitsu Laboratories in 1979 [17, 18]. Figure 2.2 shows the heterostructure of the GaAs/AlGaAs. When the AlGaAs and GaAs are attached, the narrow band gaps of GaAs are bent downward, while the wide band gaps of the AlGaAs are bent upward

due to the wide mismatch of the Fermi energy. The conduction band of the GaAs state obtains a small potential. The electronic wave functions in the potential are confined in the z-direction. Therefore, at the interface between them, a thin two-dimensional conducting layer is formed [16]. Researchers can fabricate high-quality structures with molecular-beam epitaxy.

The Hamiltonian of a free particle is given by

$$\mathcal{H} = \frac{\overrightarrow{p}^2}{2m}, \tag{2.8}$$

where m is the mass of a particle. In 2DEG, since the particle is confined, the Hamiltonian Eq. (2.8) is expressed as

$$\mathcal{H} = \frac{p_x^2}{2m} + \frac{p_y^2}{2m}. \tag{2.9}$$

Thus, the eigenenergy of the Hamiltonian is expressed as

$$E = \frac{\hbar^2}{2m}\left(k_x^2 + k_y^2\right). \tag{2.10}$$

The typical properties of 2DEG is well known. The mobility is about 10^6 cm^2/Vs, the carrier density ranges from 2×10^{11} cm^{-2} to 2×10^{12} cm^{-2}, the mean free path is about 30 μm, and the Fermi wave length is about 40 nm [16].

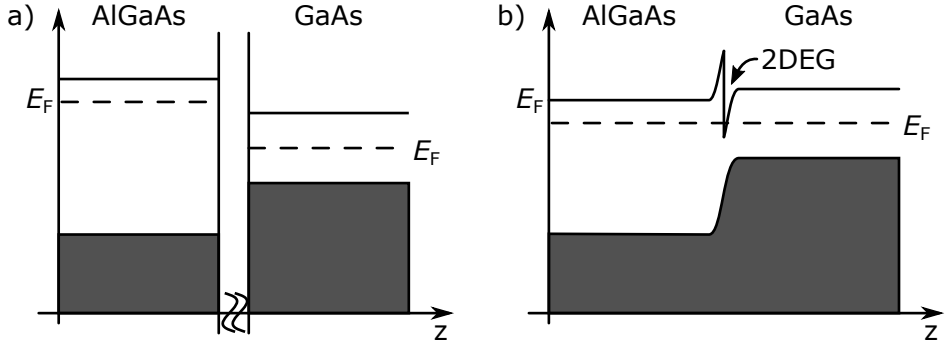

FIGURE 2.2: Schematic diagram of conduction and valence band of the AlGaAs and GaAs. a) Energy bands when AlGaAs and GaAs are far enough apart. b) Energy bands when AlGaAs and GaAs are attached. A thin two-dimensional conducting layer is formed at GaAs conduction band [16].

2.2.2 Graphene

We briefly introduce graphene according to Refs. [19–24]. A monolayer graphene is a single layer comprising carbon atoms in a honeycomb lattice. Figure 2.3 a) shows the schematic of graphene. The electrons in $2s$, $2p_x$, $2p_y$, and $2p_z$ orbitals significantly act for graphene structure. The $2s$, $2p_x$, and $2p_y$ comprising a sp^2 hybridization form a σ band, the $2p_z$ orbital forms a

half-filled π band. The σ band leads to a planar structure to bond the carbon atoms, while the perpendicular π band leads to the conduction of the electrons, hopping to the nearest neighbor.

We will detail the band structure of the graphene because it is particular. The lattice vectors [see Fig. 2.3 a)] can be written as

$$\overrightarrow{a_1} = \left(\sqrt{3}a, 0\right), \qquad \overrightarrow{a_2} = \left(\frac{\sqrt{3}a}{2}, \frac{3a}{2}\right), \tag{2.11}$$

where $a \simeq 1.42$ Å is the lattice distance. The reciprocal-lattice vectors are given by

$$\overrightarrow{b_1} = \left(\frac{2\pi}{\sqrt{3}a}, -\frac{2\pi}{3a}\right), \qquad \overrightarrow{b_2} = \left(0, \frac{4\pi}{3a}\right), \tag{2.12}$$

as shown in Fig. 2.3 b). Of particular importance for the physics of graphene are the two points, K and K', at the corner of the graphene Brillouin zone. These are named Dirac points for reasons that will become clear later. Their positions in the vector space are given by

$$\overrightarrow{K} = \left(\frac{4\pi}{3\sqrt{3}a}, 0\right), \qquad \overrightarrow{K'} = \left(-\frac{4\pi}{3\sqrt{3}a}, 0\right) \tag{2.13}$$

at the corner of the Brillouin zone, as shown in Fig. 2.3 b). We will explain the band structure using the tight-binding model. A trial wave function, Ψ^k, is expressed as

$$\left|\Psi^k\right\rangle = C^{\mathrm{A}}\left|\psi^{\mathrm{A}}\right\rangle + C^{\mathrm{B}}\left|\psi^{\mathrm{B}}\right\rangle, \qquad \left\langle\Psi^k\middle|\,\overrightarrow{r}\right\rangle = \Psi^k\left(\overrightarrow{r}\right), \tag{2.14}$$

where k is the wave vector, $\psi^{\mathrm{A(B)}}$ is the wave function on the A(B) atom, and $C^{\mathrm{A(B)}}$ is the eigenfunctions for the coefficients. According to Bloch's theorem, the $\left|\psi^{\mathrm{A(B)}}\right\rangle$ is expressed as

$$\left|\psi^{\mathrm{A(B)}}\right\rangle = \frac{1}{\sqrt{N}}\sum_j \exp\left(ik\overrightarrow{R}_j^{\mathrm{A(B)}}\right)\left|\phi^{\mathrm{A(B)}}\right\rangle, \tag{2.15}$$

where N is the number of elementary cells, R_j is the Bravais lattice site, and ϕ is the wave function of p_z orbital of carbon atoms, $\left\langle\phi_j^{\mathrm{A(B)}}\middle|\,\overrightarrow{r}\right\rangle = \phi\left(\overrightarrow{r} - \overrightarrow{R}_j^{\mathrm{A(B)}}\right)$. The Schrödinger equation, $\mathcal{H}\left|\Psi^k\right\rangle = E\left|\Psi^k\right\rangle$ is expressed as

$$\begin{pmatrix} \varepsilon_0 & tf(k) \\ tf'(k) & \varepsilon_0 \end{pmatrix}\begin{pmatrix} C^{\mathrm{A}} \\ C^{\mathrm{B}} \end{pmatrix} = E\begin{pmatrix} 1 & sf(k) \\ sf'(k) & 1 \end{pmatrix}\begin{pmatrix} C^{\mathrm{A}} \\ C^{\mathrm{B}} \end{pmatrix}, \tag{2.16}$$

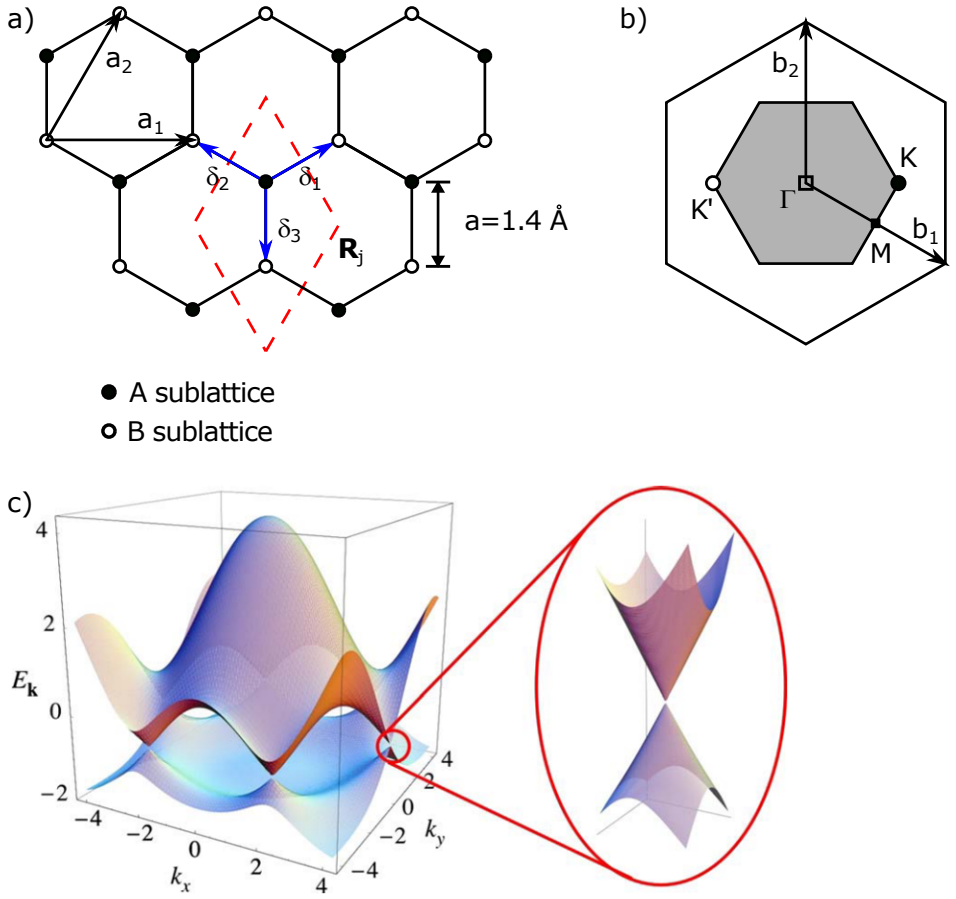

FIGURE 2.3: Schematic diagram of graphene. a) Honeycomb lattice of graphene. Reprinted figure with permission from [23] Copyright 2021 by the American Physical Society. b) Reciprocal lattice of the triangular lattice. Reprinted figure with permission from [23] Copyright 2021 by the American Physical Society. c) Energy dispersion in graphene. Right panel: zoom-in of the energy bands in the vicinity of the Dirac cone. Reprinted figure with permission from [19] Copyright 2021 by the American Physical Society.

where ε_0 is the on-site energy,

$$
\begin{aligned}
&f(k) \equiv \sum_{j=1,2,3} \exp(i\,\overrightarrow{k}\cdot\overrightarrow{\delta_j}),\\
&\delta_1 = \frac{a}{2}\left(\sqrt{3},1\right), \quad \delta_2 = \frac{a}{2}\left(-\sqrt{3},1\right), \quad \delta_3 = (0,-a),\\
&\left\langle \phi^{\mathrm{A(B)}} \middle| \mathcal{H} \middle| \phi^{\mathrm{A(B)}} \right\rangle = t, \quad \left\langle \phi^{\mathrm{A(B)}} \middle| \phi^{\mathrm{A(B)}} \right\rangle = s,
\end{aligned}
$$

t is the hopping amplitude between the nearest neighbors $(j,\ \mathrm{A})$ and $(i,\ \mathrm{B})$ [see $(\delta_1, \delta_2, \delta_3)$ in Fig. 2.3 a)], and s is the overlap correction. The energy E is

given by

$$E = \frac{\varepsilon_0 \pm t\,|f(k)|}{1 \pm s\,|f(k)|}. \tag{2.17}$$

Here, $+$ is for the conduction band, π^*, $-$ is for the valence band, π band. According to the numerical calculation [20] or the spectroscopic measurements [21], the hopping amplitude for the next nearest neighbor is neglected and $s \ll 1$. For convenience, we assume that $s \ll 1$ and $\varepsilon_0 = 0$. The energy, E, is expressed as

$$\begin{aligned} E &= \pm t\,|f(k)| \\ &= \pm t\sqrt{3 + 2\cos\left(\sqrt{3}k_x a\right) + 4\cos\left(\frac{\sqrt{3}k_x a}{2}\right)\cos\left(\frac{3k_y a}{2}\right)}. \end{aligned} \tag{2.18}$$

The energy dispersion is shown in Fig. 2.3 c).

In the vicinity of the Fermi energy, $E = 0$, K and K' vectors in Eq. (2.13) exist. $\overrightarrow{k}$ is expressed as $\overrightarrow{k} = \overrightarrow{K} + \overrightarrow{q}$. $f(k)$, near the K and K' points, is expressed as

$$\begin{aligned} f(k) &= \sum_{j=1,2,3} e^{i\overrightarrow{K}\cdot\overrightarrow{\delta_j}} e^{i\overrightarrow{q}\cdot\overrightarrow{\delta_j}} \\ &= \sum_{j=1,2,3} e^{i\overrightarrow{K}\cdot\overrightarrow{\delta_j}} \times \sum_p \frac{\left(i\left(\overrightarrow{q}\cdot\overrightarrow{\delta_i}\right)\right)^p}{p!}. \end{aligned} \tag{2.19}$$

After some algebra, the Hamiltonian in Eq. (2.16) is expressed as

$$\mathcal{H} = \xi\hbar v_{\mathrm{F}}\left(q_x\sigma^x + \xi q_y\sigma^y\right), \tag{2.20}$$

where v_{F} is the Fermi velocity,

$$v_{\mathrm{F}} = \frac{1}{\hbar}\frac{\partial E}{\partial k} = \pm\frac{3at}{2\hbar}, \tag{2.21}$$

and used the Pauli matrices

$$\sigma^x = \begin{pmatrix} 0 & 1 \\ 1 & 0 \end{pmatrix}, \qquad \sigma^y = \begin{pmatrix} 0 & -i \\ i & 0 \end{pmatrix}. \tag{2.22}$$

The valley degeneracy is expressed as ξ, where $\xi = +$ denotes the K point and $\xi = -$ denotes the K' point. The distribution in the vicinity of the K and K' vectors is expressed as

$$E_{\pm}\left(\overrightarrow{q}\right) \simeq \pm v_{\mathrm{F}}\hbar\left|\overrightarrow{q}\right| + \mathcal{O}\left[(q/K)^2\right]. \tag{2.23}$$

The conical shape of the band structure makes massless Dirac Fermion, and since the energy dispersion seems to be the massless particle in the Einstein's energy-momentum relation, $E = \pm\sqrt{m^2c^4 + \overrightarrow{p}^2c^2}$, where c is the

light velocity with $m \to 0$. The massless Dirac Fermion is predicted theoretically [25, 26] and observed experimentally [27–30]. Since the K and K' points are equivalent in the reciprocal space, graphene has a two-fold valley degeneracy. Because of the four-fold degeneracy, including the spin degeneracy, graphene has the half-integer quantum Hall effect. The details will be explained in Section 2.4.

2.3 Quantum Point Contact

Quantum point contact (QPC) has the simplest structure and is used for a test because its main properties are quantized conductance and can partition currents. In this Thesis, we fabricated the QPC on the GaAs/AlGaAs 2DEG as a test sample for the renovated noise measurement setup.

QPC is composed of fine metallic gate leads deposited on the 2DEG surface, as shown in Figure 2.4. Applying negative voltages to the gate leads can

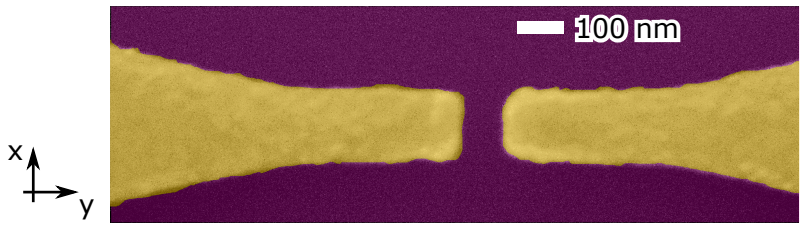

FIGURE 2.4: False-color SEM image of the QPC fabricated by me. The width of the gap between gate leads is 75 nm. It is fabricated by accumulating a thickness of 5 nm of Ti and 50 nm of Au.

increase the Schottky barrier in the 2DEG region. The high barriers create a region where carriers do not exist, the depletion layer. The carrier density can be controlled by applying an appropriate voltage. Broadening the size of the depletion region is also possible with the strong negative voltage of leads. As shown in Fig. 2.4, the narrow conductor can be created, where the yellow regions are the gate with gold metal, and the black region is GaAs, which has the 2DEG beneath it. This structure is called a QPC. The conductance of QPC versus gate voltage is shown in Fig. 2.5. At a large negative voltage, the conductance becomes zero. The region is called pinch-off. The conductance for the finite voltage has a step-like shape, with each height being $2e^2/h$. The quantized conductance is obtained from the discrete energy level between the QPC region.

The potential energy of QPC has a saddle-point because of the low energy in leads and high potential barrier in the depletion layer [see Fig. 2.5 b)]. Büttiker argued this model [32]. The saddle-point model potential in the xy-plane is given by

$$V(x,y) = V_0 - \frac{1}{2}m\omega_x^2 x^2 + \frac{1}{2}m\omega_y^2 y^2.$$

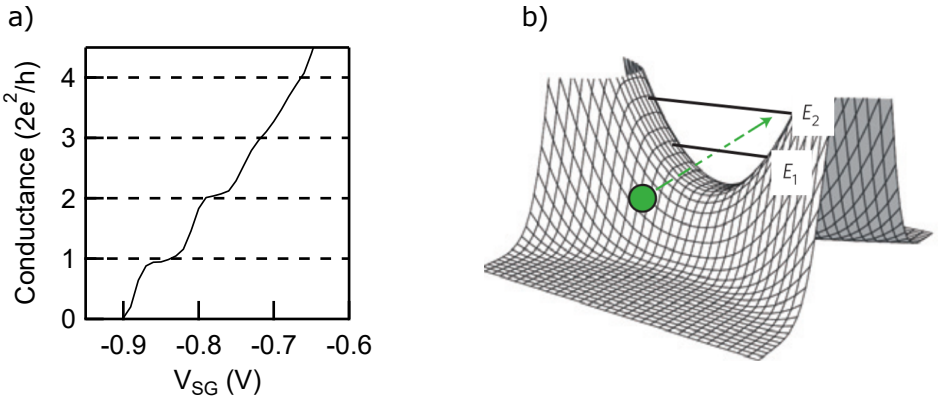

FIGURE 2.5: a) Conductance of the QPC. The QPC depletes the ballistic channel as the negative voltage is applied to the gate. The step-like shape of conductance is one of the main properties of QPC (results of Ch. 5). b) QPC forms the saddle-point potential comprising discrete energy levels only in one direction. Reprinted by permission from Springer Nature: Springer Nature NATURE PHYSICS [31], 2021. .

Here, V_0 is the electronic potential at the saddle, and ω_x and ω_y are the angular frequency along the x-axis and y-axis. Consequently, the area can be described by a harmonic oscillator. The energy-dependent transmission probability of electrons from the n-th incident channel to the m-th outgoing channel is expressed as [33, 34]

$$\mathcal{T}_{mn} = \frac{\delta_{mn}}{1 + e^{\pi\varepsilon_n}}, \qquad \varepsilon_n = 2\,\frac{\varepsilon - \hbar\omega_y\left(n + \frac{1}{2}\right) - V_0}{\hbar\omega_x},$$

where δ_{mn} is the Kronecker delta. Electrons can only transport when the incident and outgoing channels match each other. The transmission probabilities for $n = 0, 1, 2, \cdots$ can be plotted, as shown in Figure 2.6. Consequently, as the QPC gate is closed, the conductance decreases step by step with a quantized value, $G = M\frac{2e^2}{h}\mathcal{T}$, due to the Landauer formula in Eq. (2.7).

2.4 Quantum Hall Effect

The quantum Hall effect is one of the most significant effects in the two-dimensional system. We introduce the quantum Hall effect briefly according to Refs. [16, 35].

The classical Hall effect was discovered in 1879 by Edwin Herbert Hall [36]. He found that the transverse resistance in a thin metal in the strong magnetic field can be calculated as

$$R_H = \frac{B}{en_e}, \tag{2.24}$$

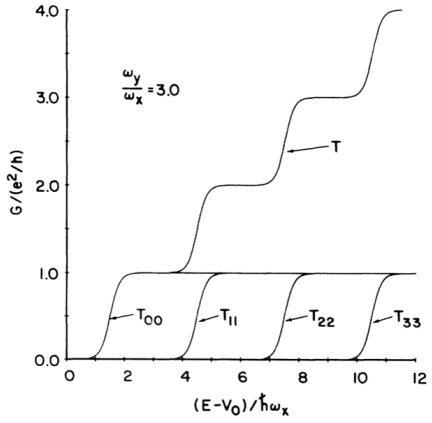

FIGURE 2.6: Transmission and conductance of QPC channel. Reprinted figure with permission from [32] Copyright 2021 by the American Physical Society.

where e is the carrier charge, n_e is the carrier density, and B is a planer magnetic field.

In the 2DEG, the quantum Hall effect was discovered in 1980 by Klaus von Klitzing [1]. The quantum Hall effect is independent of the geometry of samples, and the quantized Hall resistance is precise for integer numbers n, $\frac{nh}{2e^2}$.

Considering the conductance in a 2DEG, the Hamiltonian of an electron in the x-y two-dimensional plane in the magnetic field is expressed as

$$\mathcal{H} = \left[\frac{(i\hbar\nabla + e\boldsymbol{A})^2}{2m}\right]. \tag{2.25}$$

By assuming the magnetic field is parallel with the z-direction, we introduce a vector potential of a magnetic field:

$$\boldsymbol{A} = (0, B\boldsymbol{x}, 0)\,.$$

Equation (2.25) is given by

$$\left[\frac{p_x^2}{2m} + \frac{\left(p_y + eBx\right)^2}{2m}\right]\Psi(x,y) = E\Psi(x,y).$$

After some algebra, the solution is given by

$$\Psi_{n,k}(x,y) = \frac{1}{\sqrt{\mathcal{L}}}e^{ikx}u_n(q+q_k) \equiv |n,k\rangle$$
$$E(n,k) = \left(n+\frac{1}{2}\right)\hbar\omega_c, \quad n = 0,1,2,\cdots$$

where $\mathcal{L}$ is the sample length,

$$\begin{aligned} u_n(q) &= e^{-\frac{q^2}{2}} H_n(q), \\ q = y\sqrt{m\omega_c/\hbar} \quad &\text{and} \quad q_k = y_k\sqrt{m\omega_c/\hbar}, \\ y_k \equiv \frac{\hbar k}{eB} \quad &\text{and} \quad \omega_c \equiv \frac{|e|B}{m} \end{aligned}$$

and $H_n(q)$ is the Hermite polynomial. These levels are called Landau levels.

The conduction in the regime can be explained using the Landauer formula of Eq. (2.7). In the non-equilibrium state, when the longitudinal voltage drop is $V_{\mathrm{L}} = 0$ and the Hall voltage $eV_{\mathrm{H}} = \mu_{\mathrm{L}} - \mu_{\mathrm{R}}$, the net current through the quantum Hall state is expressed using Eq. (2.5) as

$$I = \frac{2e}{h} M \left(\mu_L - \mu_R\right). \tag{2.26}$$

Consequently, the longitudinal and Hall resistance are expressed as

$$R_{\mathrm{L}} = \frac{V_{\mathrm{L}}}{I} = 0, \qquad R_{\mathrm{H}} = \frac{V_{\mathrm{H}}}{I} = \frac{h}{2e^2 M}. \tag{2.27}$$

When the Fermi energy exists between two Landau levels, the Hall resistance has plateau, while the longitudinal resistance is zero. When the Zeeman splitting exists, the Hall resistance is

$$R_{\mathrm{H}} = \frac{h}{e^2 n} \simeq \frac{25.8128\ \mathrm{k\Omega}}{n}. \tag{2.28}$$

Hall conductance can be calculated by considering the density of states [1, 35, 37]. The flux density in a high magnetic field is given by

$$n_{\mathrm{B}} = \frac{B}{h/e}. \tag{2.29}$$

We assume that the Zeeman splitting exists. In this case, the localized number of states, n_{LL}, within each Landau level equals n_{B} [see Fig. 2.7 a)]. The filling factor is defined as

$$\nu = \frac{n_e}{n_B}. \tag{2.30}$$

Using the formula of classical Hall effect given in Eq. (2.24),

$$R_{\mathrm{H}} = \frac{h}{[\![\nu]\!] e^2} \tag{2.31}$$

The integer part of $[\![\nu]\!]$ equals the Landau level, n. Here, $[\![\cdots]\!]$ is the floor function for positive value and the ceiling function for another case.

In the quantum Hall effect regime, the carriers transport through the edge state. The edge state has the same chemical potential as the potential of a contact. Since the edge state is nondissipative, the abrupt change of the chemical

potential appears between the contact and the edge state, as shown in Fig. 2.7 b). The spot is called hotspot [38].

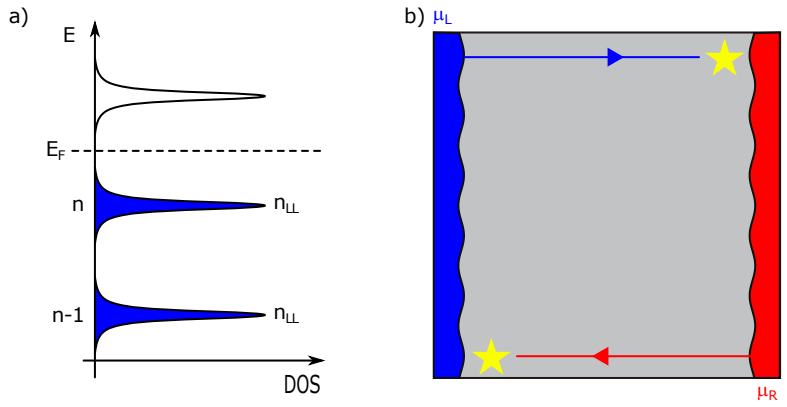

FIGURE 2.7: a) Density of states in a high magnetic field. The n-th Landau levels are completely filled. b) Schematic diagram of edge state and existence of the hotspot (yellow star) in the quantum Hall effect regime.

2.4.1 Graphene

We introduce the quantum Hall effect in monolayer graphene according to Refs. [23, 35, 37]. The Landau level of graphene differs from the levels of conventional 2DEG. The cyclotron energy in graphene is much higher [19, 39–41] than the energy in conventional 2DEG. We explain the quantum Hall effect with four-fold degeneracy. At a high magnetic field, the Hamiltonian Eq. (2.20) at the K point, $\xi = +$, is expressed as

$$\mathcal{H} = v_{\mathrm{F}} \begin{pmatrix} 0 & p_x + i\left(p_y + eBx\right) \\ p_x - i\left(p_y + eBx\right) & 0 \end{pmatrix}. \tag{2.32}$$

After some algebra, the eigenenergy is given by

$$E = \mathrm{sign}(n) v_{\mathrm{F}} \sqrt{2eB\hbar\,|n|}. \tag{2.33}$$

Here, n is the Landau level index $n = 0, \pm 1, \pm 2, \cdots$. The positive Landau level indexes denotes electron-like Landau levels (n-type regime), and the negative Landau level indexes denotes hole-like Landau levels (p-type regime).

The conductance can also be explained using the density of states [35]. The Landau level increases with the step in units of four, $4n$, due to the four-fold degeneracy. The half-integer quantum Hall effect appears when $n = 0$, where one has perfect electron-hole symmetry. Thus, the electron density n_e is given by [37]

$$n_e = n\frac{2eB}{h}\bigg|_K + n\frac{2eB}{h}\bigg|_{K'} + \frac{2eB}{h}\bigg|_{E=0} = \frac{4eB}{h}\left(n + \frac{1}{2}\right). \tag{2.34}$$

The filling factor is given by

$$\nu = \frac{n_e}{n_B} = \pm 4 \left(n + \frac{1}{2} \right). \tag{2.35}$$

As a consequence, the conductance is expressed as

$$G = \nu \frac{e^2}{h} = \pm 4 \left(n + \frac{1}{2} \right) \frac{e^2}{h}. \tag{2.36}$$

2.5 Quantum Hall Effect Breakdown

The dissipationless quantum Hall effect state is observed to be broken when the current, I_{sd}, exceeds a critical value, I_c, called the quantum Hall effect breakdown (QHEBD), as shown in Fig. 2.8. Many researchers have reported the effect [42–46]. The quantum Hall effect is a significant phenomenon in the International System of Units [47, 48]; the high bias voltage or bias current is necessary to measure a high resolution of the resistance standard. It is important to investigate the non-equilibrium state of the quantum Hall effect regime to understand the quantum Hall regime to realize the high-resolution standard resistance.

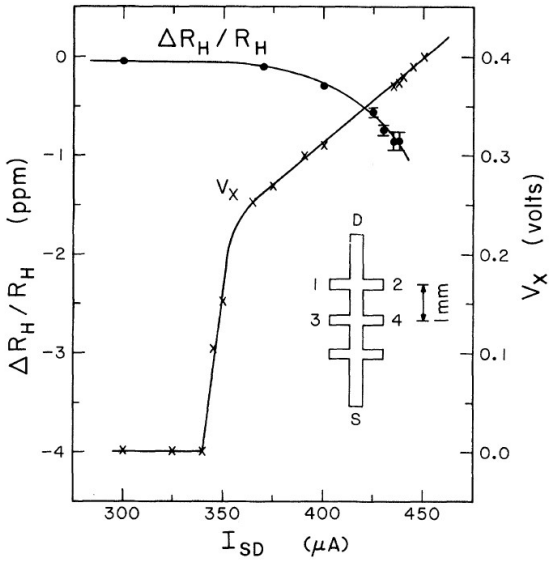

FIGURE 2.8: Hall resistance reduction due to quantum Hall effect breakdown. Reprinted figure with permission from [43] Copyright 2021 by the American Physical Society.

Researchers have suggested models that explain the processes of QHEBD. The two types of theories are famous: the bootstrap electron heating (BSEH) and the quasi-elastic inter-Landau level scattering (QUILLS). Many experienced researchers have tried to explain the process based on these theories.

The QUILLS model focuses on exciting electrons between inter-Landau levels [49–51], as shown in Fig. 2.9 a). The model is like the Zener effect in a

p-n diode, which explains that the excitation carriers exceed the band gap in high bias voltages. The model is proposed to explain the experimental data measured by Bliek *et al.* [52]. At $\nu = 2$, the critical electric field is given by [51]

$$\alpha e E_c l_b \simeq \hbar\omega_c, \tag{2.37}$$

where $l_b = \sqrt{\hbar/eB}$ and α is a numerical factor $\simeq 3$. This condition can be rewritten as

$$E_c = \frac{B}{\alpha m}\sqrt{\hbar e B}. \tag{2.38}$$

The characteristic of the model is also that E_c or I_c is proportional to $B^{3/2}$ because $\omega_c = eB/m$. Many experimental [46, 50, 52–58] and theoretical [49, 51] studies also support the model.

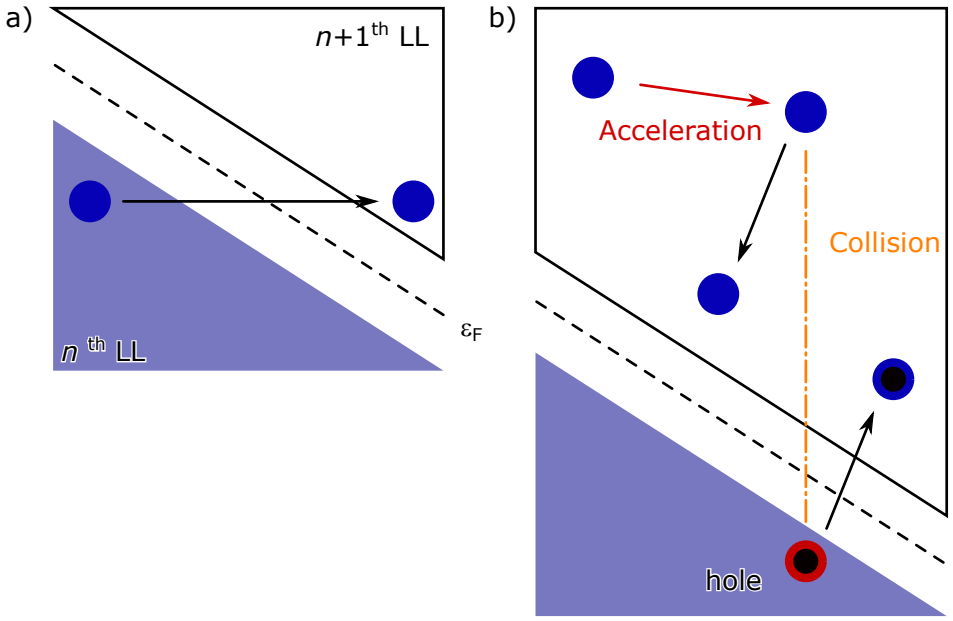

FIGURE 2.9: Schematic representation of a) QUILLS and b) BSEH models. a) Excitation of electrons is caused by several reasons, such as thermal fluctuation or high bias voltages. b) Small number of non-equilibrium electrons create electron-hole pairs by collisions. Reprinted figure with permission from [43] Copyright 2021 by the American Physical Society.

The BSEH model was proposed by Susumu Komiyama and Yasushi Kawaguchi [59], as shown in Fig.2.9 b). This model is like the avalanche breakdown in an insulating or p-n diode, which occurs when the accelerated carriers by electric fields collide with bound electrons and then create free electron-hole pairs. The model is a macroscopic model that considers the energy gain and loss of electrons. In the model, the system is thermally fluctuating in the QHEBD regime because the electrons scatter with the lattice. The critical electric field, E_c, is given by [59]

$$E_c = B\sqrt{\frac{2\hbar}{m^*\tau_e}}, \tag{2.39}$$

where $\tau_e \propto B^{-1}$ is a characteristic electron-phonon energy relaxation time. The characteristic of the model is that E_c or I_c is also proportional to $B^{3/2}$. The current is more than an order of magnitude smaller than that given by Eq. (2.38). Many experimental [45, 60–69] and theoretical [59] studies support the model.

However, it is also known that the signature of the QHEBD differs depending on the geometrical structure of the samples or the contact lead [70]. In this study, we measure the current noise at the QHEBD regime to understand the transport of electrons, and discuss on the process of the manifestation of the QHEBD later in Chapter 6.

Chapter 3

Current Noise in Mesoscopic Systems

We now introduce the current noise in mesoscopic systems mainly according to Ref. [3, 71].

3.1 Definition of Noise

Current fluctuation, called current noise, has significant information, on electron transport in mesoscopic samples. Numerous researchers have measured the current noise to investigate physics such as the quantum Hall effect breakdown [72–74], spin transport [75, 76], non-equilibrium statistical physics [77], Hanbury-Brown Twiss effect [78, 79], and quantum optics [80, 81].

When a resistor is connected to a voltage source that applies a bias voltage V, an ammeter shows the electric current I that flows through the resistor, as shown in Fig. 3.1. The current I means a time-averaged value $\langle I(t)\rangle$, determined by Ohm's law, $I = V/R$. One can also measure a finite fluctuation $\Delta I(t) \equiv I(t) - \langle I(t)\rangle \neq 0$ on the current, which is the current noise. The current noise power spectral density, which is the Fourier transform of $\Delta I(t)$, $\Delta I(\omega) = \int_{-\tau/2}^{\tau/2} dt \Delta I(t) \exp(i\omega t)$ for measured time $-\tau/2 \leq t \leq \tau/2$, is expressed as

$$\begin{aligned} S(\omega) &= \lim_{\tau\to\infty} \frac{2}{\tau} |\Delta I(\omega)|^2 \\ &= \lim_{T\to\infty} \frac{2}{\tau} \int_{-\tau/2}^{\tau/2} dt \int_{-\tau/2}^{\tau/2} dt' \left\langle \Delta I(t)\Delta I(t')\right\rangle \exp\left(i\omega(t-t')\right). \end{aligned} \quad (3.1)$$

Here, $\omega = 2\pi f$ is an angular frequency. The physical unit of S is easily seen from the definition. The unit of the current, $[\mathrm{A}] = [\mathrm{C/s}]$, corresponds to the number of electrons passing through the system for a finite time, while the unit of the current noise, $\left[\mathrm{A^2/Hz}\right] = \left[\mathrm{C^2/s}\right]$, corresponds to the variance of the number of electrons passing through the system for the corresponding time.

Generally, the noise has different information at different frequency regime: low frequency ($hf \ll k_\mathrm{B}T_e$) and high frequency regimes ($hf \gg k_\mathrm{B}T_e$), where h is the Plank constant, f is the frequency, k_B is the Boltzmann constant, and

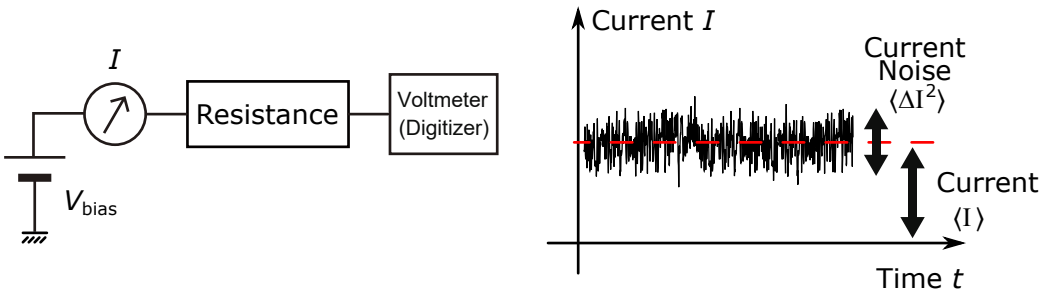

FIGURE 3.1: Schematic of the noise measurement system. A current I is measured by the voltmeter (digitizer). The current, $\langle I \rangle$, has intrinsic noise, $\langle (\Delta I)^2 \rangle$.

T_e is the temperature of the electron. This thesis focuses on the current noise for the low-frequency regime and shows what information we can obtain.

3.1.1 $1/f$ Noise

We introduce the $1/f$ noise according to Ref. [82].

The $1/f$ noise is the power spectral density appearing in the low-frequency regime. The $1/f$ noise was named because the spectral density depends inversely on the frequency.

The power spectral density, $S(f)$, is expressed as $S(f) \simeq 1/f^{\gamma}$, where f is the frequency and $\gamma \simeq 1$ is an experimental parameter. The noise was first discovered in vacuum tubes [83] and observed in electronic systems [84, 85]. In electronic systems, one of the main properties of noise is usually found at $f < 100$ kHz. It is well-known that the $1/f$ noise measurement is related to the properties of individual devices [86].

There are mainly two types of origins for the $1/f$ noise [87]; the fluctuation of the carrier density, n_e, and the fluctuation of the mobility, μ, because the deviation of the current, $I \propto e n_e \mu$, can be expressed as $\delta I \propto e\,(\delta n_e)\,\mu + e n_e\,(\delta \mu)$, where e is the charge of an electron.

The carrier-density-fluctuation mechanism is generated from carrier capture and emission back of defects of a sample [88]. Because each defects has different capture times, the $1/f$ properties appear. The mobility-fluctuation mechanism is generated from the varying scattering cross-section of the defects, such as multi-potential and carrier capture and release, *etc.* [89, 90]. The $1/f$ noise from any mechanisms can be expressed using the Hooge parameter, α_{H}, [91]

$$\frac{S^I}{I^2} = \frac{\alpha_{\mathrm{H}}}{n_e f}, \tag{3.2}$$

where $S^I \simeq (\delta I)^2$ is the power spectral density of the fluctuations due to the current. The $1/f$ noise was measured to estimate the purities of the sample, such as the puddle of the graphene [92, 93] or breakdown mechanism of the insulator [94].

3.1.2 Thermal Noise

Thermal fluctuations of the carriers exist at finite temperature. The fluctuation causes the noise.

When the sample is in an equilibrium state, such as zero bias, the average current, $\langle I(t)\rangle$, is also zero, while the current noise, $\langle(\Delta I)^2\rangle$, is not zero, originating from the thermal excitation of the carriers. The noise is referred to as the thermal noise or Johnson-Nyquist noise [95, 96]. The noise power spectral density, S^I, is given by

$$S^I = 4k_B T_e G, \tag{3.3}$$

where $G = I/V$ is the conductance of the sample. Since this noise is independent of frequency, it is a white noise. The noise is often used to measure the temperature of the carriers or to calibrate the noise measurement system. Details will be discussed in Chapter 4.

3.1.3 Shot Noise

Shot noise is a consequence of charge discreteness. The shot noise appears when the sample is in the non-equilibrium state.

Here, we consider one particle incident to a barrier that has the transmission probability $\mathcal{T}$ and the reflection probability $\mathcal{R}(=1-\mathcal{T})$ to describe the shot noise [3]. The incident occupation number is n_i, the transmitted occupation number is $n_\mathcal{T}$, and the reflected occupation number is $n_\mathcal{R}$. When a sufficiently large number of processes occurs, we can calculate the average and the variations of these occupation numbers. Let the incident occupation number, n, be 1; $\langle n_\mathrm{i}\rangle = 1$. Thus, $\langle n_\mathcal{T}\rangle = \mathcal{T}$ and $\langle n_\mathcal{R}\rangle = \mathcal{R}$. The deviation from the average occupation number is expressed as $\left\langle \left(n_j - \langle n_j\rangle\right)^2 \right\rangle$, where n_j is the incident, transmitted, and reflected occupation numbers. The mean-squared fluctuations of the incident numbers will vanish [1]; $(n_\mathrm{i} - \langle n_\mathrm{i}\rangle)^2 = 0$. The correlation of the transmitted and reflected state will also vanish; $\langle n_\mathcal{T} n_\mathcal{R}\rangle = 0$. Hence, the correlation of the mean-squared fluctuations of the

[1] Note that $n^2 = n$ in a Fermi system.

transmitted and reflected state is given by [2]

$$\left\langle (n_{\mathrm{i}} - \langle n_{\mathrm{i}} \rangle)^2 \right\rangle = \left\langle (\Delta n_{\mathcal{T}})^2 \right\rangle + 2 \langle \Delta n_{\mathcal{T}} \Delta n_{\mathcal{R}} \rangle + \left\langle (\Delta n_{\mathcal{R}})^2 \right\rangle, \tag{3.4}$$

where $\Delta n_{\mathcal{T}(\mathcal{R})} \equiv n_{\mathcal{T}(\mathcal{R})} - \left\langle n_{\mathcal{T}(\mathcal{R})} \right\rangle$. Because $\langle \Delta n_{\mathcal{T}} \Delta n_{\mathcal{R}} \rangle = -\mathcal{T}\mathcal{R}$ [3], the mean-squared of the transmitted and reflected states and their correlation is given by

$$\left\langle (\Delta n_{\mathcal{T}})^2 \right\rangle = \left\langle (\Delta n_{\mathcal{R}})^2 \right\rangle = - \langle \Delta n_{\mathcal{T}} \Delta n_{\mathcal{R}} \rangle = \mathcal{T}\mathcal{R}. \tag{3.5}$$

Based on those relations, the total transmitted current is expressed as

$$\int_{-\tau/2}^{\tau/2} \mathrm{d}t I(t) = e n_{\mathcal{T}}$$

and on the average current is given by

$$\langle I(t) \rangle = \frac{e \langle n_{\mathcal{T}} \rangle}{\tau} = \frac{e\mathcal{T}}{\tau}.$$

Because the power spectral density [Eq. (3.1)] of the shot noise is independent of the frequency, we consider the zero frequency limit for convenience. The power spectral density is expressed as

$$S(0) = \frac{2}{\tau} \int_{-\tau/2}^{\tau/2} \mathrm{d}t \int_{-\tau/2}^{\tau/2} \mathrm{d}t' \left\langle \Delta I\left(t\right) \Delta I\left(t'\right) \right\rangle = \frac{2e^2}{\tau} \left\langle (\Delta n_{\mathcal{T}})^2 \right\rangle$$

[2] The step-by-step solution is

$$\begin{aligned} 0 = \left\langle (n_{\mathrm{i}} - \langle n_{\mathrm{i}} \rangle)^2 \right\rangle &= \left\langle [(n_{\mathcal{T}} + n_{\mathcal{R}}) - (\langle n_{\mathcal{T}} \rangle + \langle n_{\mathcal{R}} \rangle)]^2 \right\rangle \\ &= \left\langle [(n_{\mathcal{T}} - \langle n_{\mathcal{T}} \rangle) + (n_{\mathcal{R}} - \langle n_{\mathcal{R}} \rangle)]^2 \right\rangle \\ &= \left\langle (n_{\mathcal{T}} - \langle n_{\mathcal{T}} \rangle)^2 \right\rangle + 2 \langle (n_{\mathcal{T}} - \langle n_{\mathcal{T}} \rangle)(n_{\mathcal{R}} - \langle n_{\mathcal{R}} \rangle) \rangle \\ &\quad + \left\langle (n_{\mathcal{R}} - \langle n_{\mathcal{R}} \rangle)^2 \right\rangle \\ &= \left\langle (\Delta n_{\mathcal{T}})^2 \right\rangle + 2 \langle \Delta n_{\mathcal{T}} \Delta n_{\mathcal{R}} \rangle + \left\langle (\Delta n_{\mathcal{R}})^2 \right\rangle. \end{aligned}$$

[3] The step-by-step solution is

$$\begin{aligned} \langle \Delta n_{\mathcal{T}} \Delta n_{\mathcal{R}} \rangle &= \langle n_{\mathcal{T}} n_{\mathcal{R}} - \langle n_{\mathcal{T}} \rangle n_{\mathcal{R}} - \langle n_{\mathcal{R}} \rangle n_{\mathcal{T}} + \langle n_{\mathcal{T}} \rangle \langle n_{\mathcal{R}} \rangle \rangle \\ &= 0 - \langle n_{\mathcal{T}} \rangle \langle n_{\mathcal{R}} \rangle - \langle n_{\mathcal{R}} \rangle \langle n_{\mathcal{T}} \rangle + \langle n_{\mathcal{T}} \rangle \langle n_{\mathcal{R}} \rangle \\ &= - \langle n_{\mathcal{T}} \rangle \langle n_{\mathcal{R}} \rangle \\ &= -\mathcal{T}\mathcal{R}. \end{aligned}$$

In the Poissonian process, $\mathcal{T}$ is very small, $\left\langle (\Delta n_{\mathcal{T}})^2 \right\rangle \simeq \mathcal{T}$ [Eq. (3.5)]. Thus, the shot noise power spectral density is

$$S_{\mathrm{P}}^{I} = \frac{2e^2\mathcal{T}}{\tau} = \frac{2e^2}{\tau} \langle n_{\mathcal{T}} \rangle = 2e \langle I(t) \rangle .$$

If the electrons do not transport in the Poissonian process, the shot noise can be expressed as

$$S^{I} = 2eF \langle I(t) \rangle ,$$

where Fano factor $F = S^{I}/S_{\mathrm{P}}^{I}$. The details will be explained in Chapter 3.2.

3.2 Current Noise Based on Landauer Picture

Here, we derive the general formula for the shot noise and the averaged current based on the Landauer picture according to Ref. [3].

3.2.1 Scattering Theory

Let the ideal infinite one-dimensional reservoirs (the leads) be connected to the mesoscopic sample (Fig. 3.2). The Hamiltonian of the left or right lead is

$$\mathcal{H} = \sum_{k} (\varepsilon_k - \mu)\, c_k^{\dagger} c_k, \tag{3.6}$$

where $\varepsilon_k = \hbar^2 k^2/2m$ is the energy of electrons, μ is the chemical potential, $c_k^{\dagger}$ is the creation operator, and c_k is the annihilation operator, respectively. In the vicinity of the Fermi energy, the linear approximation of Eq. (3.6) is given by $\varepsilon_k - \mu = \hbar v_{\mathrm{F}} (k - k_{\mathrm{F}})$, where $v_{\mathrm{F}} = \hbar k_{\mathrm{F}}/m$ is the Fermi velocity, and k_{F} is the Fermi wavenumber.

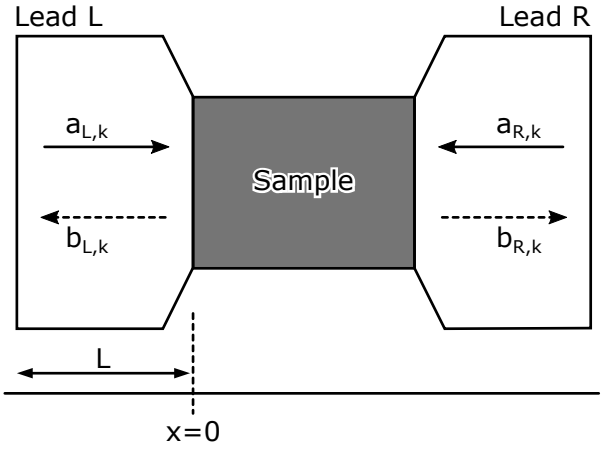

FIGURE 3.2: Schematic of a two-terminal conductor. The sample has one transverse channel. a is the operator for the incident state upon the sample, and b is the operator for the outgoing state.

We consider the left lead, L. We introduce creation $a^{\dagger}_{\mathrm{L},k}$ and annihilation $a_{\mathrm{L},k}$ operators in the left lead incident to the sample. In the same way, the creation $b^{\dagger}_{\mathrm{L},k}$ and annihilation $b_{\mathrm{L},k}$ operators describe electrons in the outgoing states. In this case, the Hamiltonian is expressed as

$$\mathcal{H} = \sum_k \hbar v_{\mathrm{F}} \left(k - k_{\mathrm{F}}\right) a^{\dagger}_{\mathrm{L},k} a_{\mathrm{L},k} + \sum_k \left(-\hbar v_{\mathrm{F}}\right) \left(k + k_{\mathrm{F}}\right) b^{\dagger}_{\mathrm{L},k} b_{\mathrm{L},k}.$$

Enough far from the sample, the current in the left lead is expressed as

$$\hat{I}(x) = \frac{\hbar e}{2im}\left(\hat{\psi}^{\dagger}(x)\frac{\mathrm{d}\hat{\psi}(x)}{\mathrm{d}x} - \frac{\mathrm{d}\hat{\psi}^{\dagger}(x)}{\mathrm{d}x}\hat{\psi}(x)\right),$$

where $\hat{\psi}^{\dagger}(x) = \sum_k \left(\sqrt{\mathcal{L}}\right)^{-1} \exp\left(ikx\right) c_k$ is the field operator, c_k is $a_{\mathrm{L},k}$ at $k \simeq +k_{\mathrm{F}}$, c_k is $b_{\mathrm{L},k}$ at $k \simeq -k_{\mathrm{F}}$, and $\mathcal{L}$ is the lead length. The current can then be expressed as

$$\hat{I}(x) = \frac{\hbar e}{\mathcal{L}} \sum_{k,k'} \frac{k + k'}{2m} c^{\dagger}_k c_{k'} e^{i(k'-k)x}.$$

We consider the vicinity of $k \simeq \pm k_{\mathrm{F}}$ and at $x = 0$, corresponding to the junction position between the lead and the sample. Thus, the current is expressed as

$$\hat{I} = \hat{I}(x=0) = \frac{e v_{\mathrm{F}}}{\mathcal{L}} \sum_{k,k'} \left(a^{\dagger}_{\mathrm{L},k} a_{\mathrm{L},k} - b^{\dagger}_{\mathrm{L},k} b_{\mathrm{L},k}\right) \tag{3.7}$$

We consider the left, L, and right, R, leads. The index of the lead α means L and R. The operators $a_{\alpha,k}$ and $b_{\alpha,k}$ are related via the scattering matrix S,

$$\begin{pmatrix} b_{\mathrm{L},k} \\ b_{\mathrm{R},k} \end{pmatrix} = S \begin{pmatrix} a_{\mathrm{L},k} \\ a_{\mathrm{R},k} \end{pmatrix}.$$

Here S has the block structure

$$S = \begin{pmatrix} S^{\mathrm{LL}}(k) & S^{\mathrm{LR}}(k) \\ S^{\mathrm{RL}}(k) & S^{\mathrm{RR}}(k) \end{pmatrix} = \begin{pmatrix} r & t' \\ t & r' \end{pmatrix},$$

Here, r and r' describe electron reflection back to the left and right reservoirs, respectively, but t and t' are responsible for the electron transmission through the sample. Because the creation and annihilation operators obey anticommutation relations

$$\left[a_{\alpha,k}, a^{\dagger}_{\alpha',k'}\right] = \left[b_{\alpha,k}, b^{\dagger}_{\alpha',k'}\right] = \delta_{\alpha,\alpha'}\delta_{k,k'},$$

the scattering matrix S is unitary.

We can express the current from the left lead in Eq. (3.7) in terms of scattering matrix S,

$$\hat{I}_{\mathrm{L}} = \frac{e v_{\mathrm{F}}}{\mathcal{L}} \sum_{\alpha=\mathrm{L},\mathrm{R}} \sum_{\beta=\mathrm{L},\mathrm{R}} \sum_{k,k'} a^{\dagger}_{\alpha,k} A^{\alpha\beta}_{\mathrm{L}}\left(k,k'\right) a_{\beta,k'}, \tag{3.8}$$

where

$$A_{\mathrm{L}}^{\alpha\beta}\left(k,k'\right)=\delta_{\mathrm{L},\alpha}\delta_{\mathrm{L},\beta}-\left(S^{\mathrm{L}\alpha}\left(k\right)\right)^{*}S^{\mathrm{L}\beta}\left(k'\right).$$

3.2.2 Average Current

The creation and annihilation operators at equilibrium state are expressed as

$$\left\langle a_{\alpha,k}^{\dagger}a_{\beta',k'}\right\rangle=\delta_{\alpha,\beta}\delta_{k,k'}f_{\alpha}(k),$$

where $f_{\alpha}(k)$ is the Fermi-Dirac distribution function,

$$f_{\alpha}(k)=\frac{1}{\exp\left[\left(\varepsilon_{k}-\mu_{\alpha}\right)/k_{\mathrm{B}}T_{e}\right]+1}.$$

The average of the current shown in Eq. (3.8) is

$$\left\langle\hat{I}_{\mathrm{L}}\right\rangle=\frac{ev_{\mathrm{F}}}{\mathcal{L}}\sum_{k}\sum_{\alpha}A_{\mathrm{L}}^{\alpha\alpha}(k,k)f_{\alpha}(k)=\frac{e}{2\pi\hbar}\int_{-\infty}^{\infty}\mathrm{d}\varepsilon\sum_{\alpha}A_{\mathrm{L}}^{\alpha\alpha}\left(\varepsilon,\varepsilon\right)f_{\alpha}\left(\varepsilon\right).$$

$\left(\mathcal{L}^{-1}\sum_{k}\right)$ can be changed to $\left[\int dk/(2\pi)\right]$ in wide lead, k is changed to ε due to $\varepsilon_{k}=\hbar v_{\mathrm{F}}\left(k-k_{\mathrm{F}}\right)$, $A_{\mathrm{L}}^{\mathrm{LL}}=\left|t\right|^{2}\equiv\mathcal{T}$, and $A_{\mathrm{L}}^{\mathrm{RR}}=-\left|t'\right|^{2}=-\mathcal{T}$, this formula is expressed as follows:

$$\left\langle\hat{I}_{\mathrm{L}}\right\rangle=\frac{e}{2\pi\hbar}\int_{-\infty}^{\infty}\mathrm{d}\varepsilon\mathcal{T}\left(\varepsilon\right)\left[f_{\mathrm{L}}\left(\varepsilon\right)-f_{\mathrm{R}}\left(\varepsilon\right)\right].$$

In the zero-temperature and the equilibrium state, $\left[f_{\mathrm{L}}\left(\varepsilon\right)-f_{\mathrm{R}}\left(\varepsilon\right)\right]$ is one for $0\leq\varepsilon\leq eV$, and otherwise zero. Thus, the current is expressed as

$$\left\langle\hat{I}_{\mathrm{L}}\right\rangle=\frac{e^{2}}{2\pi}\mathcal{T}V,$$

and the conductance G is given by

$$G=\frac{\left\langle\hat{I}_{\mathrm{L}}\right\rangle}{V}=\frac{e^{2}}{h}\mathcal{T}. \tag{3.9}$$

Equation (3.9) is referred to as the Landauer formula.

Using $f_{\mathrm{L}}(\varepsilon)-f_{\mathrm{R}}(\varepsilon)=f\left(\varepsilon-eV\right)-f(\varepsilon)\simeq\left(-\mathrm{d}f/\mathrm{d}\varepsilon\right)eV$, the conductance is expressed as

$$G=\frac{e^{2}}{2\pi\hbar}\int\mathrm{d}\varepsilon\mathcal{T}(\varepsilon)\left(-\frac{\mathrm{d}f(\varepsilon)}{\mathrm{d}\varepsilon}\right). \tag{3.10}$$

3.2.3 General Expression for Noise

The time evolution expression of the current is expressed as

$$\hat{I}_{\mathcal{L}}(t)=e^{\frac{i\mathcal{H}t}{\hbar}}\hat{I}_{\mathrm{L}}e^{-\frac{i\mathcal{H}t}{\hbar}}.$$

We define the correlation function, $C(t,t')$, using the fluctuation of the current $\Delta\hat{I}_{\mathrm{L}}(t) = \hat{I}_{\mathrm{L}}(t) - \left\langle \hat{I}_{\mathrm{L}}(t) \right\rangle$

$$C\left(t,t'\right) \equiv \left\langle \Delta\hat{I}_{\mathrm{L}}(t)\Delta\hat{I}_{\mathrm{L}}(t') \right\rangle = \left\langle \hat{I}_{\mathrm{L}}(t)\hat{I}_{\mathrm{L}}(t') \right\rangle - \left\langle \hat{I}_{\mathrm{L}}(t) \right\rangle \left\langle \hat{I}_{\mathrm{L}}(t') \right\rangle .$$

Using Eq. (3.1), the power spectral density $S(\omega)$ is expressed as

$$S(\omega) \equiv \lim_{\tau\to\infty} \frac{2}{\tau} \int_{-\tau/2}^{\tau/2} \mathrm{d}t \int_{-\tau/2}^{\tau/2} \mathrm{d}t' C\left(t,t'\right) e^{i\omega(t-t')}.$$

This equation can be expressed using $\Delta t = t - t'$

$$\begin{aligned} S(\omega) &= \lim_{\tau\to\infty} \frac{2}{\tau} \int_{-\tau/2}^{\tau/2} \int_{-\infty}^{\infty} \mathrm{d}\left(\Delta t\right) C\left(\Delta t\right) e^{i\omega\Delta t} \\ &= 2\int_{-\infty}^{\infty} \left[\mathrm{d}\left(\Delta t\right)\right] C\left(\Delta t\right) e^{i\omega\Delta t}, \end{aligned}$$

where we assume the Δt is sufficiently large due to the lack of correlation between the two current at different times. Thus, the white noise, $S(\omega = 0)$ is expressed as

$$S(0) = 2\int_{-\infty}^{\infty} \mathrm{d}t \left(\left\langle \hat{I}_{\mathrm{L}}\left(t\right) \hat{I}_{\mathrm{L}}\left(0\right) \right\rangle - \left\langle \hat{I}_{\mathrm{L}}\left(t\right) \right\rangle \left\langle \hat{I}_{\mathrm{L}}\left(0\right) \right\rangle \right). \tag{3.11}$$

We obtain the expression for the power spectral density using the time evolution of the current, Eq. (3.8),

$$\begin{aligned} S(0) &= 2\int_{-\infty}^{\infty} \mathrm{d}t \left(\frac{ev_{\mathrm{F}}}{\mathcal{L}}\right)^2 \sum_{k,k',k'',k'''} \sum_{\alpha,\beta,\alpha',\beta'} A_{\mathrm{L}}^{\alpha\beta}\left(k,k'\right) A_{\mathrm{L}}^{\alpha',\beta'}\left(k'',k'''\right) \\ &\quad \times \left[\left\langle a_{\alpha,k}^{\dagger} a_{\beta,k'} a_{\alpha',k''}^{\dagger} a_{\beta',k'''} \right\rangle - \left\langle a_{\alpha,k}^{\dagger} a_{\beta,k'} \right\rangle \left\langle a_{\alpha',k''}^{\dagger} a_{\beta',k'''} \right\rangle \right] \\ &\quad \times \exp\left(\frac{i\left(\varepsilon_k - \varepsilon_{k'}\right) t}{\hbar} \right). \end{aligned} \tag{3.12}$$

Here, for Fermi gas at equilibrium, the expectation value is

$$\begin{aligned} & \left\langle a_{\alpha,k}^{\dagger} a_{\beta,k'} a_{\alpha',k''}^{\dagger} a_{\beta',k'''} \right\rangle - \left\langle a_{\alpha,k}^{\dagger} a_{\beta,k'} \right\rangle \left\langle a_{\alpha',k''}^{\dagger} a_{\beta',k'''} \right\rangle \\ = & \left\langle a_{\alpha,k}^{\dagger} a_{\beta',k'''} \right\rangle \left\langle a_{\beta,k'} a_{\alpha',k''}^{\dagger} \right\rangle \\ = & \delta_{\alpha,\beta'}\delta_{k,k'''}\delta_{\beta,\alpha'}\delta_{k',k''} f_{\alpha}\left(k\right)\left[1 - f_{\beta}\left(k\right)\right], \end{aligned} \tag{3.13}$$

using Wick's theorem. By Riemann integral in wavenumber k and integrating with respect to t, the white noise power spectral is

$$S(0) = \frac{e^2}{\pi\hbar} \int \mathrm{d}\varepsilon \sum_{\alpha,\beta} A_{\mathrm{L}}^{\alpha,\beta}\left(\varepsilon,\varepsilon\right) A_{\mathrm{L}}^{\beta,\alpha}\left(\varepsilon,\varepsilon\right) f_{\alpha}\left(\varepsilon\right)\left[1 - f_{\beta}\left(\varepsilon\right)\right]. \tag{3.14}$$

For $|eV| \ll k_{\mathrm{B}}T_e$ regime,

$$\begin{aligned} f(\varepsilon)\left[1-f(\varepsilon)\right] &= k_{\mathrm{B}}T_e\left(-\partial f/\partial\varepsilon\right), \\ \sum_{\alpha,\beta} A_{\mathrm{L}}^{\alpha,\beta}(\varepsilon,\varepsilon)\, A_{\mathrm{L}}^{\beta,\alpha}(\varepsilon,\varepsilon) &= 2\mathcal{T}(\varepsilon). \end{aligned} \tag{3.15}$$

Using Eq. (3.10), equation (3.14) is expressed as

$$S(0) = 4k_{\mathrm{B}}T_eG. \tag{3.16}$$

The formula is the Johnson-Nyquist noise [Eq. (3.3)].

For $k_{\mathrm{B}}T_e \ll |eV|$ regime can be expressed as $f_{\mathrm{L}}(\varepsilon) = \Theta(-\varepsilon + eV)$ and $f_{\mathrm{R}}(\varepsilon) = \Theta(-\varepsilon)$. Here, $\Theta(x)$ is the Heaviside step function. At zero temperature, the power spectral density in a two-terminal measurement is expressed as

$$S(0) = \frac{e^2}{\pi\hbar} A_{\mathrm{L}}^{\mathrm{LR}}(\varepsilon,\varepsilon) A_{\mathrm{L}}^{\mathrm{RL}}(\varepsilon,\varepsilon)\,|eV|\,. \tag{3.17}$$

We assume that the energy dependence of $\mathcal{T}$ is very small compared to the energy scale of the temperature and bias voltage. Since $A_{\mathrm{L}}^{\mathrm{LR}} A_{\mathrm{L}}^{\mathrm{RL}} = |t|^2\left(1 - |t|^2\right) = \mathcal{T}(1-\mathcal{T})$, the power spectral density is expressed as

$$S(0) = \frac{e^2}{\pi\hbar}\mathcal{T}(1-\mathcal{T})\,|eV| = 2e\,\langle I\rangle\,(1-\mathcal{T}). \tag{3.18}$$

At finite temperature, the formula is expressed as

$$S = 4k_{\mathrm{B}}T_eG + 2e\,\langle I\rangle\,(1-\mathcal{T})\left[\coth\left(\frac{eV}{2k_{\mathrm{B}}T_e} - \frac{2k_{\mathrm{B}}T_e}{eV}\right)\right]. \tag{3.19}$$

The factor $1-\mathcal{T}$ is the Fano factor in one-dimensional channel. In the multichannel, Eq. (3.19) is given by

$$S = 4k_{\mathrm{B}}T_eG + 2e\,\langle I\rangle\,F\left[\coth\left(\frac{eV}{2k_{\mathrm{B}}T_e}\right) - \frac{2k_{\mathrm{B}}T_e}{eV}\right], \tag{3.20}$$

where F is the Fano factor

$$F \equiv \frac{\sum_n \mathcal{T}_n(1-\mathcal{T}_n)}{\sum_n \mathcal{T}_n}. \tag{3.21}$$

Equation (3.20) is the general formation of white noise. In the equilibrium state, $k_{\mathrm{B}}T_e \ll |eV|$, the expression is expressed as Eq. (3.16), while the expression is expressed as Eq. (3.20) in the non-equilibrium state.

For example, we introduce the current noise in the quantum point contact (QPC). As explained in Section 2.3, the QPC has channels. Since each channel has each transmission probability $\mathcal{T}$, we can calculate the Fano factor by varying the gate voltage (Fig. 3.3). Because the current noise of QPC can be explained easily, thus it is often used as the test sample. The details will be explained in Chapter 5.

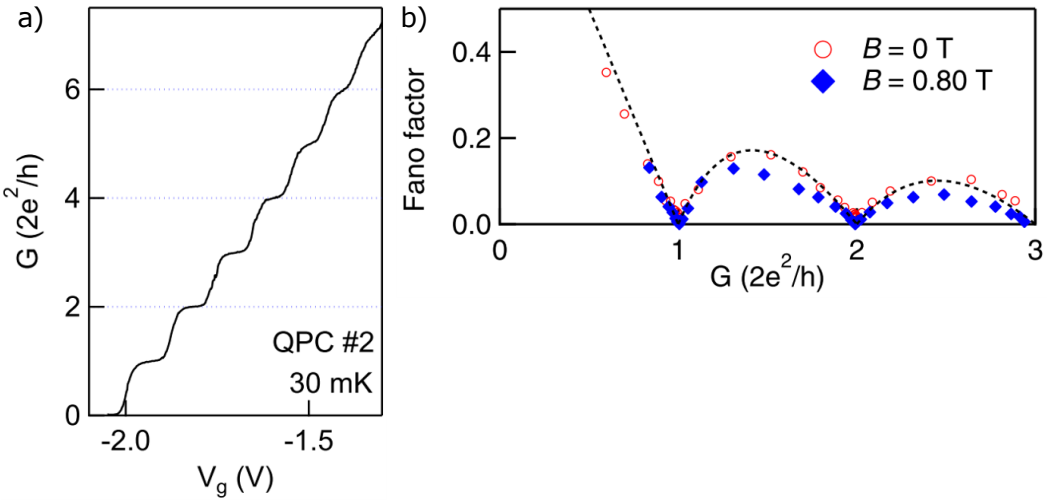

FIGURE 3.3: Conductance and current noise of QPC. a) Conductance as a function of gate voltage. b) Fano factor as a function of conductance. The black line is the theoretical value Reprinted figure with permission from [97] Copyright 2021 by the American Physical Society.

Chapter 4

Current Noise Measurement

In this Chapter, we introduce several noise measurement techniques [98]. How to measure the current noise is technically more complicated than how to measure the conductance. Here, we show three types of examples of the noise measurement technique development citing several references [99–102].

4.1 Background

Usually, the current noise for the mesoscopic sample is measured below 1 K to reduce thermal excitation and maintain coherent transport. The noise generated from the sample is remarkably small to measure using the general ammeter. Amplifiers are important to amplify the noise up to the measurable quantity. We measure the voltage noise since voltage amplifiers are less difficult to handle than the current amplifiers to directly measure the current noise. The fluctuating current noise from the mesoscopic sample, $\Delta I_{\rm in}(t)$, is converted to the voltage signal by

$$\Delta V_{\rm in}(t) = Z\Delta I_{\rm in}(t),$$

where Z is the total impedance of the circuit before the input port of the amplifier, and $\Delta V_{\rm in} \equiv V_{\rm in}(t) - \langle V_{\rm in}\rangle$. Here, $\langle\cdots\rangle$ is a time-averaged value. The voltmeter records the amplified voltage noise as the voltage spectral density, $S^V(\omega) \equiv \langle \Delta V_{\rm in}^2 \rangle$, via the fast Fourier transformation (FFT).

When extra electronic circuits, such as amplifiers, exist, we cannot avoid extrinsic noise, δv, generated from them. If we build the measurement system, as shown in Fig. 4.1 a), the amplified voltage signal is expressed with extrinsic noise as [1]

$$\Delta V_{\rm meas} = A_2\left(\Delta V_{\rm out} + \delta v_2\right) = A_2\left[A_1(\Delta V_{\rm in} + \delta v_1) + \delta v_2\right],$$

where A is the gain of an amplifier. While the extrinsic noise of "Amplifier 2", δv_2, is only amplified A_2 times, δv_1 is amplified A_2A_1 times by "Amplifier 1" and "Amplifier 2". The extrinsic noise of the signal is mainly affected in the first-stage amplifier of the system. Figure 4.1 b) shows the typical power spectrum density of voltage noise $\Delta V_{\rm meas}$ in a solid red line. As shown in

[1] We assume that we measure the signal for infinite time.

Fig. 4.1 b), the noise spectral density can be divided into two regions. The $1/f$ noise region is dominant at low frequency (typically below 100 kHz). The noise is originated from the amplifier, or the mesoscopic sample itself. A higher frequency region is called the white noise; a frequency-independent noise is dominant.

The extrinsic noise is added to the intrinsic noise from the sample, as shown in Fig. 4.1 b) (solid black line). Below, we show how the noise measurement setup changes the noise spectral density. We explain several measurement systems considering only the amplifier in the first stage and extrinsic noise from that for convenience.

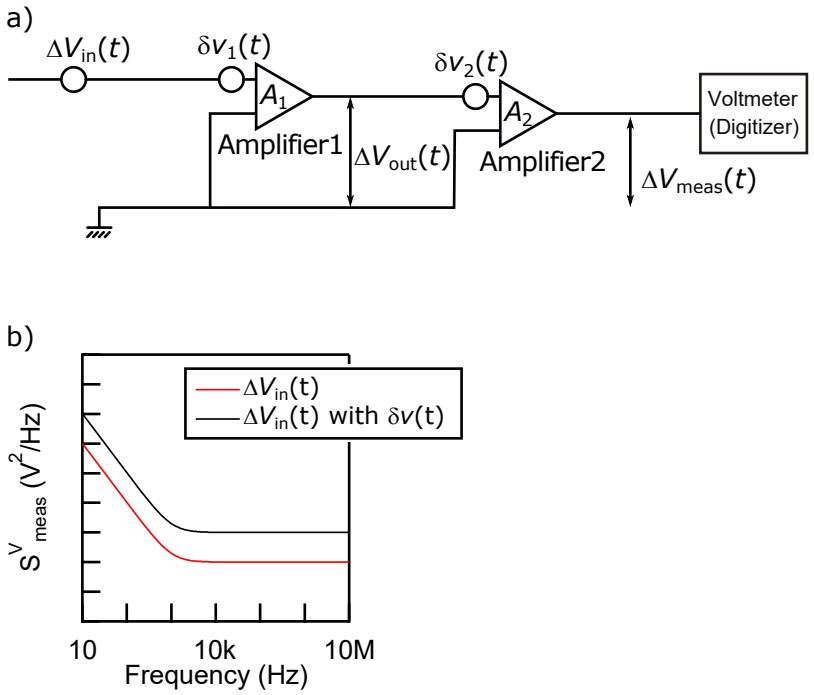

FIGURE 4.1: a) Amplifiers amplify not only $\Delta V_{\rm in}(t)$ but also δv_1 or δv_2. A_1A_2 times amplified δv_1 is much higher than A_2 times amplified δv_2. The noise floor of the system is mainly affected by δv_1. b) Typical voltage spectral density amplified by a noiseless amplifier (red solid line) and that by a real amplifier (black solid line). This graph is shown in a log-log plot.

4.2 Straightforward Method

The straightforward method to measure noise is the simplest way that we can think of, although it has defects. We describe this approach and the resulting typical noise spectral density in Fig. 4.2. A typical power spectrum density is shown in the right panel of Fig. 4.2. For the high-frequency region, the effect of the RC low-pass filter comprising $R_{\rm m}$ and capacitor ($C_{\rm coax}$) of the coaxial cables appears as

$$\Delta V_{\rm in}(t)\left|\frac{1}{1+i\omega C_{\rm coax}R_{\rm m}}\right|,$$

where ω is the angular frequency. The low-pass filter decreases the white noise regime below several 10 kHz when the sample is in the quantum Hall regime. This method not only avoid extrinsic noise but also decrease measurable bandwidth. Although this system may be proper for measuring the noise for the low-frequency region, it is often difficult to obtain the white noise regime.

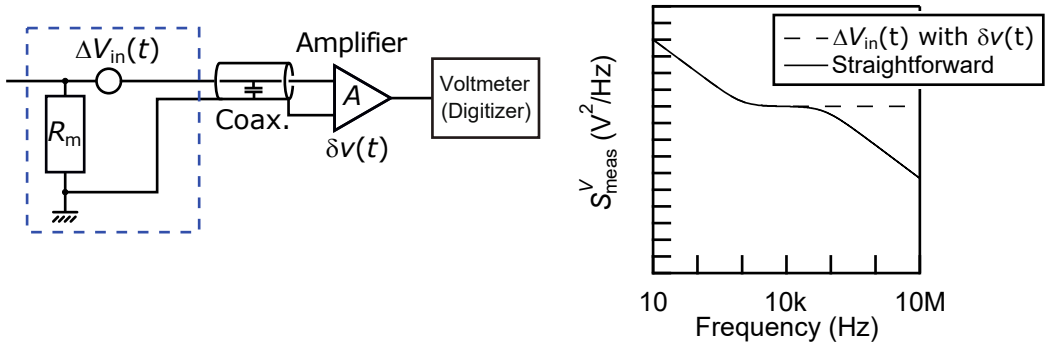

FIGURE 4.2: Straightforward setup for the voltage noise measurement (left), and the expected voltage noise power spectral density (right). The voltage signal $v(t)$ is amplified through the amplifier and recorded at the voltmeter (digitizer). Right panel: Typical power spectrum density of the voltage noise using the straightforward method. The graph is shown in a log-log plot. The black dashed line is a typical voltage spectrum density amplified by a real amplifier [Fig. 4.1 b)].

4.3 Cross-correlation Method

To reduce the extrinsic noise, which is one of the problems of "the straightforward method" in Section 4.2, some researchers implement "the cross-correlation noise measurement" [103, 104]. As shown in Fig. 4.3, the voltage signal, $\Delta V_{in}(t)$, amplified at two different amplifiers A_1 and A_2 is given by $\Delta V^{I}_{out}(t) = \Delta V_{in}(t) + \delta v_1(t)$ and $\Delta V^{II}_{out}(t) = \Delta V_{in}(t) + \delta v_2(t)$, respectively. Here, $\Delta V_{in}(t)$ is transmitted in two paths, Amplifier 1 and Amplifier 2 lines. Both amplifiers have their own extrinsic noise $\delta v_i(t)$ $(i = 1, 2)$. At the digitizer, we compute the cross-correlated spectral density between the two signals $\Delta V^{I}_{out}(t)$ and $\Delta V^{II}_{out}(t)$.

The spectral density is given as

$$\begin{aligned} S^V(t) &= \left\langle \Delta V^{I}_{out}(t) \Delta V^{II}_{out}(t) \right\rangle \\ &= \langle [\Delta V_{in}(t) + \delta v_1(t)] \, [\Delta V_{in}(t) + \delta v_2(t)] \rangle \\ &= \left\langle [\Delta V_{in}(t)]^2 \right\rangle \end{aligned}$$

by taking the cross-correlation. Here, the contributions including the extrinsic signals, $\delta v_1(t)$ and $\delta v_2(t)$, cancel out after long-time averaging since they

are uncorrelated. Consequently, we can record the noise spectral density of only the intrinsic noise, as shown in the right panel of Fig. 4.3. The advantage of the method is that we can obtain only intrinsic noise, which would be impossible to obtain in "the straightforward method" in Section 4.2. This method is often used in mesoscopic experiments, for example, Refs. [5, 76, 103].

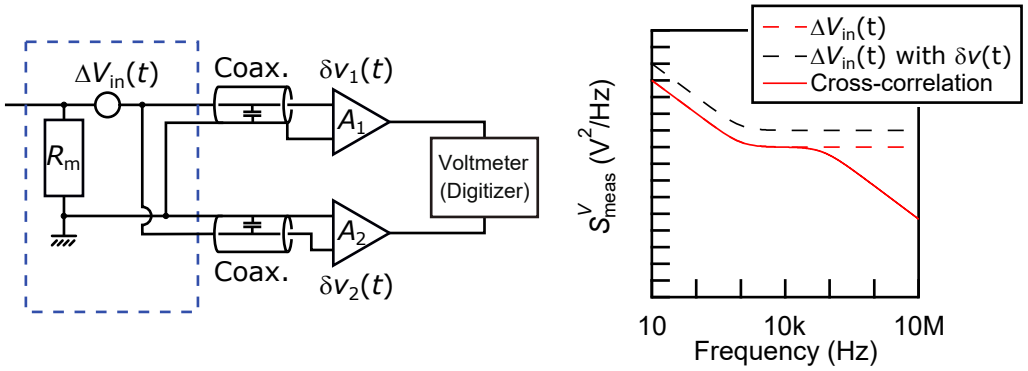

FIGURE 4.3: Cross-correlation method measurement system (left) and the expected voltage noise power spectral density. Right panel: Typical power spectrum density of the voltage noise using the method. The graph is shown in a log-log plot. The red (black) dashed line is a typical voltage spectrum density amplified by noiseless (real) amplifier, as shown in Fig. 4.1 b). The cross-correlation measurement method can reduce extrinsic noise.

4.4 *LC* Circuit Method

It is necessary to avoid the *RC* low-pass filter effect to measure the white noise, excluding $1/f$ noise, which is another problem of "the straightforward method" (Sec. 4.2). We use the inductor-capacitor (*LC*) resonant circuit, as shown in Fig. 4.4 [12, 99, 100, 102, 105]. Near the *LC* resonance frequency, the *RLC* impedance converts the current noise from the R_m to the voltage noise,

$$\begin{aligned} |Z| &= \left| \left[\frac{1}{R_m} + (i\omega L_{in})^{-1} + i\omega C_{coax} \right]^{-1} \right| \\ &= \sqrt{\frac{R_m^2}{1 + R_m^2 \left(\omega C_{coax} - \frac{1}{\omega L_{in}} \right)^2}} \quad . \end{aligned} \tag{4.1}$$

The resonance peak is given by

$$f_o = \frac{1}{2\pi\sqrt{L_{in} C_{coax}}}.$$

To set the resonance peak, we install the amplifier in the refrigerator.

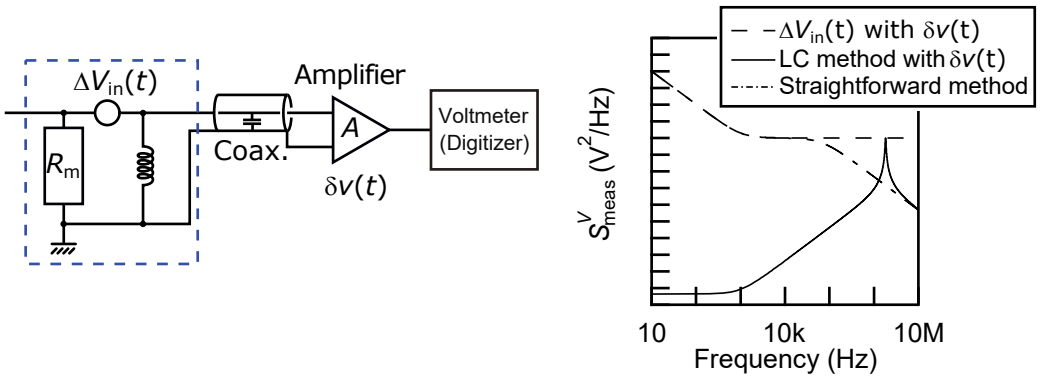

FIGURE 4.4: Measurement setup for the voltage noise with LC tank to shift the measurement band region. The noise only at a resonance frequency is extracted. Right panel: Typical power spectrum density of the voltage noise using this method. The graph is shown in a log-log plot. The black dashed line is a typical voltage spectrum density amplified by real amplifier as shown in 4.1 b).

The purpose of the LC tank is to shift the measurement region, where the influence of the $1/f$ noise is absent. However, the disadvantage is that we measure the noise spectral density only at a resonance frequency; thus, we cannot obtain the full spectra.

Equation (4.1) expresses the power spectrum density as a function of frequency. Because Eq. (4.1) is the square root of the Lorentzian function, we can fit the measured noise spectral density to the noise spectrum power, as shown in Fig. 4.5. The noise power corresponds to the peak of the Lorentzian function (right panel of Fig. 4.4). To extract the height of the peak, we fit the Lorentzian function,

$$P(f) = P_B + \frac{P_0}{1 + \left(f^2 - f_o^2\right)^2 / \left(f\Delta f_{3dB}\right)^2}, \tag{4.2}$$

where P_B is the background noise, and Δf_{3dB} is the full width at half maximum of the peak.

The resonance peak is slightly distorted from the Lorentzian line shapes expected for an ideal RLC resonance circuit. This distortion is due to the parasitic resistance r in the RLC tank circuit and the parasitic capacitances in the high electron mobility transistor (HEMT) used in the cryogenic amplifier. The details of this will be explained in Chapter 5

4.5 Noise Model

To extract S^I from P, which is the same as S^V, the noise measurement system must be calibrated. An effective circuit of Fig. 4.4 is shown in Fig. 4.6. The intrinsic current noise, $\Delta I_{in}(t)$, and the extrinsic current noise, $\delta i(t)$, are

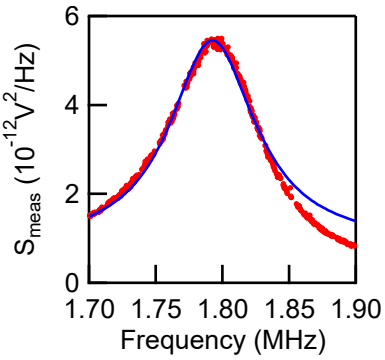

FIGURE 4.5: Power spectral densities P obtained from noise data acquired from the quantum point contact on GaAs/AlGaAs heterostructure. The blue line is the fitting function of Eq. (4.2) over the range 1.7 to 1.85 MHz. The details will be explained in Chapter 5

converted to the voltage noise. The amplified voltage noise, $\Delta V_{\text{out}}(t)$, is expressed as

$$\Delta V_{\text{out}} = A\left[\left(\Delta I_{\text{in}} + \delta i\right) Z + \delta v\right].$$

The amplified voltage spectral density, $S^V(\omega)$, is

$$\begin{aligned} S^V &\equiv \left\langle \Delta V_{\text{out}}^2 \right\rangle \\ &= \left\langle A^2 \left[\left(\Delta I_{\text{in}} + \delta i\right) Z + \delta v\right]^2 \right\rangle \\ &= A^2 \left[\left(\left\langle \Delta I_{\text{in}}^2 \right\rangle + \left\langle \delta i^2 \right\rangle\right) Z^2 + \left\langle \delta v^2 \right\rangle\right] \\ &= A^2 \left[\left(S_{\text{m}}^I + S_{\text{AMP}}^I\right) Z^2 + S_{\text{AMP}}^V\right], \end{aligned} \tag{4.3}$$

where Z is RLC impedance, as shown in Eq. (4.1), S_{m}^I is current noise power spectral density of the mesoscopic sample, S_{AMP}^I is input-referred current noise power spectral density, and S_{AMP}^V is input-referred voltage noise power spectral density of the amplifier. Following the calibration, S_{AMP}^I and S_{AMP}^V are extracted from thermal noise measurements. The details will be discussed in Chapter 5.

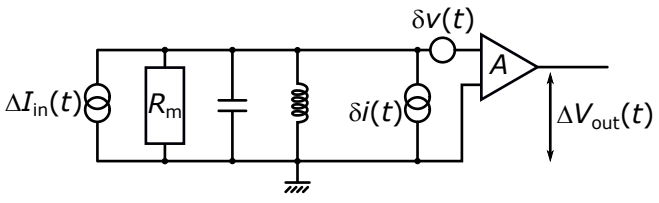

FIGURE 4.6: Circuit model used for LC circuit methods. The $\Delta V_{\text{out}}(t)$ extraction of the noise of the mesoscopic sample S^I.

Chapter 5

Development of Cryogenic Amplifier

5.1 Purpose of This Experiment

Over the last 30 years, shot noise in the mesoscopic system has provided important information on the microscopic scattering properties of quantum transport [2–4]. The electric current corresponds to the average number of electrons that pass through the system for a finite time. In the electric current, the noise or equivalently fluctuation, is the fluctuation of the number of electrons passing through the system. The noise measurement is unique because it gives information that is not available by the conventional conductance measurement.

So far, researchers have reported many noise experiments. For example, shot noise measurements in quantum point contact (QPC) [75, 103, 106–111], diffusive wire [112, 113], quantum dot [114–117], tunnel junctions [118], and magnetic tunnel junctions [119, 120] have been reported. Shot noise has also been used to probe many-body physics, such as fractional quantum charge [5–7], Cooper pair [121], spin-dependent transport in a QPC [108–110], quantum wire [122], Kondo effect [9–11, 123], quantum dots in the sequential tunneling [116], and cotunneling [115, 117] regimes.

The noise power spectral density quantifies the noise. As discussed in Chapter 4 most usually, it is obtained via fast Fourier transformation (FFT) of the time-domain signal of the current either in an autocorrelation [12, 99, 100, 102, 124] or a cross-correlation measurement [12, 99, 100, 124]. In all cases, many efforts are required to obtain an accurate noise signal, such as using an inductor-capacitor (LC) resonant circuit [12, 99, 100, 102], reducing the extrinsic noise from a cryogenic amplifier [102], and widening the frequency regime for the averaging [124]. The experimental study of anyonic statistics at the fractional quantum Hall system using the current noise measurement is recently reported [14]. The deviation of the noise measurement seems to be about 0.1×10^{-29} A^2/Hz. We believe that the high accuracy of the system would lead to measure much deeper mesoscopic physics.

It is well known by the central limit theorem that N times more data is required for $\sqrt{N}$ times more accurate signal. Naturally, measuring the noise for an extensive time to achieve a high signal-to-noise ratio has a practical limitation. In this sense, improving the high electron mobility transistors

(HEMTs) used in the cryogenic amplifiers themselves would be a good strategy. Researchers usually use commercially available HEMTs, such as AVAGO ATF-35143 (Avago Technologies, referred to as "ATF HEMT" below), shown in Fig. 5.1. They are designed for a GHz frequency regime at room temperature, which could not be optimized for the use in the MHz frequency regime at low temperature, where most of the mesoscopic noise measurements are performed. We expect that reducing the noise from the HEMT in cryogenic amplifiers is the key to a highly accurate noise measurement system. By using the improved HEMTs, the accuracy increase on the already reported amplifiers. There are several types of research on the fabrication of the homemade HEMT using GaAs/AlGaAs wafers [125–127].

Here, we describe how to improve the cryogenic amplifier with a homemade HEMT. This Chapter presents the components of a GaAs/AlGaAs wafer of homemade HEMTs for a cryogenic amplifier designed for higher transconductance. We measure the intrinsic properties of the HEMT and the properties of cryogenic amplifiers, which include the HEMT. We demonstrate the measurement of current noise in a gate defined GaAs/AlGaAs QPC.

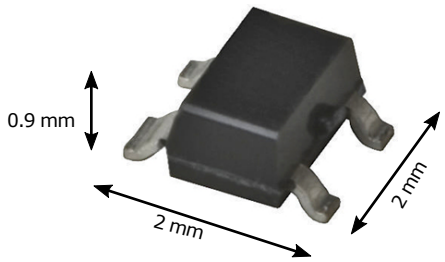

FIGURE 5.1: Commercial high-electron-mobility transistor (HEMT) (Avago Technologies ATF-35143).

5.2 Principles of the Development

5.2.1 GaAs/AlGaAs Heterostructure as HEMT

Since 1979, Takashi Mimura and Satoshi Hiyamizu have researched GaAs HEMT (high-electron-mobility transistor) in Fujitsu Laboratories [17, 18]. They achieved fabricating GaAs/AlGaAs heterostructure, which has a high-speed performance superior to that of Si MOSFETs. Stable operation of it is the top priority for radio telescopes and was a significant HEMT strong point at that time, compared to the parametric amplifiers being used. In mesoscopic physics, this GaAs/AlGaAs heterostructure is a fascinating playground for researchers to see various quantum effects. In this thesis, we follow the birth background of the GaAs/AlGaAs heterostructure as HEMT. We use this as a HEMT for the current noise measurement system.

5.2.2 Voltage Amplifier

There are several types of amplifiers. Many researchers have developed designs of amplifiers to reduce the $1/f$ noise [102] or to widen bandwidth [124]. In this work, we only focus on the voltage amplifier, as discussed in Chapter 4.

Here, we explain the characteristics of a common source circuit with fixed bias "CS1", as shown in Fig. 5.2 a), with a gate supply voltage V_{g} and a drain one V_{DD}. The 330 kΩ resistor and the 100 nF capacitor connected to the HEMT gate form an RC filter that attenuates high-frequency extrinsic noise from the gate supply. For a set of V_{g} and V_{DD}, the gain

$$A_{\mathrm{CS1}}\left(V_{\mathrm{g}}, V_{\mathrm{DD}}\right) \equiv \frac{\partial V_{\mathrm{out}}(V_{\mathrm{g}}, V_{\mathrm{DD}})}{\partial V_{\mathrm{g}}} \tag{5.1}$$

is given by[1]

$$A_{\mathrm{CS1}} = -g_{\mathrm{m}} \frac{R_{\mathrm{D}}}{1 + R_{\mathrm{D}} g_{\mathrm{ds}}} = -g_{\mathrm{m}} Z_{\mathrm{out}}, \tag{5.2}$$

where

$$g_{\mathrm{m}}\left(V_{\mathrm{g}}, V_{\mathrm{ds}}\right) \equiv \frac{\partial I_{\mathrm{ch}}\left(V_{\mathrm{g}}, V_{\mathrm{ds}}\right)}{\partial V_{\mathrm{g}}}, \tag{5.3}$$

and

$$g_{\mathrm{ds}}\left(V_{\mathrm{g}}, V_{\mathrm{ds}}\right) \equiv \frac{\partial I_{\mathrm{ch}}\left(V_{\mathrm{g}}, V_{\mathrm{ds}}\right)}{\partial V_{\mathrm{ds}}}. \tag{5.4}$$

This leads to

$$A_{\mathrm{CS1}} = -R_{\mathrm{D}} \frac{\partial I_{\mathrm{ch}}\left(V_{\mathrm{g}}, V_{\mathrm{DD}}\right)}{\partial V_{\mathrm{g}}}. \tag{5.5}$$

Here, g_{m} is the transconductance, g_{ds} is the drain conductance, R_{D} is the load resistance,

$$Z_{\mathrm{out}} = \frac{R_{\mathrm{D}}}{1 + R_{\mathrm{D}} g_{\mathrm{ds}}} \tag{5.6}$$

is the output impedance of the amplifier, $V_{\mathrm{ds}} = V_{\mathrm{DD}} - R_{\mathrm{D}} I_{\mathrm{ch}}$ is the voltage between the drain and source of the HEMT, and $I_{\mathrm{ch}}\left(V_{\mathrm{g}}, V_{\mathrm{ds}}\right)$ is the current flowing in the HEMT channel. The other common source circuit with self-bias "CS2", is shown in Fig. 5.2 b). It has the advantage that we do not have to apply V_{g} because the effective V_{g} is applied to the HEMT due to the R_{S}. We will use a CS2-type amplifier in a real noise measurement system.

[1] Because $V_{\mathrm{ds}} = V_{\mathrm{DD}} - R_{\mathrm{D}} I_{\mathrm{ch}}$, $\frac{dV_{\mathrm{ds}}}{dV_{\mathrm{g}}} = -R_{\mathrm{D}} \frac{dI_{\mathrm{ch}}}{dV_{\mathrm{g}}}$. Note that this $\frac{dI_{\mathrm{ch}}}{dV_{\mathrm{g}}} \neq g_{\mathrm{m}}$. The ΔI_{ch} is given by $\Delta I_{\mathrm{ch}} = g_{\mathrm{m}} \Delta V_{\mathrm{g}} - g_{\mathrm{ds}} \Delta V_{\mathrm{ds}}$, thus $\frac{dI_{\mathrm{ch}}}{dV_{\mathrm{g}}} = g_{\mathrm{m}} - g_{\mathrm{ds}} \frac{dV_{\mathrm{ds}}}{dV_{\mathrm{g}}}$. Therefore,

$$\begin{aligned} \frac{dV_{\mathrm{ds}}}{dV_{\mathrm{g}}} &= -R_{\mathrm{D}} \left(g_{\mathrm{m}} - g_{\mathrm{ds}} \frac{dV_{\mathrm{ds}}}{dV_{\mathrm{g}}} \right) \\ \rightarrow \quad A = \frac{dV_{\mathrm{ds}}}{dV_{\mathrm{g}}} &= \frac{-R_{\mathrm{D}} g_{\mathrm{m}}}{1 + R_{\mathrm{D}} g_{\mathrm{ds}}}. \end{aligned}$$

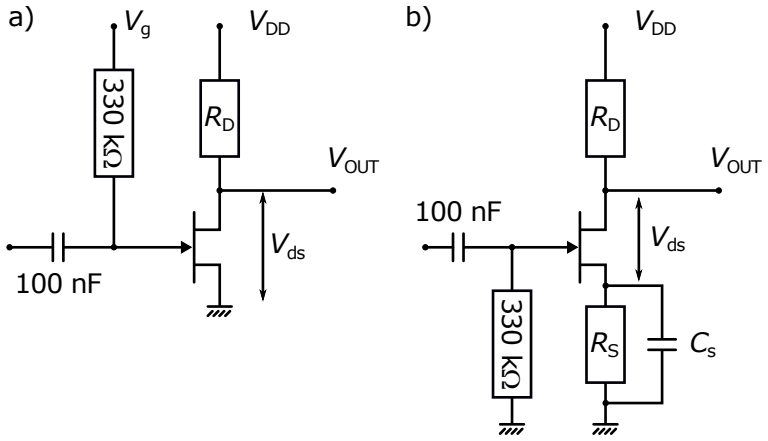

FIGURE 5.2: a) Schematic diagram of the common-source circuit with fixed bias "CS1". b) Schematic diagram of the common-source circuit with self-bias "CS2".

The signal-to-noise ratio in the first amplification step, namely, the cryogenic part in Fig. 4.4, governs the resolution of the measurement system as described in Chap. 4. While the cryogenic amplifier converts S^I_{in} to $S^V_{\text{in}} \equiv \langle \Delta V^2_{\text{in}} \rangle$ in conjunction with the LC tank circuit, it also generates extrinsic noise, which interferes with S^I_{in}. With this extrinsic noise included, the relation between S^I_{in} and S^V_{out} can be described by Eq. (4.3). When the gate leakage current of the HEMT is negligible, both S^I_{HEMT} and S^V_{HEMT} originate exclusively from the current noise $S^I_{\text{ch}} \equiv \langle \Delta I^2_{\text{ch}} \rangle$ in the HEMT channel generated by the finite source-drain voltage [128].

At cryogenic temperature, S^I_{ch} is given by [125]

$$S^I_{\text{ch}} \simeq S^I_{\text{ch-}1/f} + S^I_{\text{ch-shot}}, \tag{5.7}$$

where $S^I_{\text{ch-}1/f}$ and $S^I_{\text{ch-shot}}$ are the power spectral densities of the $1/f$ noise and the shot noise generated in the HEMT channel, respectively. It is empirically known that $S^I_{\text{ch-}1/f}$ increases in proportion to I^2_{ch} and decreases in inverse proportion to the total number of charge carriers [129]. On the other hand, $S^I_{\text{ch-shot}}$ is proportional to I_{ch} as

$$S^I_{\text{ch-shot}} = 2eI_{\text{ch}}F, \tag{5.8}$$

where F is the so-called Fano factor ($0 \leq F \leq 1$).

The gain, $|A_{\mathrm{CS1}}| \propto \partial I_{\mathrm{ch}}/\partial V_{\mathrm{g}}$, monotonically increases with $P = V_{\mathrm{DD}} I_{\mathrm{ch}}$ because

$$\begin{aligned} P &= V_{\mathrm{DD}} I_{\mathrm{ch}}\left(V_{\mathrm{DD}}, V_{\mathrm{g}}\right) \\ &= I_{\mathrm{ch}}^2\left(V_{\mathrm{DD}}, V_{\mathrm{g}}\right)\left(R_{\mathrm{D}} + \frac{1}{g_{\mathrm{ds}}}\right) \\ &= I_{\mathrm{ch}}^2\left(V_{\mathrm{DD}}, V_{\mathrm{g}}\right)\left(R_{\mathrm{D}} + \frac{1}{\left.\frac{\partial I_{\mathrm{ch}}\left(V_{\mathrm{g}}, V_{\mathrm{ds}}\right)}{\partial V_{\mathrm{ds}}}\right|_{V_{\mathrm{g}}}}\right) \\ &\propto I_{\mathrm{ch}}^2(V_{\mathrm{DD}}, V_{\mathrm{g}}) \end{aligned} \tag{5.9}$$

Therefore,

$$A \propto \frac{\partial I_{\mathrm{ch}}(V_{\mathrm{DD}}, V_{\mathrm{g}})}{\partial V_{\mathrm{g}}} \propto \sqrt{P}. \tag{5.10}$$

S^V_{HEMT} decreases in inverse proportion to $\sqrt{P}$, because

$$\begin{aligned} S^V_{\mathrm{HEMT}} &\simeq \frac{S^V_{\mathrm{out}}}{|A_{\mathrm{dc}}|^2} = \frac{S^I_{\mathrm{ch}} R_{\mathrm{D}}^2}{|A_{\mathrm{dc}}|^2} \simeq \frac{S^I_{\mathrm{ch\text{-}shot}} R_{\mathrm{D}}^2}{|A_{\mathrm{dc}}|^2} \\ &= \frac{2eI_{\mathrm{ch}} F R_{\mathrm{D}}^2}{\left(R_{\mathrm{D}} \frac{\partial I_{\mathrm{ch}}\left(V_{\mathrm{DD}}, V_{\mathrm{g}}\right)}{\partial V_{\mathrm{g}}}\right)^2} \propto \frac{\sqrt{P}}{P} = \frac{1}{\sqrt{P}}. \end{aligned} \tag{5.11}$$

5.2.3 Measurement Setup

We install a cryogenic CS amplifier in a standard measurement setup comprising an inductor-capacitor (LC) tank circuit [12, 101, 102]. Figure 5.3 a) shows a block diagram of our setup installed in a dilution refrigerator, and Fig. 5.3 b) illustrates a circuit model of the cryogenic assembly. A bias voltage V_{bias} is applied to generate a current I_{m} flowing into a mesoscopic device (resistance R_{m}) at mixing-chamber (MC) temperature. The transmitted current I_{in} flows down to the cold ground through $L_{\mathrm{in}} = 33\ \mu$H placed on the MC plate. Note that, even if I_{m} is noiseless, the current flowing through the device may reflect the discrete nature of electron charge, leading to the fluctuation ΔI_{in} in I_{in}. The inductor forms the LC tank circuit with capacitance C_{in}, mainly composed of the parasitic capacitance C_{coax1} of the coaxial cable. Near the LC resonance frequency, ΔI_{in} yields voltage noise $\Delta V_{\mathrm{in}} = Z_1 \times \Delta I_{\mathrm{in}}$, where

$$Z_1 = \left[\frac{1}{R_{\mathrm{m}}} + (i\omega L_{\mathrm{in}} + r)^{-1} + i\omega C_{\mathrm{in}}\right]^{-1} \tag{5.12}$$

is the parallel impedance of the mesoscopic device and the tank circuit. Here, r is the total parasitic resistance of the inductor and the coaxial cable. The voltage noise is amplified to ΔV_{out} by the cryogenic amplifier and again amplified to ΔV_{meas} by a commercial amplifier (NF Corporation SA-220F5,

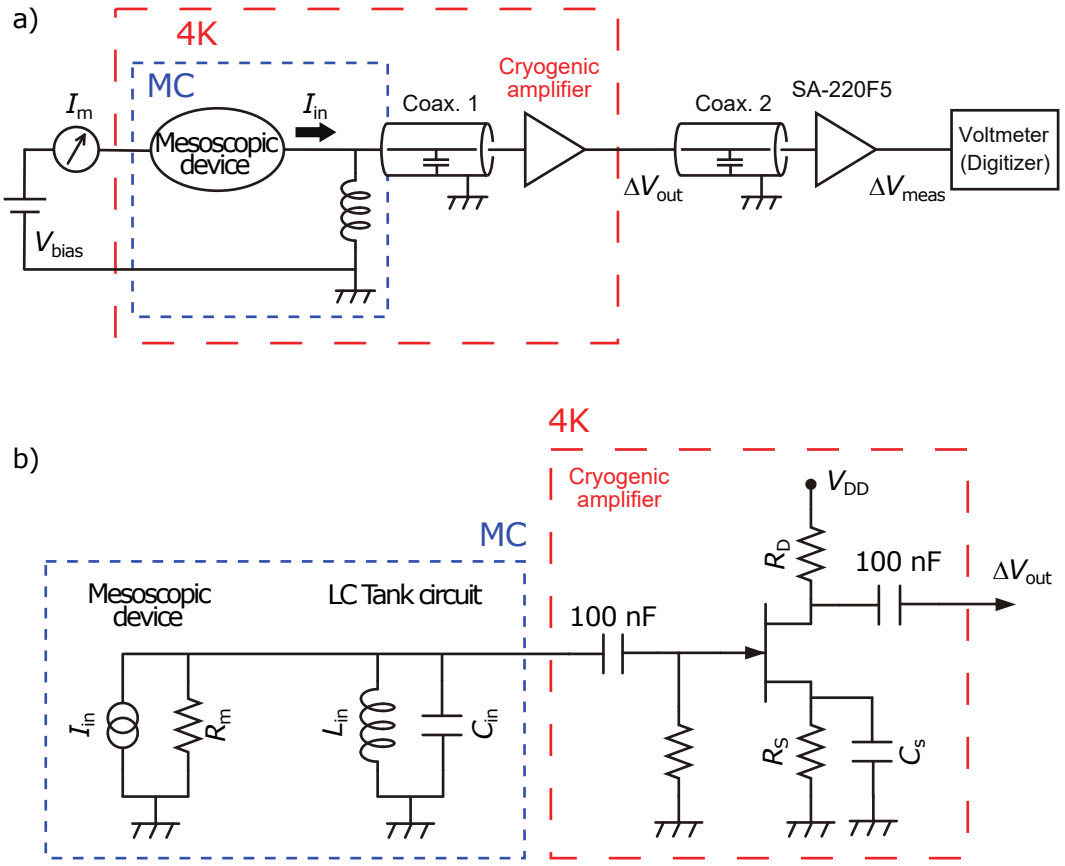

FIGURE 5.3: a) Schematic diagram of the noise-measurement setup using an LC tank circuit. Mesoscopic device and amplifiers are connected via CuNi coaxial cables, Coax. 1 and Coax. 2 with parasitic capacitances C_{coax1} and C_{coax2}, respectively. A cryogenic amplifier is placed on 4 K stage of the dilution refrigerator. b) Electronic circuit model of the cryogenic assembly.

46 dB) at room temperature. The measurement is completed by recording ΔV_{meas} using a digitizer (National Instruments PXI-5922) that provides a high-speed voltmeter. We analyze the time-domain data using FFT technique to evaluate $S^I_{\mathrm{in}} \equiv \langle \Delta I^2_{\mathrm{in}} \rangle$ from the FFT spectrum $S^V_{\mathrm{meas}} \equiv \langle \Delta V^2_{\mathrm{meas}} \rangle$.

In this Chapter, we focus on Johnson and shot noise in the low-frequency white-noise region ($f \ll k_{\mathrm{B}} T_e/h$ and eV_{bias}/h, where e is the elementary charge, h is the Planck constant, k_{B} is the Boltzmann constant, and T_e is electron temperature). However, at very low frequencies (typically below 100 kHz), these noises are buried in the $1/f$ noise generated in the mesoscopic sample or the cryogenic HEMT amplifier or both. To avoid the $1/f$ noise, we designed the LC resonance frequency $f_o = \left(2\pi\sqrt{L_{\mathrm{in}} C_{\mathrm{in}}}\right)^{-1}$ to be near 1.8

MHz, where the $1/f$ noise is expected to be small, by choosing $L_{\text{in}} = 33\ \mu\text{H}$ and $C_{\text{in}} \simeq C_{\text{coax1}} \simeq 240$ pF.

5.3 Results and Discussions

5.3.1 HEMT

In principle, S^V_{HEMT} can be suppressed by increasing $g_{\text{m}} \equiv \Delta I_{\text{ch}}/\Delta V_{\text{g}}$ while keeping S^I_{ch} low. For this purpose, we fabricate HEMTs using a GaAs/AlGaAs heterostructure and gate patterns that are designed to be suitable for high g_{m}. Transport properties of the homemade HEMTs are measured at temperatures below 4.2 K, where these HEMTs show no significant temperature dependence. We note that the major features of the transport properties are unchanged after several cooldowns.

Design

Figure 5.4 shows a schematic of the HEMT fabricated from a GaAs/$Al_{0.33}Ga_{0.67}As$ heterostructure grown by molecular beam epitaxy on a semi-insulating GaAs substrate. The heterostructure is modulation-doped with silicon at two δ

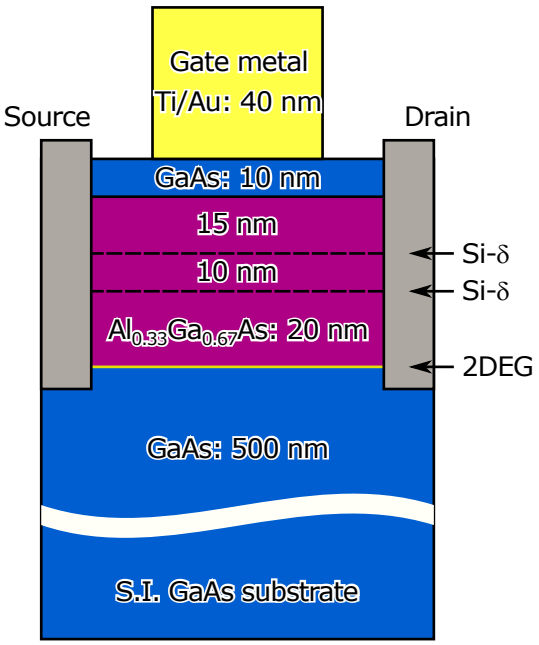

FIGURE 5.4: Schematic of the HEMT structure fabricated in 2DEG in GaAs/AlGaAs heterostructure.

planes (doping level of 6×10^{12} cm^{-2} for each). The two-dimensional electron gas (2DEG) located 55 nm below the surface has electron density $n_e = 4.0 \times 10^{11}$ cm^{-2} and mobility $\mu = 3.2 \times 10^5$ cm^{2}V^{-1}s^{-1} at 4.2 K. The shallow depth and the high electron density of the 2DEG are advantageous for increasing g_{m}.

Our HEMT was patterned using photolithography for fabricating mesa structures, ohmic contacts of Au-Ge-Ni alloys, and a gate electrode of 10-nm-thick titanium and 30-nm-thick gold.

For a given GaAs/AlGaAs heterostructure, the HEMT characteristics are determined by the geometry of the gated region: the gate length L and the channel width W. For examining g_m and the noise characteristics depending on L and W, we fabricated five sorts of HEMTs having different sets (W; L) on the same wafer. Four of them have (W; L) = (1 mm; 2, 4, 16, or 64 μm), and the other has (3 mm; 4 μm) [see Fig. 5.5 for an example].

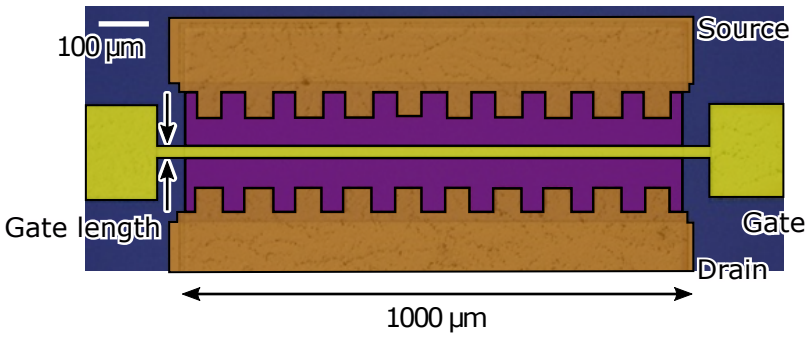

FIGURE 5.5: False-color optical micrograph of a (W; L) = (1 mm; 16μm) HEMT. The meander structure of source and drain electrodes is for suppressing the ohmic contact resistances.

Characteristic of High Electron Mobility Transistors

Figure 5.6 a) presents V_g-I_{ch} traces of four HEMTs with different L and ATF HEMT measured at $V_{ds} = 0.27$ V below 1 K. For a shorter L, a more negative V_g is necessary to pinch off the channel. Concomitantly, the slope of the traces becomes steeper for a shorter L, resulting in a higher g_m. The g_m of ATF HEMT is much smaller than the g_m of homemade HEMT. Figure 5.6 b) displays the V_g dependence of g_m of HEMTs obtained by numerically differentiating I_{ch} with respect to V_g. While the 4-μm HEMT shows a single gentle peak of height $g_m \simeq 80$ mS, the 2-μm one shows a double peak reflecting the irregular structure in the pinch-off trace [indicated by the vertical arrow in Fig. 5.6 a)]. The peak height of g_m is about 25 mS. The double-peak structure is sensitive to a slight change in V_{ds}, causing instability of the HEMT. Similar irregular features are observed in several 2-μm HEMTs, while the details differ from HEMT to HEMT. We consider that the irregularities originated from unintentional tunneling through impurities or defects in the gated region. Note that a higher V_{ds} sometimes induces similar irregularities even in the HEMTs with longer L. However, the typical V_{ds} value, where such irregularity appears in a longer L HEMT, is much higher than that of a 2-μm HEMT. Thus, we conclude that a 4-μm HEMT is best suited for the present study because of its high stability and high g_m.

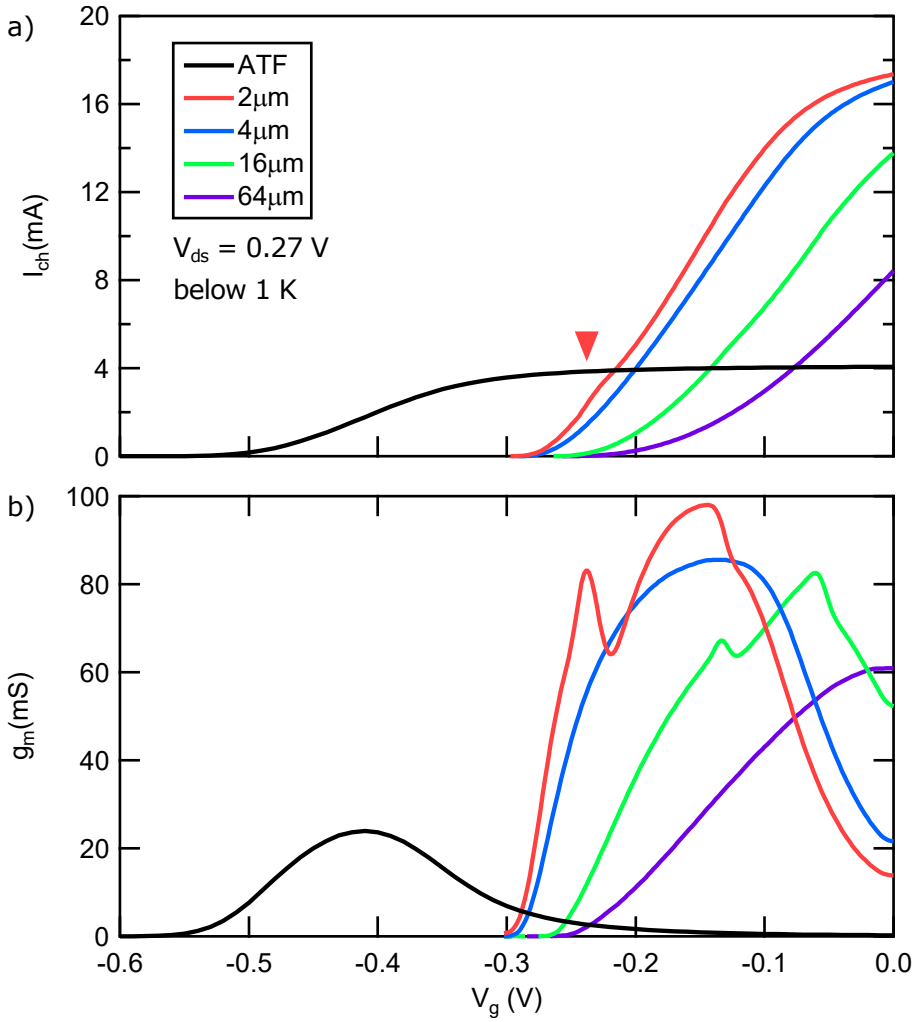

FIGURE 5.6: a) V_g dependence of I_{ch} of four HEMTs with different L, and ATF HEMT at $V_{ds} = 0.27$ V. b) V_g dependence of g_m of five HEMTs with $L = 2, 4, 16$, and 64 μm of homemade HEMTs and ATF HEMT.

Figure 5.7 a) presents the pinch-off characteristics of the (3 mm; 4 μm) and (1 mm; 4 μm) HEMTs measured at V_{ds} = 0.5 V at 4.2 K [2]. Since the pinch-off characteristics of ATF HEMT at $V_{ds} = 0.5$ V are unstable, it is not shown. While the pinch-off voltages are similar, the 3-mm HEMT shows more than twice as steep I_{ch} as the 1-mm one at -0.25 V $< V_g < -0.18$ V. In the g_m-V_g plot shown in Fig. 5.7 b), g_m of the 3-mm HEMT at $V_g = -0.19$ V reaches $\sim$260 mS, which is about 2.5 times as large as that of the 1-mm one.

Figures 5.8 shows the V_{ds} dependence of I_{ch} of the (3 mm; 4 μm) and (1 mm; 4 μm) HEMTs measured at several V_g values between -0.20 and -0.26

[2]The saturation of I_{ch} near 20 mA for $W = 3$ mm HEMT is due to parasitic resistance of about 25 Ω, which is the sum of the ohmic contact resistance and the wiring resistance. We do not observe such saturation for the $W = 1$ mm HEMT over the measured V_g range because of its smaller contact resistance and the resultant smaller total parasitic resistance (about 20 Ω).

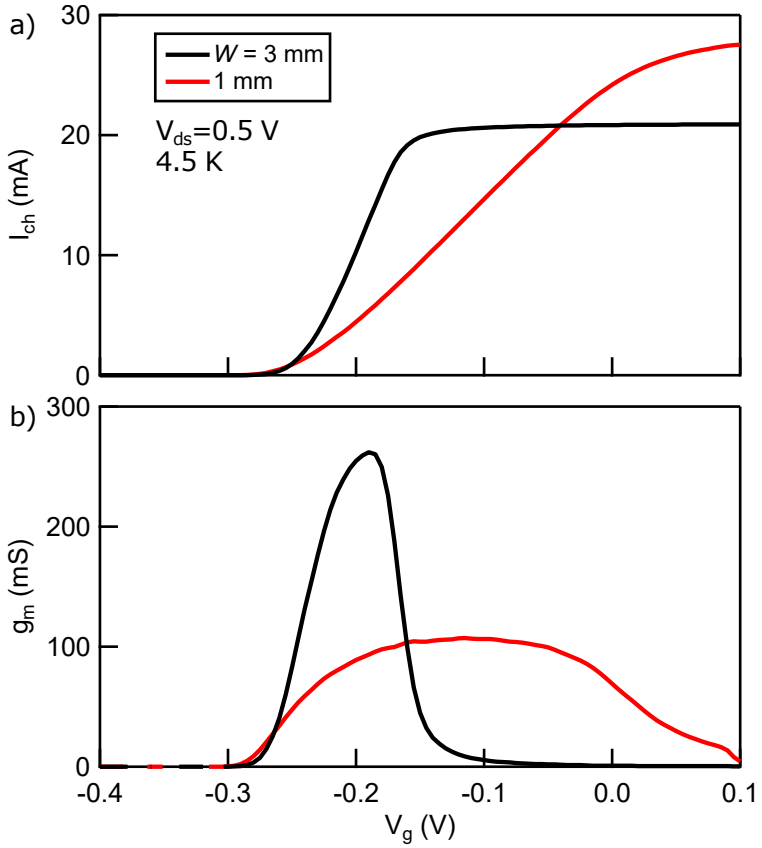

FIGURE 5.7: a) V_{g} dependence of I_{ch} of two HEMTs with W = 3 mm and W = 1 mm at $V_{\mathrm{ds}} = 0.5$ V. b) g_{m} corresponding to the case shown in a). Since the characteristics of ATF HEMT is unstable, it is not shown.

V. The drain conductance at a given set of (V_g, V_{ds}) can be evaluated by differentiating I_{ch} with respect to V_{ds}; for example, at (V_g, V_{ds}) = (−0.25 V, 0.5 V), we find $g_{ds} \simeq 0.52$ mS for the $W = 3$ mm HEMT and 0.24 mS for the $W = 1$ mm one.

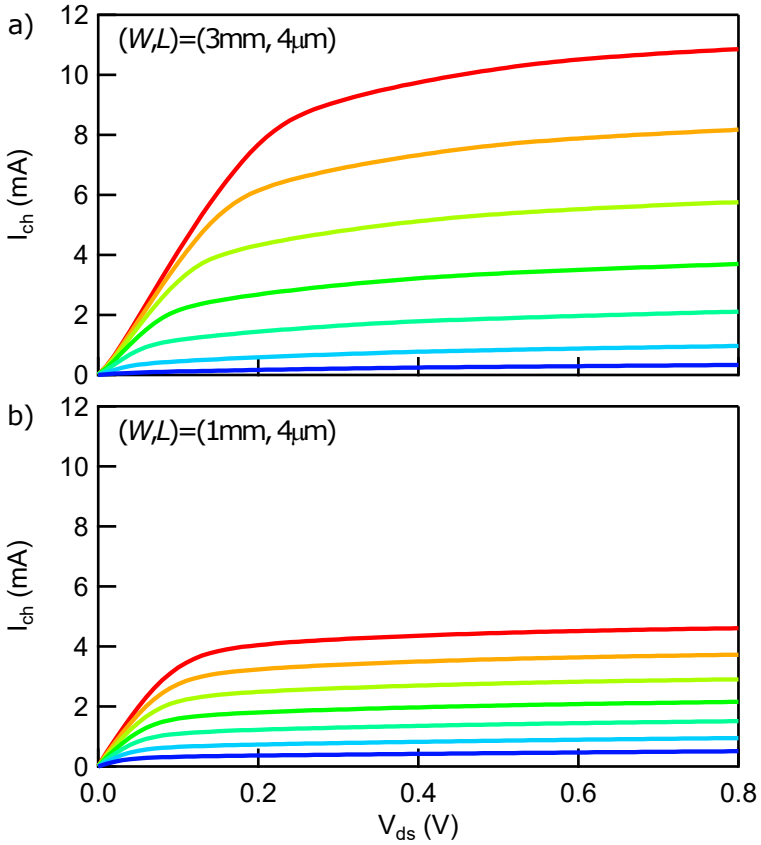

FIGURE 5.8: a) V_{ds}-I_{ch} traces of (W; L) = (3 mm; 4 μm) HEMT measured at several V_g values from −0.20 V (red) to −0.26 V (purple) in 0.01 V steps. b) V_{ds}-I_{ch} traces of (W; L) = (1 mm; 4 μm) HEMT in the same range of V_g.

5.3.2 Voltage Amplifier

Design

To reduce the extrinsic noise, several RC filters are embedded in "CS1". Figure 5.9 shows an equivalent circuit and values for passive components to reduce the extrinsic noise and to stabilize the temperature of the amplifier. R_m placed in the mixing chamber (M/C) is used to investigate the property as the amplifier. To test the amplifier with ATF-35143, we use the 1 kΩ resistor as R_m. For the amplifier with the homemade HEMT, the QPC device is used as R_m.

C_1 is used to block the dc current to the sample. The low-pass filters are designed with R_1 (= 470 kΩ) and C_2 (= 110 nF), whose cut-off frequency f_c is set to ∼3 Hz, R_2 = 100 kΩ is set to reduce extrinsic noise. The components of R_D (= 500 Ω) and C_3 (= 110 nF), which have $f_c \simeq 3$ kHz, are inserted

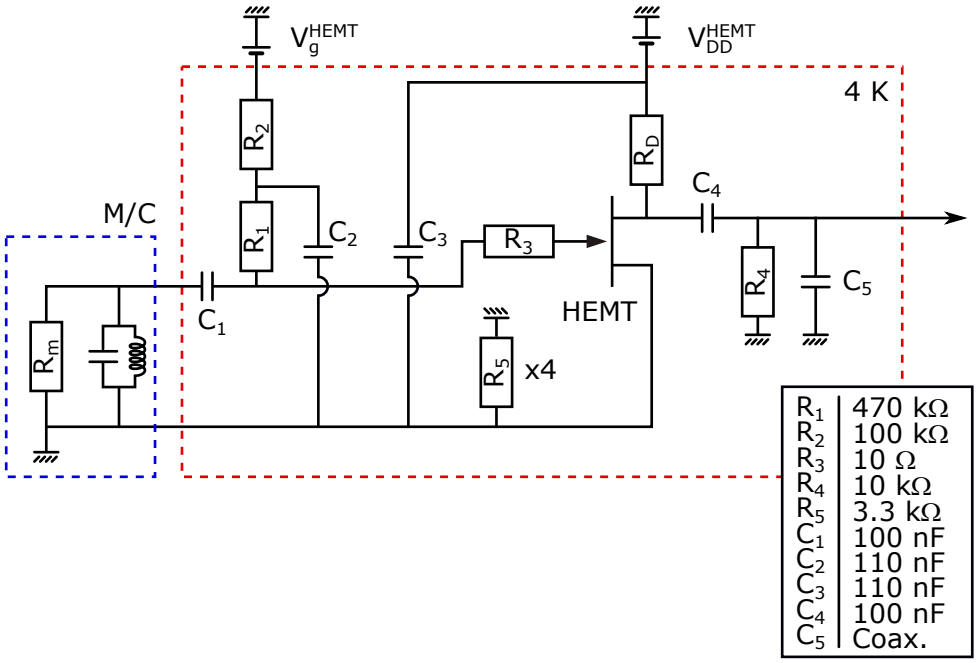

FIGURE 5.9: Circuit diagram of "CS1" with several RC filters.

to suppress the extrinsic noise from the outside. R_3 (=10 Ω) is embedded to protect the HEMT from accidental high voltage damage. R_4 ($= 10$ kΩ) is embedded to discharge the dc voltage between the capacitors at the end of the cryogenic amplifier, C_4, and the room temperature amplifier. C_4 is inserted to block the dc current, $V_{\rm DD}^{\rm HEMT}/R_{\rm D}$, toward the room temperature amplifier, and C_5 phenomenologically represents a parasitic capacitance between the amplifiers. The combined C_5 and $Z_{\rm out}^{\rm HEMT}$ reduce the AC signal from the device. The voltage amplifier is placed at the 4 K station, whose temperature is stable separately from the M/C temperature. The four parallel resistors ($R_5 = 3.3$ kΩ $\times$ 4) are connected to the electrical ground of the amplifier to anchor the temperature of the amplifier in four kelvin.

DC Transport Properties

The voltage amplifier is fabricated and evaluated using several HEMTs. Figure 5.10 a) represents the current and $g_{\rm m}$ when $R_{\rm D}$ (=500 Ω) is installed as a test at $V_{\rm DD}^{\rm HEMT} = 1.0$ V in 4 K station.

Figure 5.10 a) shows the $V_{\rm g}$ dependence of $I_{\rm ch}$ and Fig. 5.10 b) shows $V_{\rm g}$ dependence of $|A|$ at $V_{\rm DD} = 1.0$ V, while ATF HEMT circuits were measured at $V_{\rm DD} = 0.4$ V [3]. When $V_{\rm g}$ is decreased from 0 V, we observe $I_{\rm ch} \simeq V_{\rm DD}/R_{\rm D}$ down to a threshold $V_{\rm g}$ value [e.g., -0.24 V for the (3 mm; 4 μm) HEMT], where the resistance of the HEMT channel becomes comparable to $R_{\rm D}$. When $V_{\rm g}$ is further decreased, $I_{\rm ch}$ decreases to zero, showing a finite $|A|$ along the way. Here, we choose the $|A|$ peak as the operating point. For example, the

[3] The commercial HEMT becomes unstable above $V_{\rm DD} = 0.4$ V.

operating point of the (3 mm; 4 μm) HEMT is set at $V_g = -0.26$ V, where $|A| \simeq 32$, at $V_{DD} = 1.0$ V.

The measured $|A|$ is summarized in Fig. 5.11, as a function of power consumption P. The (3 mm; 4 μm) HEMT shows the highest $|A|$ over the entire range of P [4]. Figure 5.11 represents the gain (=$R_D \times g_m$) following the power

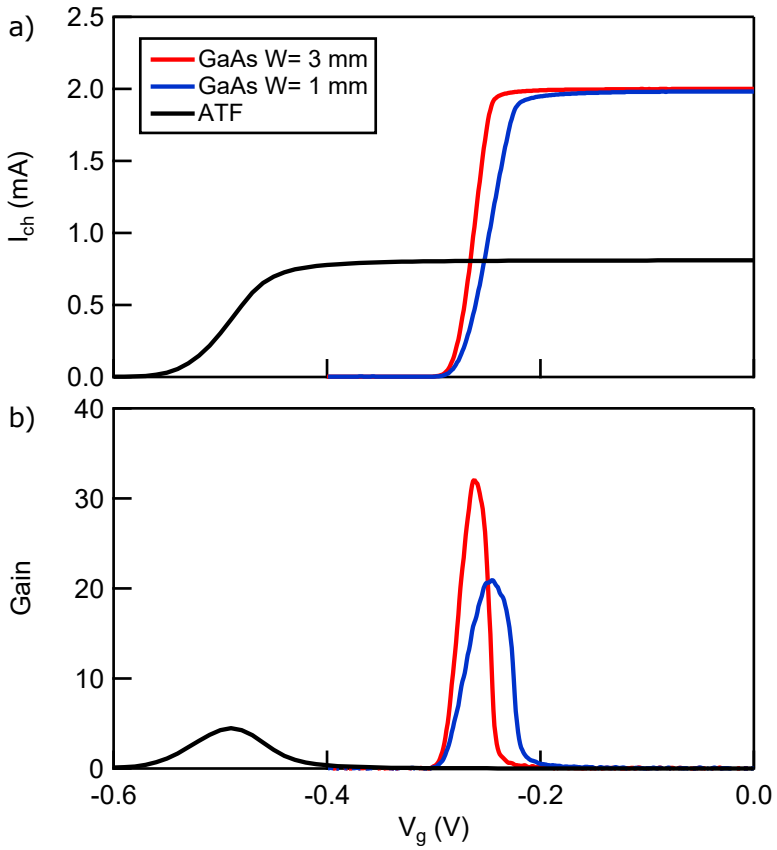

FIGURE 5.10: a) Characteristic of the current and g_m on the gate voltage of the HEMT with 1 mm and 3 mm of the gate width when R_D = 500 Ω at $V_{DD} = 1.0$ V. b)$|A_{CS1}|$ of (1 mm; 4 μm) HEMT circuits. The operating point of the ATF HEMT is much higher than that of the homemade HEMTs, and the gain is much smaller than that of the homemade HEMTs.

consumption of the voltage amplifiers. The gain, $|A| \propto \partial I_{ch}/\partial V_g$, monotonically increases with P, reflecting the $\sqrt{P}$ dependence of I_{ch} as described in Eq. (5.9). The amplifiers should be operated at a lower power than the cooling power (about 1 mW) of the 4 K station of the dilution refrigerator, so the power consumption of the amplifier has to be considered. The HEMT with 3 mm of gate length at the same power consumption has the highest gain and HEMT with 1 mm of the gate width has the second highest gain. When the homemade HEMT is used, the amplifier has a higher gain than the amplifier with the ATF HEMT. At the higher power consumption of the amplifier with the commercial HEMTs than 200 μW, the gain could not be determined

[4] We restricted the measurement up to $P \simeq 1$ mW to avoid the temperature rise of the 4 K stage.

due to the unstable characteristics. The amplifier with the homemade HEMT has stable gain at the higher power consumption than the amplifier with the commercial one. Thus, the amplifier with the homemade one can have higher gain than the amplifier with the commercial one.

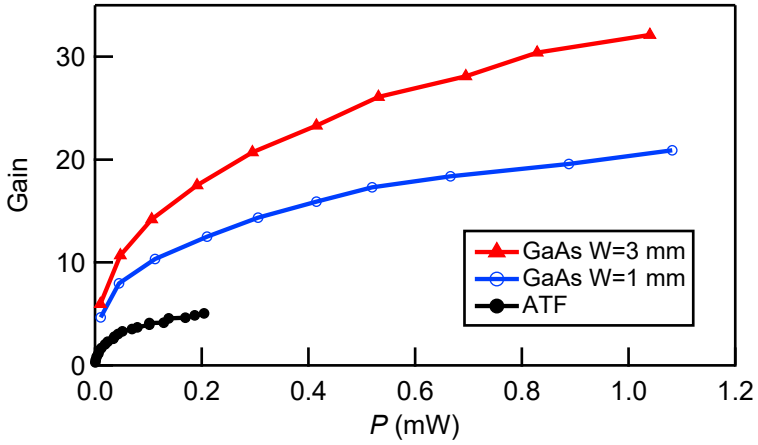

FIGURE 5.11: Gain $|A_{CS1}|$ of the three CS1 circuits plotted as a function of P.

Noise Characteristics

We measured the noise characteristics of the (3 mm; 4 μm) and (1 mm; 4 μm) HEMTs as well as the ATF HEMT in the CS1 circuit shown in Fig. 5.2 a) at 4.2 K. We chose $R_D = 500\ \Omega$, where $Z_{out} \simeq R_D = 500\ \Omega$. In this case, S^I_{ch} and S^V_{HEMT} can be evaluated as

$$S^I_{ch} = \frac{S^V_{out}}{|Z_{out}|^2} \simeq \frac{S^V_{out}}{R^2_D} \tag{5.13}$$

$$S^V_{HEMT} = \frac{S^V_{out}}{|A|^2}. \tag{5.14}$$

Before examining the noise characteristics, we measured the dc transport properties of the CS1 circuits to choose the operating point.

Figures 5.12 a) and 5.12 b) show the S^I_{ch} and S^V_{HEMT} spectra at the operating points estimated from the measured S^V_{out} spectra using Eqs. (5.13) and (5.14), respectively. In these plots, the RC damping at the output due to $Z_{out} \simeq R_D = 500\ \Omega$ and $C_{coax2} \simeq 75$ pF [see Fig. 5.3 a)] has been numerically compensated. Note that the data for the GaAs HEMTs were obtained at V_{DD} = 1 V, while those for the ATF were at 0.4 V. At low frequencies, where the $1/f$ noise governs the noise characteristics, S^I_{ch} of the GaAs HEMTs are much larger than that of the ATF HEMT, mainly because V_{DD} is larger in the former. Meanwhile, near the noise-measurement frequency of $f_o \simeq 1.8$ MHz (see Sec. 5.2.3), where the shot-noise contribution becomes dominant, S^I_{ch} of the three HEMTs are comparable with each other. The low-noise performance of the

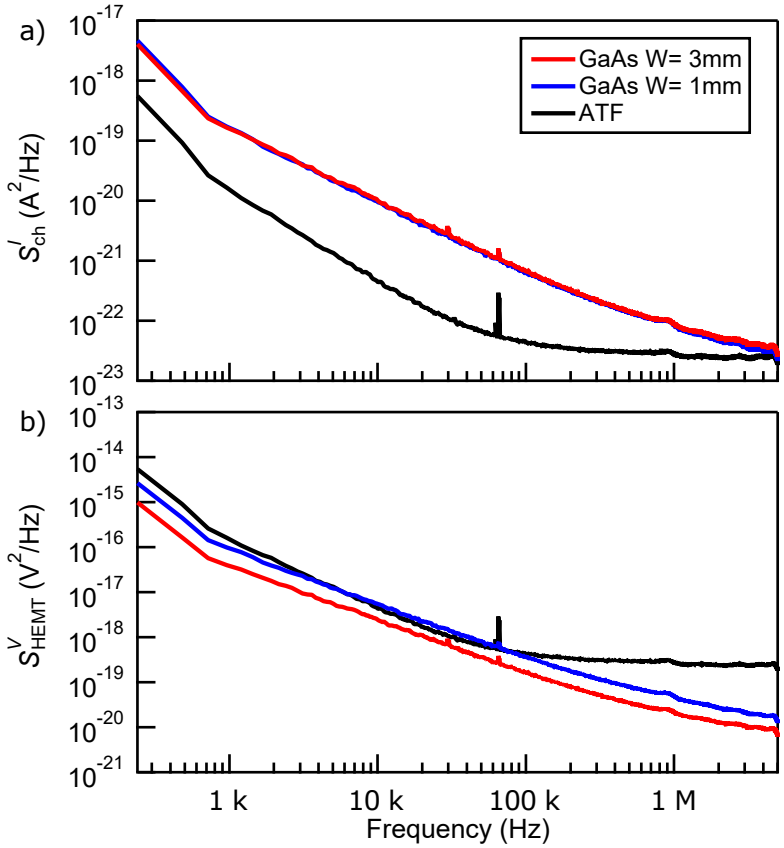

FIGURE 5.12: a) S^I_{HEMT} and b) S^V_{HEMT} of the three CS1 circuits.

GaAs HEMTs manifests itself in the S^V_{HEMT} spectra; the higher gains of the GaAs HEMTs result in the lower S^V_{HEMT} [see Figs. 5.10 and Eq. (5.14)]. Actually, S^V_{HEMT} of the (3 mm; 4 μm) HEMT circuit with the highest gain among the three is the lowest over the entire range of the frequency. We note that near $f_o \simeq 1.8$ MHz, it is about one order of magnitude lower than that of the ATF one [Fig. 5.12 b)].

The measured S^V_{HEMT} is summarized in Fig. 5.13, as a function of power consumption P. The (3 mm; 4 μm) HEMT shows the lowest S^V_{HEMT} over the entire range of P, and therefore it is the best suited for the present purpose [see Fig. 5.11].

Determination of R_{D}

Here, we discuss CS amplifiers based on the (3 mm; 4 μm) HEMT, which has the highest $|A|$ and the lowest S^V_{HEMT}. The load resistance R_{D} determines $|A|$, as seen in Eqs. (5.2) and (5.5). In Fig. 5.14, the red circles show the measured $|A|$ for several R_{D} values at $P \simeq 1$ mW at 4.2 K. The gain increases monotonically with R_{D}, following the curve simulated using Eq. (5.2) with $g_{\mathrm{m}} = 87$ mS and $g_{\mathrm{ds}} = 0.67$ mS. The tiny deviations of the experimental data from the simulation are due to the changes in g_{m} and g_{ds} caused by the shift of the operating point depending on R_{D}.

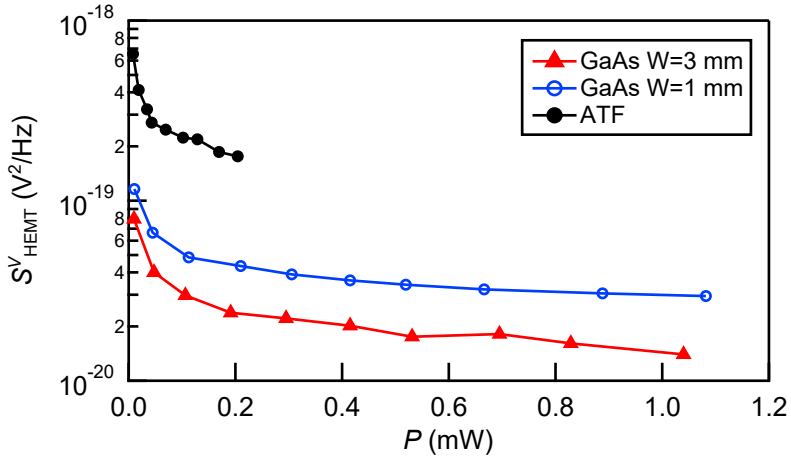

FIGURE 5.13: P dependence of S^V_{HEMT} at $f = 1.8$ MHz

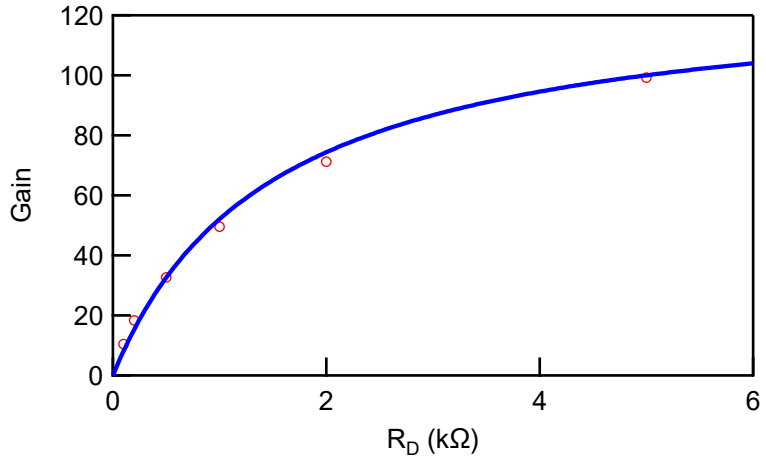

FIGURE 5.14: Gain $|A|$ as a function of R_{D} at $P \simeq 1$ mW. The blue line is a simulated curve using Eq. (5.2).

The black (red) trace in Fig. 5.15 a) shows the representative S^V_{HEMT} spectrum for $R_{\mathrm{D}} = 2$ kΩ with (without) the numerical compensation for the RC damping at the output of CS1. Figure 5.15 b) shows those for $R_{\mathrm{D}} = 200$ Ω. The effect of the RC damping in the $R_{\mathrm{D}} = 200$ Ω circuit is much smaller than that in the $R_{\mathrm{D}} = 2$ kΩ circuit, because Z_{out}, forming an RC filter with C_{coax2} [see Fig. 5.3 a)], monotonically decreases with R_{D}. Figure 5.15 b) indicates that below $R_{\mathrm{D}} = 200$ Ω, the damping effect can be neglected at the noise-measurement frequency of $f_1 \simeq 1.8$ MHz.

Figure 5.16 shows the R_{D} dependence of S^V_{HEMT} at 1.8 MHz. The S^V_{HEMT} value is minimal near $R_{\mathrm{D}} = 200$ Ω. Because of the negligible RC damping and the low S^V_{HEMT}, we chose $R_{\mathrm{D}} = 200$ Ω for our cryogenic amplifier [5].

[5] At higher R_{D} the operating point becomes close to the pinch-off, leading to lower g_{m}. This increases S^V_{HEMT} for a given S^I_{ch} because $S^V_{\mathrm{HEMT}} \simeq S^I_{\mathrm{ch}}/g^2_{\mathrm{m}}$

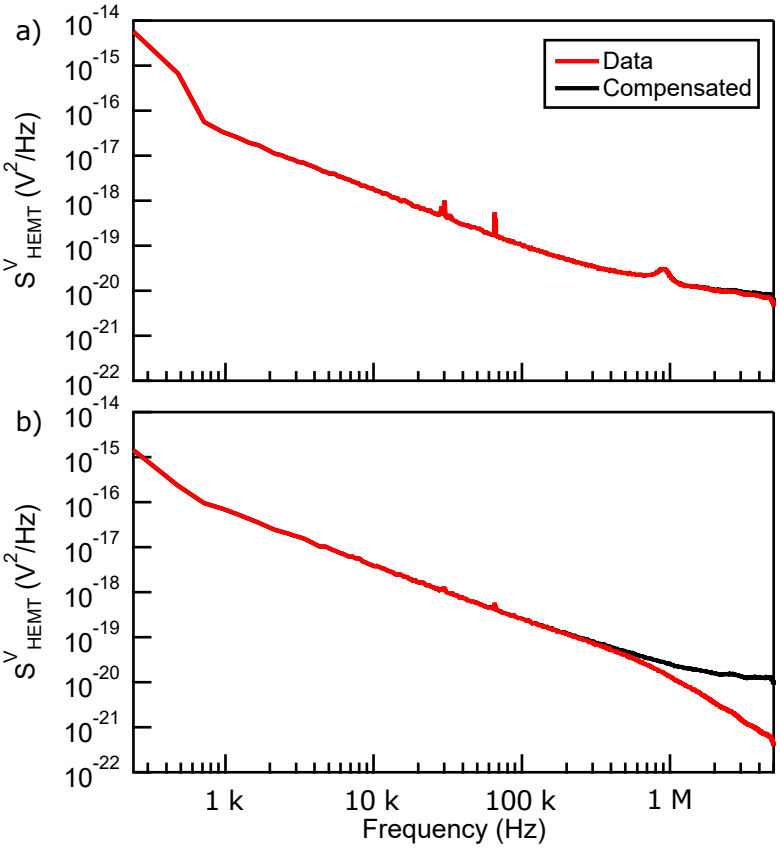

FIGURE 5.15: S^V_{HEMT} spectra of CS1 circuits with a) 200 Ω and b) $R_{\mathrm{D}} = 2\,\mathrm{k}\Omega$. The black (red) curves are with (without) compensation of RC damping.

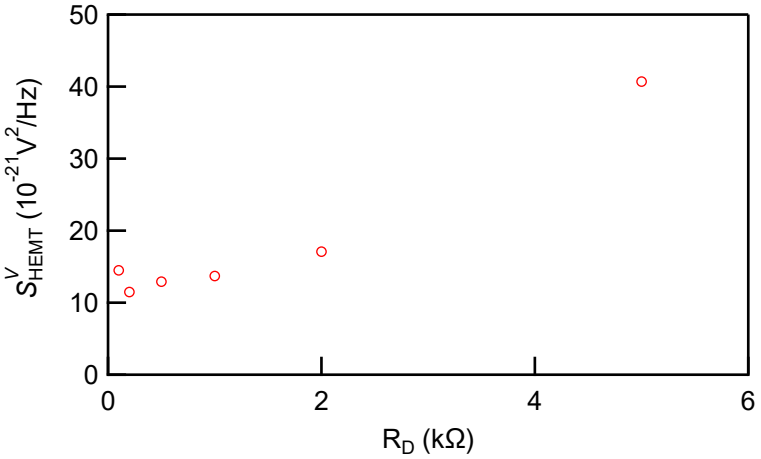

FIGURE 5.16: R_{D} dependence of S^V_{HEMT} at $f = 1.8$ MHz. The RC damping is numerically compensated. At higher R_{D} the operating point becomes close to the pinch-off, leading to lower g_{m}. This increases S^V_{HEMT} for a given S^I_{ch} because $S^V_{\mathrm{HEMT}} \simeq S^I_{\mathrm{ch}}/g^2_{\mathrm{m}}$.

Self-Biasing

Unlike the CS1 circuit, the cryogenic amplifier in Fig. 5.3 b) has the self-biasing resistor R_{S} and the shunt capacitor C_{S}. We examined the self-biasing

using another common-source circuit "CS2" shown in Fig. 5.2 b). At MHz frequencies, C_S= 100 nF dominates over R_S to ground the HEMT source, enabling us to obtain high ac gain $|A_{CS2}| = V_{out}/V_{ext}$ while simplifying the cryogenic assembly by removing the wiring for V_g [see Fig. 5.2 a)]. We chose R_S = 165 Ω and applied V_{DD} = 0.883 V to set the circuit near the operating point, where $P \simeq 1.3$ mW. Figure 5.17 a) shows an $|A_{CS2}|$ spectrum obtained by sweeping the frequency of the external ac voltage of $V_{ext} = 1$ mV RMS and measuring the ac output. Thanks to C_S, $|A_{CS2}|$ increases with frequency to saturate at $|A_{CS2}| \simeq 15.6$ above a few hundred kHz, which is comparable to the gain of the CS1 circuit $|A_{CS1}| \simeq 18$ (see Fig. 5.14). When the frequency is increased above 2 MHz, $|A_{CS2}|$ decreases because of the RC damping at the output of the amplifier.

Figure 5.17 b) shows that near 1.8 MHz, S^V_{HEMT} of CS2 ($\simeq 1.53 \times 10^{-20}$ A^2/Hz) is slightly larger than that of CS1, probably because of the misalignment of the operating point. However, it still remains much smaller than that of the ATF one [see Figs. 5.12 b) and 5.13].

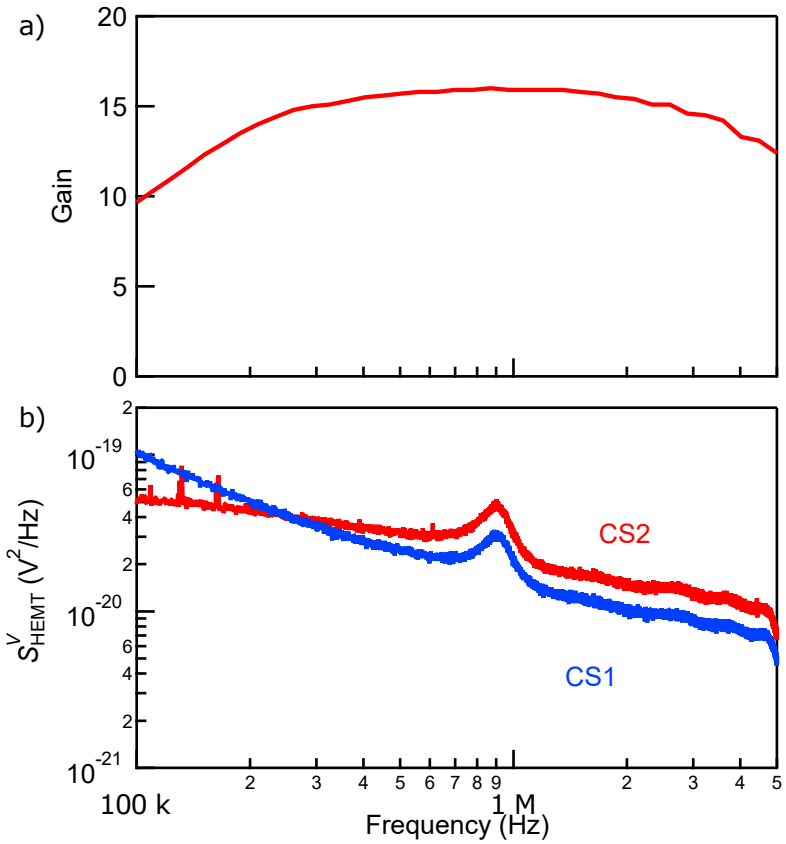

FIGURE 5.17: a) Measured $|A_{CS2}|$ spectrum. b) Comparison of S^V_{HEMT} between CS1 and CS2. The S^V_{HEMT} peak near $f = 900$ kHz is an artifact originating from the noise in the power supply.

5.3.3 Current Noise Measurement in Quantum Point Contact

Here, we demonstrate current-noise measurements performed on a QPC using the system shown in Fig. 5.3 a). The cryogenic amplifier with R_D= 200 Ω and R_S= 165 Ω was activated by applying V_{DD} = 0.883 V, the same as the CS2 circuit presented in Fig. 5.2. While the amplifier shows a slight change in its gain in different cooldowns, it can be used after appropriate calibration, as described in this section. The results are compared with those of the ATF-HEMT amplifier, which has the same R_D and R_S values and is activated by V_{DD} = 1.9 V. The measurements were performed at 30 mK and zero magnetic field.

Measurement Setup

Figure 5.18 shows a schematic of the measurement setup. The QPC, fabricated in a 2DEG with an electron density $n_e = 1.5 \times 10^{11}$ cm^{-2} and a mobility 6.6×10^5 cm^{2}V^{-1}s^{-1} in a GaAs/$Al_{0.33}Ga_{0.67}$As heterostructure, is formed by applying a gate bias V_{SG}. We measured the dc transport properties using a standard lock-in technique by applying an ac modulation of V_{bias}= 10 μV RMS (33 Hz) and measuring the current I_m.

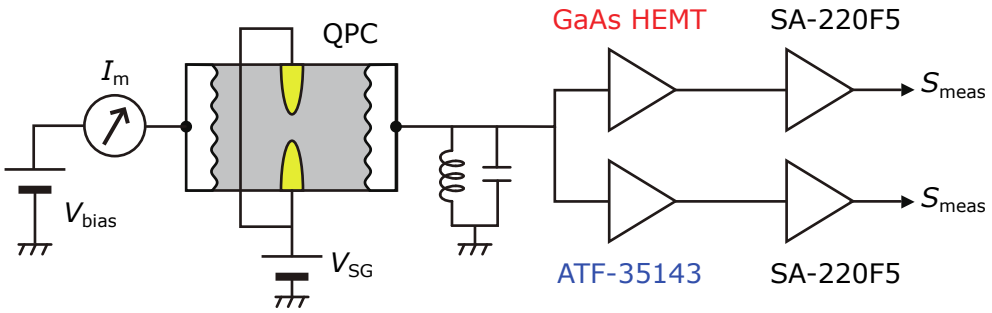

FIGURE 5.18: Schematic of noise-measurement setup for a QPC.

The current noise was measured through the two measurement lines connected to a single output of the QPC: one comprising the GaAs-HEMT amplifier "GaAs line" and the other the ATF-HEMT amplifier "ATF line". We measured time-domain ΔV_{meas} data for $\tau_{int} = 50$ seconds at a sampling rate of 10 MS/s and evaluated S_{meas} spectra near 1.8 MHz. Figure 5.19 a) shows representative results obtained at $V_{SG} = -0.88$ V, where the QPC resistance is $R_m = 21.5$ kΩ. The resonance-peak height at $f_o = 1.794$ MHz of the GaAs line is much higher than that of the ATF line, while the background of the former is lower than the latter. This observation suggests that the GaAs line has a better resolution than the ATF line.

The resonance line shapes are slightly distorted from the Lorentzian line shapes expected for an ideal RLC resonance circuit. This distortion is due to the parasitic resistance r in the RLC tank circuit and the parasitic capacitances in the HEMT.

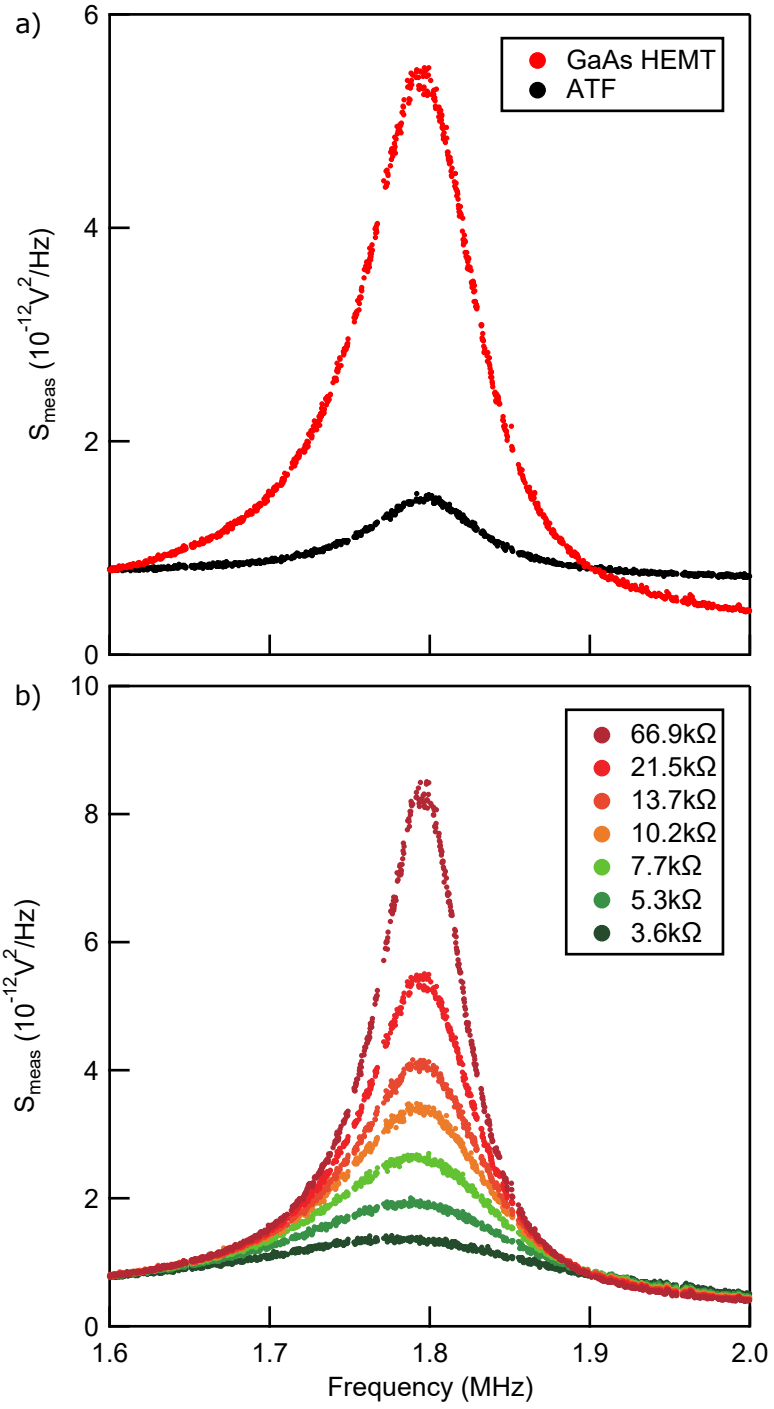

FIGURE 5.19: a) Representative noise spectra measured through the GaAs line and the ATF line. b) Zero-bias noise spectra measured through the GaAs line at several R_m values: R_m = 66.9 kΩ (dark red), 21.5 kΩ (red), 13.7 kΩ (dark orange), 10.2 kΩ (orange), 7.7 kΩ (light green), 5.3 kΩ (green), and 3.6 kΩ (dark green).

Calibration

At $V_{\rm bias}$= 0 V, the Johnson noise dominates over the other noises in the QPC, leading to $S^I_{\rm in} \simeq 4k_{\rm B}T_{\rm e}{\rm Re}(Y_1)$, where ${\rm Re}(Y_1)$ is the real part of the admittance $Y_1 = Z_1^{-1}$ [96]. Here, we calibrate the measurement system from the resonance peak height of the Johnson-noise spectra. The $S^V_{\rm meas}$ peak height is described as

$$S^V_{\rm meas} = A^2_{\rm RT}\left|A(f_o)\right|^2\left[\left|Z_1^2\right|\left(S^I_{\rm in}+S^I_{\rm HEMT}\right)+S^V_{\rm HEMT}\right], \qquad (5.15)$$

where $A_{\rm RT}$ (= 400) is the gain of the room-temperature amplifier [SA-220F5 in Fig. 5.3 a)] and $|A(f_o)|$ is that of the cryogenic amplifier at $f = f_o$ [see Eq. (4.3)]. With increasing $R_{\rm m}$, $|Z_1|$ and hence the peak height monotonically increases, as shown in Fig. 5.19 b). The open (filled) circles in Fig. 5.20 summarizes the $R_{\rm m}$ dependence of the $S^V_{\rm meas}$ peak value estimated at 30 kHz bandwidths near $f = f_o$ measured through the GaAs (ATF) line, and the blue solid (black dashed) curve is the simulation using Eq. (5.15). Table 5.1 summarizes the parameters used for the simulations, $|A(f_o)|$, T_e, $S^I_{\rm HEMT}$, and $S^V_{\rm HEMT}$ [6]. Here, we note two important findings that justify the simulations. First, the data for both GaAs and ATF lines agree well with the calculated curves using the same T_e and $S^I_{\rm HEMT}$ values over the three orders of $R_{\rm m}$. Second, $|A(f_o)|$ and $S^V_{\rm HEMT}$ of both amplifiers are comparable to the results obtained in Sec. 5.3.2.

	$\lvert A\,(f_o)\rvert$	T_e	$S^I_{\rm HEMT}$	$S^V_{\rm HEMT}$
GaAs	14.9	80 mK	2.64	0.96
ATF	5.35	80 mK	2.64	17.8

TABLE 5.1: Parameters of the fit curves in Fig. 5.20. The units of $S^I_{\rm HEMT}$ and $S^V_{\rm HEMT}$ are 10^{-27} A^2/Hz and 10^{-20} V^2/Hz , respectively.

Shot-noise Measurement

We measured the $V_{\rm bias}$ dependence of $S_{\rm meas}$ from the GaAs line and evaluated $S^I_{\rm in}$ using the parameters shown in Table 5.1. Figure 5.21 a) shows the linear conductance G of the QPC in a unit of $G_0 = 2e^2/h$ as a function of $V_{\rm SG}$ [ohmic contact resistance ($\simeq$ 2 kΩ) is subtracted]. The current-noise measurements were performed at G/G_0= 1.5, 1, 0.65, and 0, indicated by the markers superimposed on the trace. Figure 5.21 b) shows the $V_{\rm bias}$ dependence of the bias-induced excess noise $S^I_{\rm bias} = S^I_{\rm in}\left(V_{\rm bias}\right) - S^I_{\rm in}(0)$. We observed the increase in

[6] In this simulation, we first examined fits to the data for the GaAs line with several sets of $|A(f_o)|$ and T_e values to obtain r, $S^I_{\rm HEMT}$, and $S^V_{\rm HEMT}$ as fit parameters, while $C_{\rm in} = 238$ pF and $L_{\rm in} = 33\ \mu$H are fixed to give $f_o = 1.794$ MHz. Then, we examined fits to the data for the ATF line with the fixed values of T_e, r, and $S^I_{\rm HEMT}$ obtained from the former fit. Using this procedure, we found that only the parameters presented in Tab. 5.1 and $r = 14.7\ \Omega$ explain our experimental data consistently within the error of approximately 4 %.

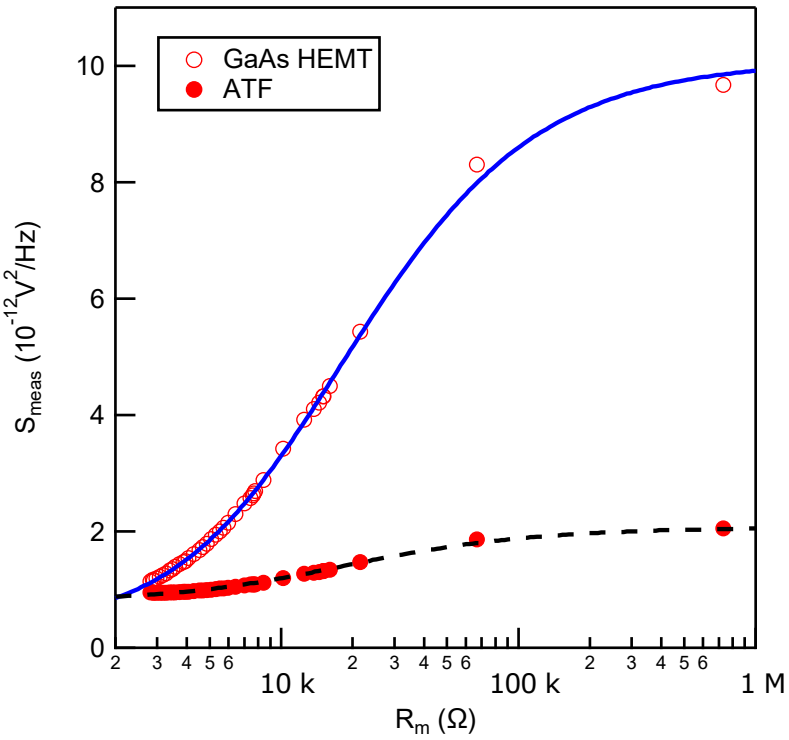

FIGURE 5.20: R_m dependence of peak heights for the GaAs line (open circles) and ATF line (filled circles). The blue solid and black dashed lines show fitted curves.

$S^I_{\rm bias}$ with $|V_{\rm bias}|$ at G/G_0= 1.5 (filled circles) and 0.65 (filled squares), while it remains zero independent of $|V_{\rm bias}|$ at G/G_0= 1 (open diamonds) and 0 (open triangles), being consistent with theory [3] and the previous experiments [97, 102, 103, 105, 106, 109, 124]. We compared the $S^I_{\rm bias}$ data at G/G_0= 1.5 and 0.65 with theoretical shot noise:

$$S_{\rm shot} = 2e\frac{V_{\rm bias}}{R_{\rm m}}F\left[\coth\left(\frac{eV_{\rm bias}}{2k_{\rm B}T_e}\right) - \frac{2k_{\rm B}T_e}{eV_{\rm bias}}\right], \tag{5.16}$$

where $F = \sum_{n,\sigma}\left[\mathcal{T}_{n,\sigma}(1-\mathcal{T}_{n,\sigma})\right] / \sum_{n,\sigma}\mathcal{T}_{n,\sigma}$ is the Fano factor. Here, $\mathcal{T}_{n,\sigma}$ is the transmission probability of spin σ =↑ or ↓ electrons in the n-th subband in the QPC; in the present spin-degenerate case, we can assume $\mathcal{T}_{n,\uparrow} = \mathcal{T}_{n,\downarrow}$. The theoretical curve calculated by substituting $\mathcal{T}_{1,\sigma} = 1$ and $\mathcal{T}_{2,\sigma} = 0.5$ ($\mathcal{T}_{1,\sigma}$ = 0.65 and $\mathcal{T}_{2,\sigma} = 0$) to Eq. (5.16), shown in blue in the figure, agrees well with the experimental result at G/G_0 = 1.5 (0.65) [7].

5.3.4 Resolution of the Noise Measurement

The resolution of the current-noise measurement is evaluated as the standard deviation of measured $S^I_{\rm in}$ [12]. We repeated the $S_{\rm meas}$ measurement about two-hundred times on the QPC set at the first conductance plateau ($R_{\rm m} \simeq 16$

[7] The slight difference between the experimental data and the theoretical curve at G/G_0 = 0.65 might be caused by the nonlinear bias dependence of the QPC conductance.

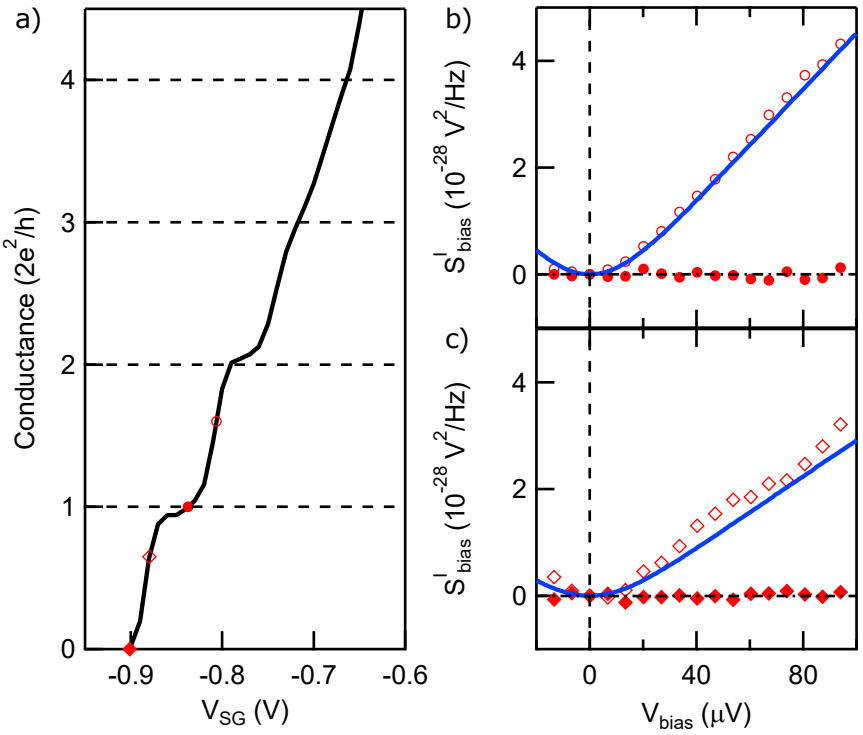

FIGURE 5.21: a) Conductance behavior of the QPC as a function of V_{SG}. (b) V_{bias} dependence of S^I_{bias} measured at $G/G_0 = 1.5$ (filled circles), 1 (open diamonds), 0.65 (filled squares), and 0 (open triangles). The blue solid curves are simulations using Eq. (5.16).

kΩ, including the Ohmic contact resistance) at V_{bias}= 0 V and estimated S^I_{in} at $f = f_o$ for these measurements. The upper panel in Fig. 5.22 a) [5.22 b)] shows the deviation $\Delta S^I_{in} = S^I_{in} - \langle S^I_{in} \rangle$, where $\langle S^I_{in} \rangle$ is the average of the S^I_{in} values, measured from the GaAs (ATF) lines. The lower panel is the result of the histogram analysis. The Gaussian fit for the histogram data shows that the standard deviation σ_{GaAs} (σ_{ATF}) of the GaAs (ATF) line is 0.52×10^{-29} A^2/Hz (0.83×10^{-29} A^2/Hz). From the comparison between them, we found that the GaAs-HEMT amplifier has about 1.6 times better resolution than the ATF-HEMT amplifier. Notably, in the present experimental setup shown in Fig. 5.18, the GaAs and ATF lines share S^I_{HEMT} so that the lower σ_{GaAs} is only due to the lower S^V_{HEMT} of the GaAs line. If the ATF line is removed to reduce S^I_{HEMT}, the GaAs line may show even better resolution than the present result.

It is instructive to compare our results with those in the previous study. Reference [12] reports $\delta S^I_{in} = 2.8 \times 10^{-29}$ A^2/Hz with $\tau_{int} = 10$ seconds for a cross-correlation measurement using ATF-HEMT amplifiers. If we perform a similar measurement using our GaAs-HEMT amplifiers, the standard deviation, or the resolution is expected to be $\delta S^I_{in} = 0.82 \times 10^{-29}$ A^2/Hz: the shorter τ_{int} increases δS^I_{in} by a factor of $\sqrt{5}$, while the cross-correlation technique decreases it by $\sqrt{2}$. Thus, the resolution of our setup is below one-third of that reported in Ref. [12]. If we define the measurement efficiency by the

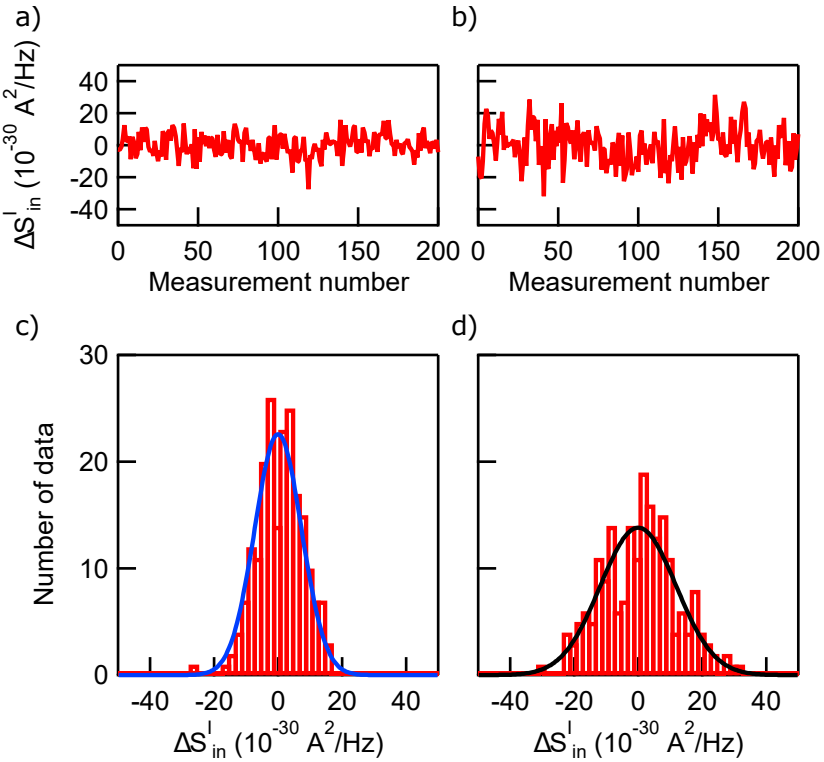

FIGURE 5.22: a) and b) (Upper panels) $\Delta S^I_{\rm in}$ data for the same measurements repeated 205 times ($R_{\rm m} \simeq 15$ kΩ; $\tau_{\rm int} = 50$ seconds). (Lower panels) Histogram analysis. Solid lines show Gaussian fits. a) GaAs HEMT line shows $\sigma_{\rm GaAs} = 0.52 \times 10^{-29}{\rm A}^2/{\rm Hz}$, while b) ATF HEMT shows $\sigma_{\rm ATF} = 0.83 \times 10^{-29}{\rm A}^2/{\rm Hz}$.

inverse of $\tau_{\rm int}$, which is the data integration time required to reach a certain value of $\delta S^I_{\rm in}$, the efficiency of our system is more than $(1/3)^{-2} = 9$ times as high efficiency as the previous one.

5.3.5 Current Noise Measurement in Quantum Hall Regime

We also tested current-noise measurements to show that our homemade amplifier can amplify the current noise signal for higher power consumption, $P \simeq 10$ mW. Here, we use the (1 mm; 4 μm) HEMT. The QPC device for another experiment was used to test the cryogenic amplifier with the homemade HEMT. The details of the noise measurement are given below.

Measurement Setup

The QPC is defined on the surface of a GaAs/$Al_{0.33}Ga_{0.67}$As heterostructure grown by MBE. The 2DEG has a density of $1.5 \times 10^{11}{\rm cm}^{-2}$ and mobility of 6.6×10^5 cm^2/V s.

Figure 5.23 shows a schematic diagram of the QPC device placed in the MC and the noise measurement circuit. The QPC is defined by the two metallic gate electrodes, where the same gate voltage, $V_{\rm SD}^{\rm QPC}$, is applied. In this

measurement, the QPC is set in the quantum Hall regime, the bulk filling factor is set to be $\nu_{\text{bulk}} = 4$ by adjusting the back gate voltage, -0.3 V, applying the magnetic field, -1.3 T, perpendicularly to the 2DEG. An additional gate electrode is prepared on the 2DEG (see the right-bottom corner of the 2DEG in Fig. 5.23 a). V_g^{DP} is applied to this electrode to control the conductance of the edge transport, which goes to the noise measurement part through the Ohmic contact Ω_{AMP}.

The conductance of the QPC is measured using the operational amplifier, Op-amp, circuit placed in the room temperature. This circuit is connected to one of the two Ohmic contacts ($\Omega_{\text{Calib.}}$ or Ω_{Shot}) according to the purpose of the measurement.

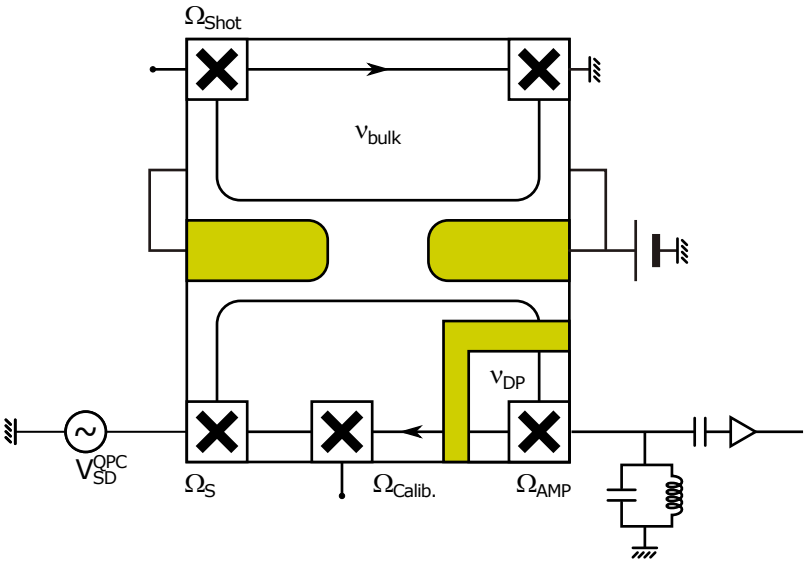

FIGURE 5.23: Schematic diagram of the QPC device. The device has five Ohmic contacts. The noise is measured at Ω_{AMP} and the current is measured at Ω_{shot} or Ω_{Calib} using Op-amp, as shown in the inset.

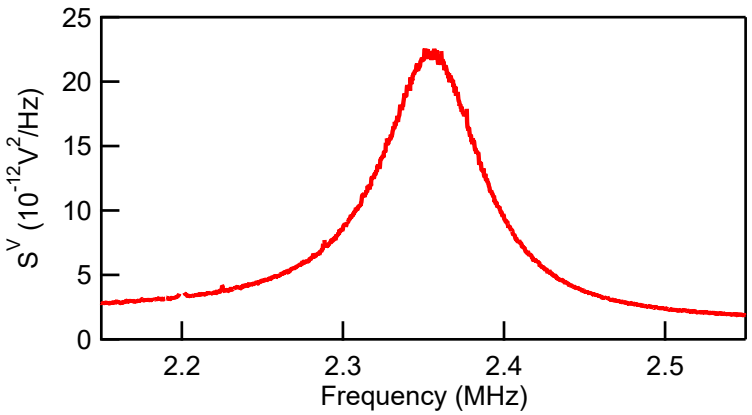

FIGURE 5.24: Noise power spectrum at $\nu_{\text{DP}} = 1$. The averaged frequency regime is shown in the inset.

Figure 5.24 shows an example of the measured noise power spectrum of the QPC at $\nu_{\mathrm{DP}} = 1$. $S^{\mathrm{V}}_{\mathrm{out}}(f)$ is measured 10,000 times averaged data for $\tau_{\mathrm{int}} = 55$ s. The height of the peak is fitted by Eq. (5.15).

Calibration

Figure 5.25 a) shows a schematic circuit diagram for the noise calibration. First, $V_{\mathrm{g}}^{\mathrm{QPC}} = -3.3$ V is applied to pinch off the QPC, and the QPC conductance is measured through the contact $\Omega_{\mathrm{Calib.}}$. Simultaneously, the noise power at $V_{\mathrm{SD}}^{\mathrm{QPC}} = 0$ is measured for ν_{DP} =1, 2, 3, and 4 by adjusting $V_{\mathrm{g}}^{\mathrm{DP}}$. We measured the thermal noise by adjusting the $V_{\mathrm{g}}^{\mathrm{DP}}$ to vary the ν_{DP}.

Figure 5.25 b) shows the conductance calculated by subtracting output-current at Ω_{Calib} from input-current by $\widetilde{V}_{\mathrm{SD}}^{\mathrm{QPC}}$ at Ω_{S}. We measured the noise at the quantum Hall regime because the edge states on the quantum Hall regime is a stable state, and the corresponding noise power density is well known. The device has well-quantized conductance as $V_{\mathrm{g}}^{\mathrm{DP}}$. The noise measurement is conducted for various $V_{\mathrm{g}}^{\mathrm{DP}}$ settings at five temperatures (25, 65, 88, 150, and 185 mK).

The noise for calibration is measured at 10 mW of the power consumption of the amplifier. The parameters are extracted assuming $S^{\mathrm{I}}_{\mathrm{in}} = 4k_{\mathrm{B}}T_e G$ in Eq. (5.15), where k_{B} is the Boltzmann constant and T_e is the electron temperature, which is assumed to equal the temperature for the moment.

Figure 5.25 c) shows calibration results for various $R^{\mathrm{DP}}(= G^{-1})$, which is the resistance between Ω_{AMP} and the device, at $T = 25$ mK. The solid curve represents the result of the numerical fitting based on Eq. (5.15). The curve fitting parameter originates from the combined resistance in the LC circuit and R^{DP}.

Figure 5.25 d) shows $S^{\mathrm{V}}_{\mathrm{out}}$ as a function of T_e, and the result of the linear fitting. The observed linearity between 25 mK and 200 mK supports the above assumption that the electron temperature equals the fridge temperature. From these results, $A = 14$ at 10 mW is extracted. Note that A is smaller than the $R_{\mathrm{D}} \times g_{\mathrm{m}} = 32$, as we reported already.

Shot Noise Measurement

After calibrating the thermal noise of the measurement setup, we performed the shot (partition) noise measurement. Figure 5.26 a) shows a schematic circuit diagram for partition noise measurement at the QPC. The conductance is measured through the contact Ω_{Shot}. To measure the shot noise, the $V_{\mathrm{g}}^{\mathrm{DP}}$ is fully opened. Based on the calibration, $S^{\mathrm{I}}_{\mathrm{in}}$ is extracted as follows: $S^{\mathrm{V}}_{\mathrm{out}}$ and G are measured at a fixed $V_{\mathrm{g}}^{\mathrm{QPC}}$ as a function of $V_{\mathrm{SD}}^{\mathrm{QPC}}$ between -60 μV and $+60$ μV.

Figure 5.26 b) shows the zero-bias conductance as a function of $V_{\mathrm{g}}^{\mathrm{QPC}}$. Unfortunately, the extra energy level in the quantum Hall effect does not appear because the width between QPC gate electrodes is not well designed. The partition noise at the condition indicated by the circle mark, about $1 \times e^2/h$

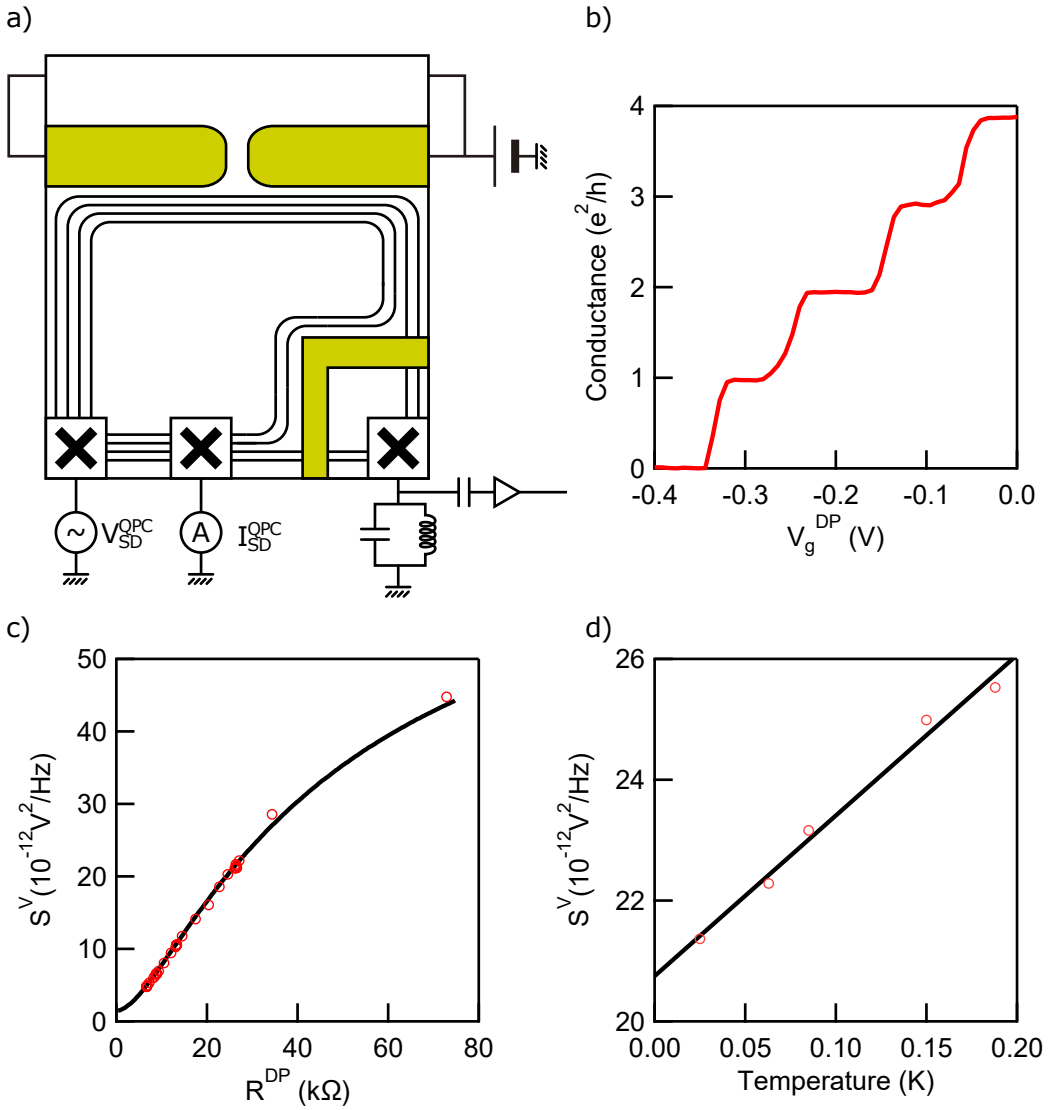

FIGURE 5.25: Schematic diagram of the noise-measurement system for calibration and partition noise measurement. a) Conductance of the device as a function of V_g^{DP}. b) Schematic diagram of the noise-measurement system for calibration. c) and d) Calibration by noise thermometry of T. c) S_V^{out} as a function of R^{DP} at temperature. Solid line is a noise model fit described in Eq. (5.15). d) S_V^{out} as a function of T. Solid line is a linear fit of S_V^{out} at five different temperatures between 25 mK and 200 mK.

of conductance, is shown in Fig. 5.26 c). The black line is the theoretical fitting line based on Eq. (5.16). Here, T_e is 25 mK. It is consistent with scattering theory and with recent measurements on mesoscopic tunnel barriers free of impurities.

5.4 Summary

We have presented a noise-measurement system comprising a homemade cryogenic GaAs-HEMT amplifier. Our system was precisely calibrated by

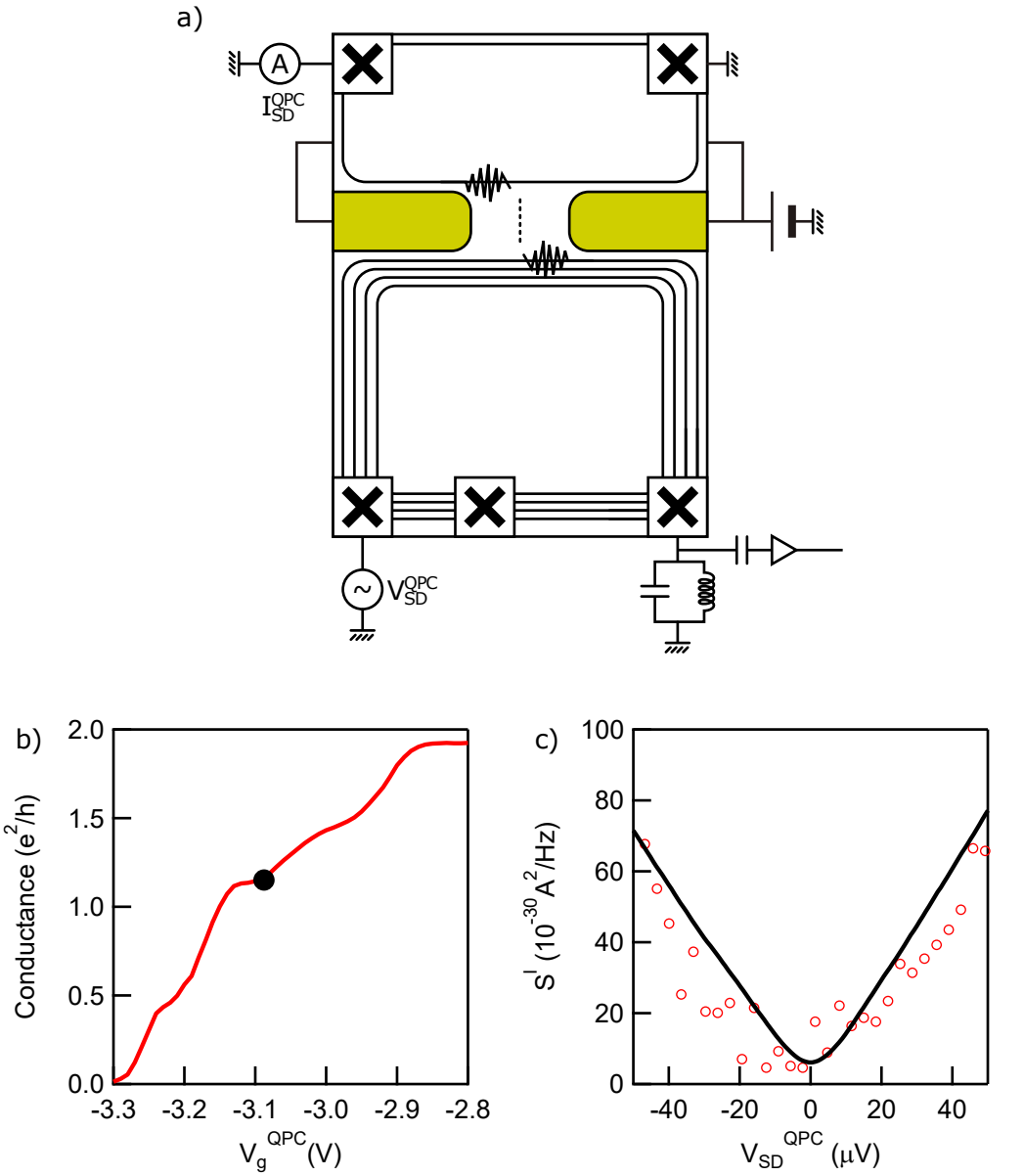

FIGURE 5.26: a) Schematic diagram of the noise-measurement system for calibration and partition noise measurement. b) Linear conductance $g\left(V_{SD}^{QPC}=0\right)$ as a function of V_g. A black dot indicates V_g^{QPC} settings for the noise measurements shown in (c). c) QPC partition noise, S_I^{QPC}, as a function of V_{SD}^{QPC}, for conductance near $1\times e^2/h$. A solid line is theoretical line of partition noise.

Johnson-noise thermometry. We measured the shot noise of the QPC and quantum Hall regimes to compare the performance of the system. The system has a higher resolution than that comprising a commercial-HEMT amplifier, mainly due to the high g_m of the homemade HEMT. We achieved a system with efficiency being more than nine times better than in previous research [12].

The measurement system is as significant as investigating the physical

meaning in the sample. A high-resolution measurement system would be performed to measure novel mesoscopic phenomena. We believe that the achievement described here is important as the basement for the new experimental physics.

Chapter 6

Current Noise in Quantum Hall Effect Breakdown of Graphene

6.1 Background and Purpose

In 1980, Klaus von Klitzing measured the characterization of the electronic transport of a silicon-based field-effect transistor [Fig. 6.1 a)] at the High Magnetic Field Laboratory in Grenoble. On February 5th, 1980, he discovered unexpected phenomena, now called the quantum Hall effect [1]. He awarded the Nobel prize due to the observation of the plateau of the Hall voltage [Fig. 6.1 b)]. The quantum Hall effect is a significant phenomenon not only as a testbed of the mesoscopic system but also as a new International System of Units (SI). Thanks to his achievements, we can now calibrate the resistance combined with Planck constant h and the elementary charge e, $h/e^2 \simeq 25.813\ \mathrm{k}\Omega$ [47, 48].

The high bias voltage or bias current is necessary to obtain a high resolution of the resistance standard. The quantized resistance varies when the bias voltage (bias current) exceeds the critical electric field, E_c (I_c), as shown in Fig. 6.2 [43]. The phenomenon is called the quantum Hall effect breakdown (QHEBD). It is significant to investigate the non-equilibrium state of the quantum Hall effect regime to realize quantum information devices or obtain the high-resolution resistance standard.

There are two types of models to explain the QHEBD. The bootstrap electron heating (BSEH) model, proposed by Susumu Komiyama and Yasushi Kawaguchi, explains the collision of accelerated carriers with bound electrons [59]. In this model, the system fluctuates thermally because of the scattering between electrons and lattices. The quasi-elastic inter-Landau level scattering (QUILLS) explains that the excitation carriers exceed the Landau level [49–51]. Despite these theories, complete understanding of QHEBD has not been met. In this Chapter, we try to clarify the dominant mechanisms of the QHEBD using conductance measurement and current noise measurement.

Considerable interest has focused on current noise measurements, which allow electron conduction in the QHEBD state to be investigated in more detail [72–74, 130, 131]. For the QHEBD in GaAs/AlGaAs, the precursor phenomenon at the Hall bar structure [72] and the giant Fano factor are observed in the Corbino disk [73, 74].

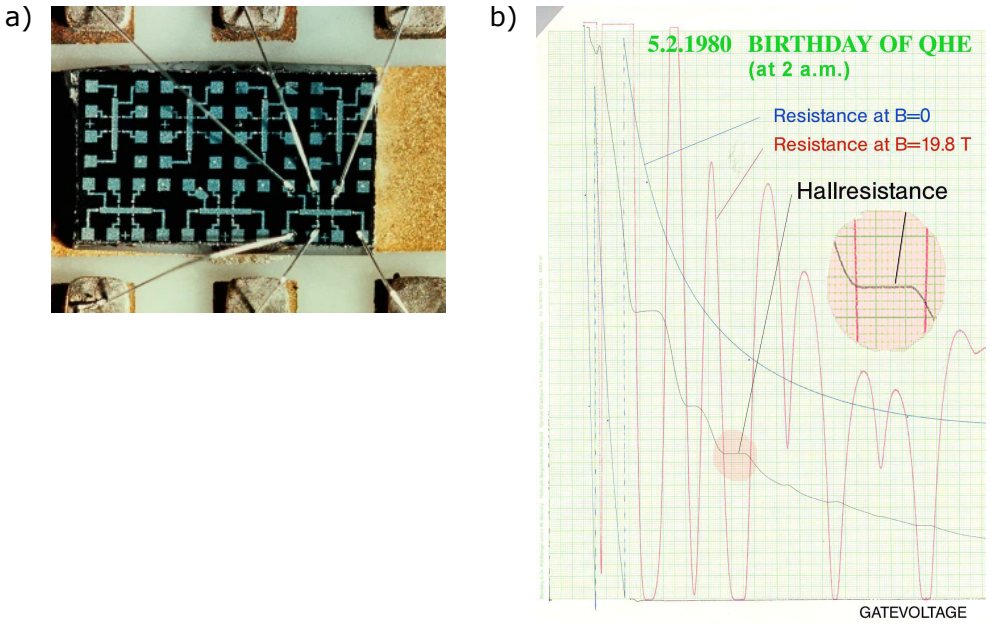

FIGURE 6.1: a) Typical silicon MOSFET device that Klaus von Klitzing measured. Reprinted by permission from Springer Nature: Springer Nature Nature Physics [48], 2021. b) Hall resistance and longitudinal resistance of a silicon MOSFET at liquid helium temperature as a function of the gate voltage. Reprinted by permission from Springer Nature: Springer Nature 25 Years of Quantum Hall Effect (QHE) A Personal View on the Discovery, Physics and Applications of this Quantum Effect by Klaus von Klitzing 2021.

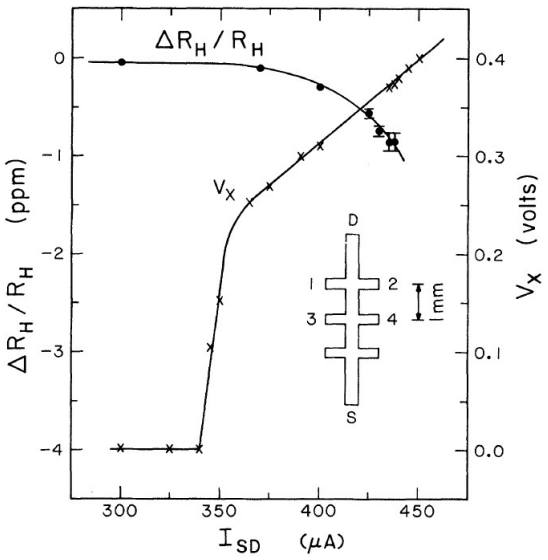

FIGURE 6.2: Resistance as a function of current. Reprinted figure with permission from [43] Copyright 2021 by the American Physical Society. The Hall voltage increases from 350 μA.

We studied the QHEBD using graphene as a testbed, not using GaAs/AlGaAs heterostructure. Since graphene can adjust the carrier type and carrier density, it is a more potential material than the GaAs/AlGaAs heterostructure. It is also known that graphene has a higher I_c due to the large value of the cyclotron energy [132], thus graphene would be more suitable as the resistance standard. Given the unique band structure of graphene and its symmetry, there is no obvious prediction for the QHEBD behavior, and detailed experimental investigations are necessary. There has been much experimental [69, 132–139] and theoretical [140] interest in QHEBD studies of graphene. Only a few experimental studies for current noise exist [141, 142]. Laitinen *et al.* research a monolayer Corbino disk-shape graphene [141]. They measured the low-frequency current noise (frequency $f \leq 10$ Hz) and shot noise experiments ($f = 600$-900 MHz). Their results indicate intense low-frequency noise in the rapidly growing, at steep sections of the I-V curves, which they interpret as bunching of electrons in the avalanche generation of the BSEH regime. On the other hand, the noise is close to the regular shot noise at microwave frequencies, although they have found $0 < F < 1.5$. The Fano factor at microwave frequencies measured at the end of the avalanche regime seems independent of the magnetic field, as shown in Fig. 6.3 a).

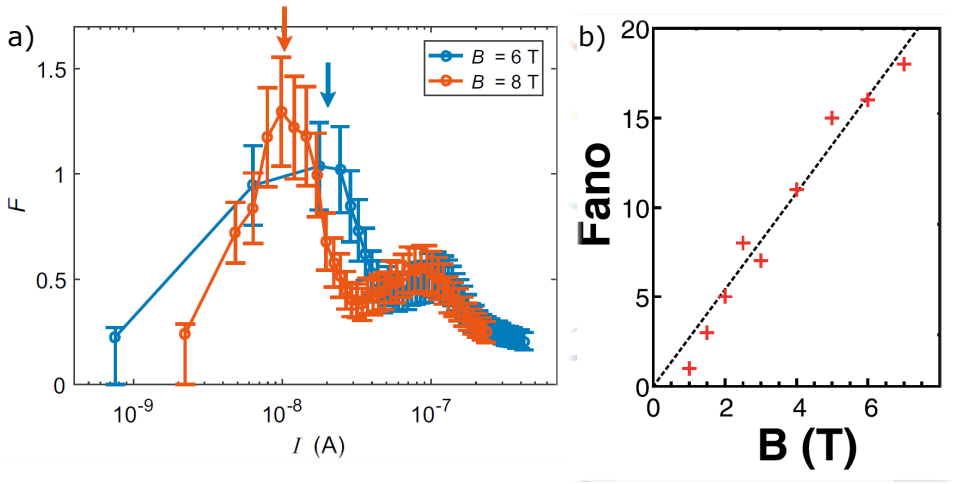

FIGURE 6.3: a) Fano factor as a function of bias current on a monolayer Corbino disk-shape graphene at 6 and 8 T. The Fano factor is under 1.5. Reprinted by permission from Springer Nature: Springer Nature Journal of Low Temperature Physics [141], 2021. b) Fano factor as a function of a magnetic field on a bi-layer Hall bar shaped graphene The Fano factor is linearly dependent on the magnetic field. Reprinted figure with permission from [142] Copyright 2021 by the American Physical Society.

Yang *et al.* [142] researched a bi-layer graphene Hall bar. They measure the shot noise experiments in the 4.5-5.5 GHz band. Their results show that the Fano factor $F \leq 20$ is linearly dependent on the magnetic field as shown in Fig. 6.3 b).

We measured the current noise experiments at about 2.75 MHz with the monolayer Hall bar varying the carrier type, p-type and n-type. We compared the QHEBD phenomenon between the GaAs/AlGaAs and monolayer graphene.

6.2 Sample Fabrication

We fabricated the sample at Quantum Nano-electronics Lab in POSTECH, Republic of Korea. Takashi Taniguchi and Kenji Watanabe produced graphene and hBN flakes from the National Institute for Materials Science (NIMS) in Japan. Here, we introduce how to fabricate hBN/graphene/hBN stacking.

6.2.1 Exfoliating 2D Crystals

We prepared graphene and hBN films by mechanical exfoliation of graphite or hBN flakes, as shown in Fig. 6.4 [143, 144].

1. Adhesive tape is pressed against a 2D crystal so that the top few layers are attached to the tape and is peeled away with graphite or hBN layer sticking on it.

2. The newly made surface is again pressed along the new adhesive.

3. Si/SiO_2 substrate is softly pressed against the taped to get the graphite layers. The graphene lies on the substrate because of the van der Waals force between the graphene and substrate.

Thick hBN flakes are necessary for encapsulating graphene to prevent environmental effects.

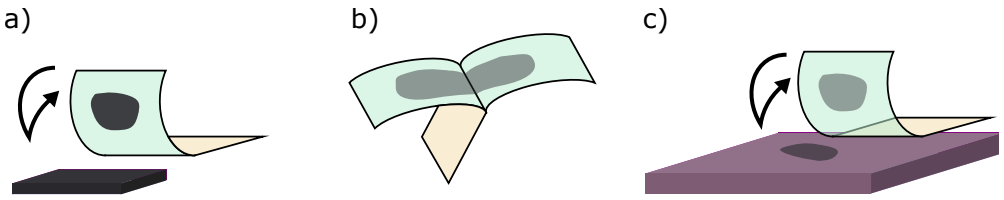

FIGURE 6.4: Schematic diagram describing steps of the mechanical exfoliation of graphene from a graphite using commercial adhesive tape. a) Adhesive tape is pressed to graphite for exfoliation. b) Both sides of the graphene are exfoliated with adhesion of the tape. c) Graphene is pressed on the Si/SiO_2 substrate, and peeled off by the tape. The graphene sticks on the substrate due to the van der Waals force between graphene and the substrate [143, 144].

6.2.2 Stacking hBN/Graphene/hBN

We used the polymer droplets, Elvacite 2552C (Lucite International), to transfer the hBN and graphene, and encapsulate [145]. Because the Elvacite is the white polymer powder, the Elvacite has to be dissolved in anisole with a ratio by volume of 1 : 1. We placed a small droplet of the Elvacite/anisole solution on the optical microscope slide using a metal tip. We baked the optical microscope slide slowly using a hotplate up to 180 °C for five minutes to evaporate the anisole solvent. The details are as follows (see Fig. 6.5).

1. Adhesive Elvatcite stamp pressed onto the hBN flake heated to 70 $\sim$ 80 °C.
2. Aligned hBN stamp pressed the graphene. Then the graphene would be picked up by van der Waals forces acting between 2D crystals.
3. Top hBN/graphene stamp picked up the bottom hBN by pressing the bottom hBN.
4. After finishing the vdW heterostructure assembly, the final transfer was conducted on the SiO_2/Si substrate heated to 180 °C to melt the stamp.
5. The stamp residue was removed by acetone rinse.
6. The sample was annealed in the vacuum at 500 °C for one hour to evaporate the residue and remove bubbles between layers, as shown in Fig. 6.6.

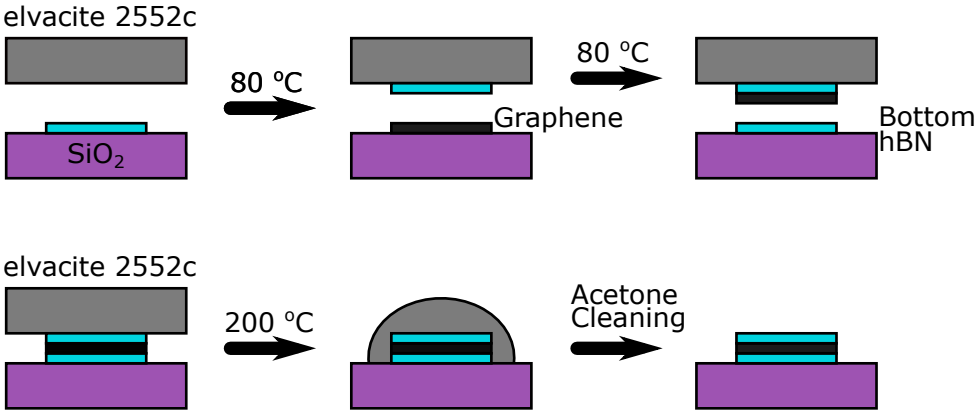

FIGURE 6.5: Schematic illustration of encapsulating graphene using the Elvacite as an adhesion layer. a) Elvacite stamp, which has adhesive properties at 70 $\sim$ 80 °C, picks up the flakes. b) hBN picks up the graphene by van der Waals force. c) Bottom hBN is picked up, in the same way, explained in b). d) Stack is placed with melted Elvacite on the SiO_2/Si substrate heated to 180 °C. e) Stamp residue is removed by acetone rinse.

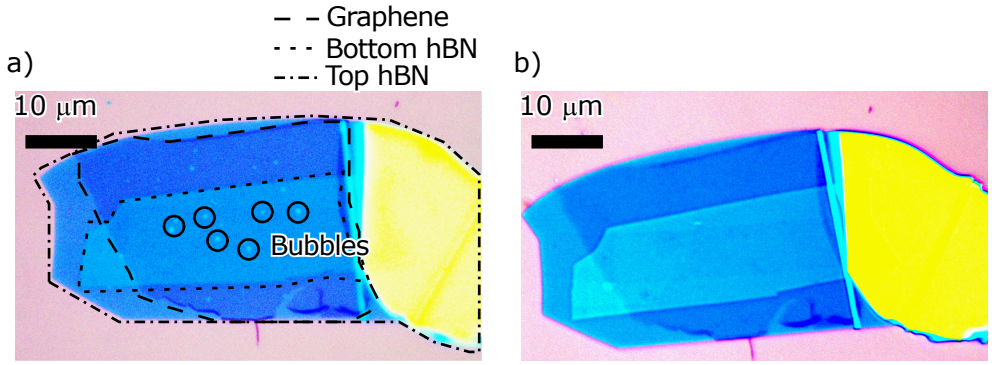

FIGURE 6.6: The impurities, also known as the bubble, are removed after vacuum annealing at 500 °C. Dashed lines represent, dash-dotted lines represent, and dotted lines represent monolayer graphene, top hBN layer, and bottom hBN layer, respectively. Circles represent bubbles between layers. Before annealing a) and after annealing b). The bubbles are removed after annealing.

6.2.3 Hall Bar Design

The hBN/graphene/hBN stack is etched to design in reactive ion etcher using plasma generated from O_2 and CF_4 gases. The details are as follows:

1. The Hall bar is patterned with electron beam lithography and developed [Fig. 6.7 a)]
2. The designed Hall bar is cleaned of organic impurities using oxygen plasma.
3. Etch the top hBN layer and graphene layer using CF_4 and O_2 plasma.

FIGURE 6.7: Hall bar etching process of hBN/graphene/hBN stack.

6.2.4 One-dimensional Contact

We contact the hBN/graphene/hBN along the 1D graphene edge [146]. This contact is a well-known method to avoid polymers and contaminate the layer interfaces, causing bubbles and wrinkles. The details are as follows:

1. Contact-lead, slightly covering the edge of the stack, is patterned with electron beam lithography.

2. Etch the top hBN layer and graphene layer using CF_4 and O_2 plasmas.
3. Metal leads are deposited by electron beam evaporation to make electrical contact.

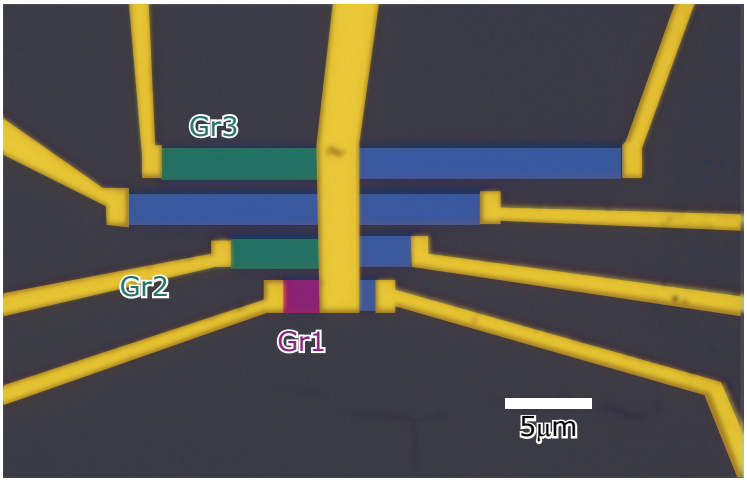

FIGURE 6.8: False-color optical image of samples. The width of the samples is 1.9 μm. In this thesis, only three graphenes are referred to as the Gr1, Gr2, and Gr3. The length of each sample is 2, 5, and 9 μm, respectively. We argue about the current noise on the Gr1 sample.

6.3 Measurement Setup

Figure 6.9 shows a schematic description of the measurement setup. The measurement is performed at 1.5 K using Kelvinox 400 (Oxford Instruments). We performed the quantum Hall effect to the using a magnetic field applied perpendicularly to the sample. The magnetic field is varied from 0 to 11 T. We inserted a load resistor, 120 kΩ at room temperature, to apply the bias voltage and current simultaneously. We measured the conductance with a standard lock-in technique to apply an ac modulation of 0.1 V. The current is under 1 μA due to the load resistor. As the source, SR830 (Stanford Research Systems) for the lock-in amplifier, Yokogawa 7651 (Yokogawa) for the dc source, and Multimeter 2000 (Keithley) for the bias dc meter are used.

The three samples are connected in parallel. Figure 6.9 shows that only one sample, Gr1, is connected to the dc source, and the other samples are disconnected. Because all samples have their ac ground (20 nF at 4 K station), they are always in an equilibrium state when disconnected. Thus, the current noise from the samples is expressed as

$$S^V_{\text{meas}} = A^2 \left(S^V_{\text{Gr1,thermal}} + S^V_{\text{Gr2,thermal}} + S^V_{\text{Gr3,thermal}} + S^V_{\text{Gr1, Excess}} \right), \quad (6.1)$$

where S^V_{meas} is the measured voltage noise, A is the total gain of the amplifier, $S^V_{\text{Gr1,thermal}}$, $S^V_{\text{Gr2,thermal}}$, and $S^V_{\text{Gr3,thermal}}$ are the thermal noise at Gr1, Gr2, and

Gr3, respectively, and $S^{V}_{\mathrm{Gr1,Excess}}$ is the excess noise due to the bias at the Gr1.

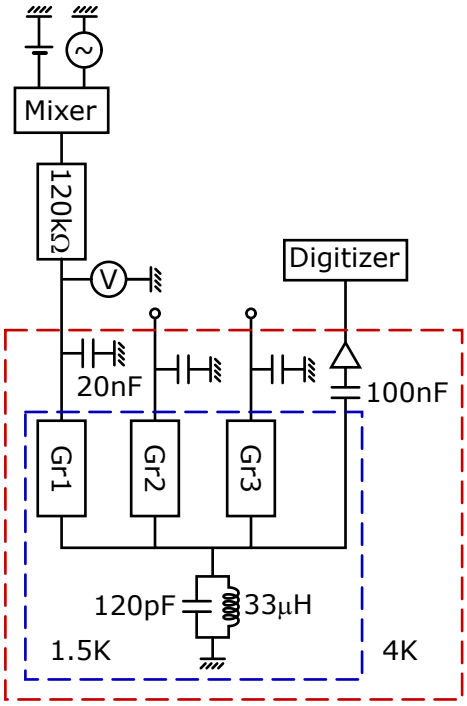

FIGURE 6.9: Schematic diagram of the measurement setup.

6.4 Results and Discussion

Hereafter, we estimated only the Gr1 sample because we did not observe the well-quantized resistance for the other samples. The temperature of the sample is about 1.5 K.

6.4.1 Zero-bias Conductance Measurement of Samples

Figure 6.10 a) shows the two-terminal resistance, R, as a function of the gate voltage, V_{g}, for the sample at zero tesla. Figure 6.10 b) shows the mobility being found to be $\mu > 2 \times 10^3 \mathrm{cm}^2/\mathrm{Vs}$. We performed a calculation based on the Drude model to obtain the mobility.

The conductivity based on the Drude model can be expressed as

$$\sigma = ne\mu = C_{\mathrm{BG}} \left| V_{\mathrm{g}} - V_{\mathrm{CNP}} \right| \mu. \tag{6.2}$$

Here, the V_{CNP} is the gate voltage at the charge neutrality point (CNP), and the C_{BG} is the capacitance of the back gate, including the bottom hBN. We

calculated the capacitance,

$$\begin{aligned}(C_{\mathrm{BG}})^{-1} &= (C_{\mathrm{SiO_2}})^{-1} + (C_{\mathrm{hBN}})^{-1} \\ &= \left(\varepsilon_r^{\mathrm{SiO_2}}\varepsilon_o \frac{1}{d_{\mathrm{SiO_2}}}\right)^{-1} + \left(\varepsilon_r^{\mathrm{hBN}}\varepsilon_o \frac{1}{d_{\mathrm{hBN}}}\right)^{-1},\end{aligned}$$

where the ε_o is the vacuum permittivity, the $\varepsilon_r^{\mathrm{SiO_2}}$ is the relative permittivity of the SiO_2 ($= 3.9$), the $\varepsilon_r^{\mathrm{hBN}}$ is the relative permittivity of the hBN ($= 3.2$), $d_{\mathrm{SiO_2}}$ is the thickness of the SiO_2 ($= 285$ nm), and d_{hBN} is the thickness of the bottom hBN ($= 4$ nm). The mobility is obtained by differentiating Eq. (6.2),

$$\left|\frac{d\sigma}{dV_{\mathrm{g}}}\right| = C_{\mathrm{BG}}\mu \rightarrow \mu = \frac{1}{C_{\mathrm{BG}}}\left|\frac{d\sigma}{dV_{\mathrm{g}}}\right|.$$

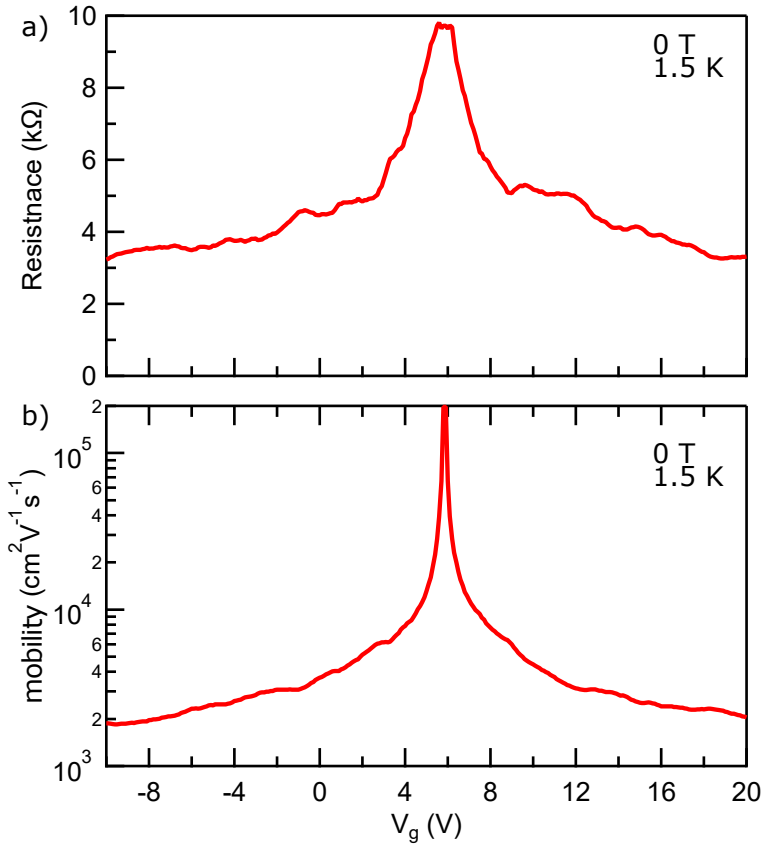

FIGURE 6.10: a) Two-terminal zero-bias resistance of Gr1 as a function of gate voltage, V_{g}, at 1.5 K and zero tesla. b) Mobility is over 2×10^3 cm^2/Vs. The mobility may be underestimated because of the short sample length, 2 μm. The mobility of Gr3, which has a 9 μm of the sample length, is over 6×10^3 cm^2/Vs (not shown here). Some conductance fluctuations may be caused by defects of impurities.

The charge neutrality point (CNP) is shifted to $V_{\mathrm{g}} = +5$ V. It is well known that the carrier density in graphene is affected by adsorbate, such

as defects [147, 148] or water molecular [149, 150], on the SiO_2 substrate. All resistance of samples has fluctuation, which may be caused by defects or impurities.

Fig. 6.11 b) shows the evolution of conductance as a function of V_g and magnetic field B. The graphene has the four-fold degeneracy of the quantum Hall states with $\nu = \pm 4\,(|n| + 1/2)$, where n is the Landau-level index. The conductance at filling factor ν is $G(V_g) = \nu e^2/h$. The electron density is expressed as $n(B) = B\nu/\varphi_0$, where $\varphi_0 = h/e$ is the magnetic flux quantum. The quantum Hall plateaus would appear linearly with the slope of the $dn/dB = \nu/\varphi_0$ [151]. The black dash lines are the slope of the ν/φ_0, with $\nu = -6, -2, +2$, and $+6$. The carrier density n_e is here calculated from Eq. (6.2). The yellow color implies that $|\nu| = 2$ regime which is the zero mode Landau-level, $n = 0$. We observed the different Landau-level by varying V_g, and we enlarged quantum Hall plateau widths by applying higher magnetic field. We only discussed the $|\nu| = 2$ with a high magnetic field since the conductance at $|\nu| = 6$ regimes and at low magnetic field regimes fluctuates.

Fig. 6.11 a) shows the cross-section of the bottom panel of Fig. 6.11 at 3, 5, and 8 T. We observed the well-quantized conductance, $2e^2/h \simeq 1/12.9\,\mathrm{k}\Omega$, while the plateau of the conductance at $|\nu| = 6$ unmatched with the $6e^2/h$. The cross-sections of the slope of the $2/\varphi_0$ and the three magnetic fields are marked as up-triangles, and the cross-section of the slope of the $6/\varphi_0$ is shown as down-triangles. The deviation at $\nu = \pm 6$ is because of the mixing of the longitudinal and transverse conductivity [152]. We estimated the contact resistance of the sample, about 100 Ω, from the difference of $h/2e^2$. The contact resistance is sufficiently low to measure for this measurement.

6.4.2 Conductance and Noise at Quantum Hall Effect Breakdown

Hereafter, we assume that the $1/f$ noise is sufficiently damped because the resonance peak is on the megahertz scale. We investigated the QHEBD of the two-terminal sample. Figure 6.12 a) shows $G(I_{sd})$ as a function of I_{sd} at 8 T for the vicinity of $\nu = -2$. The curve shows an abrupt conductance decreases from $2e^2/h$ at $I_{sd} \simeq -7\,\mu$A (as shown in Fig. 6.12 dash-dotted line). I_c is defined as the I_{sd} value where the difference of the conductance $\Delta G\,(I_{sd}) = |G(0) - G(I_{sd})|$ exceeds $0.05e^2/h$ [72]. We define the "QHE regime", $|I_{sd}| < |I_c|$, and "Breakdown regime", $|I_c| < |I_{sd}|$. We estimated the noise spectral density using Eqs. (4.2), and (4.3). Each colored triangle in Fig. 6.12 b) corresponds to the noise spectral density in the inset, respectively. Before the breakdown regime, the peak of the S^V_{meas} increases [Fig. 6.12 b)]. In the breakdown regime, S^V_{meas} increases sharply.

To estimate the QHEBD, we bias the source-drain current of our sample in the lines corresponding to the filling factor vicinity of $|\nu| = 2$ with dc current (I_{sd}) and a small ac current (less 1 μA) at a fixed magnetic field, 8 T. We observed the breakdown regime at $|\nu| \simeq 2$ starts, where $E_c = 45\,\mathrm{kV/m}$ ($I_c = -7$ μA), which is a higher breakdown electric field than the GaAs/AlGaAs case ($E_c = 0.2 \sim 3.5\,\mathrm{kV/m}$) [72–74]. The critical electric field in the works of Yang

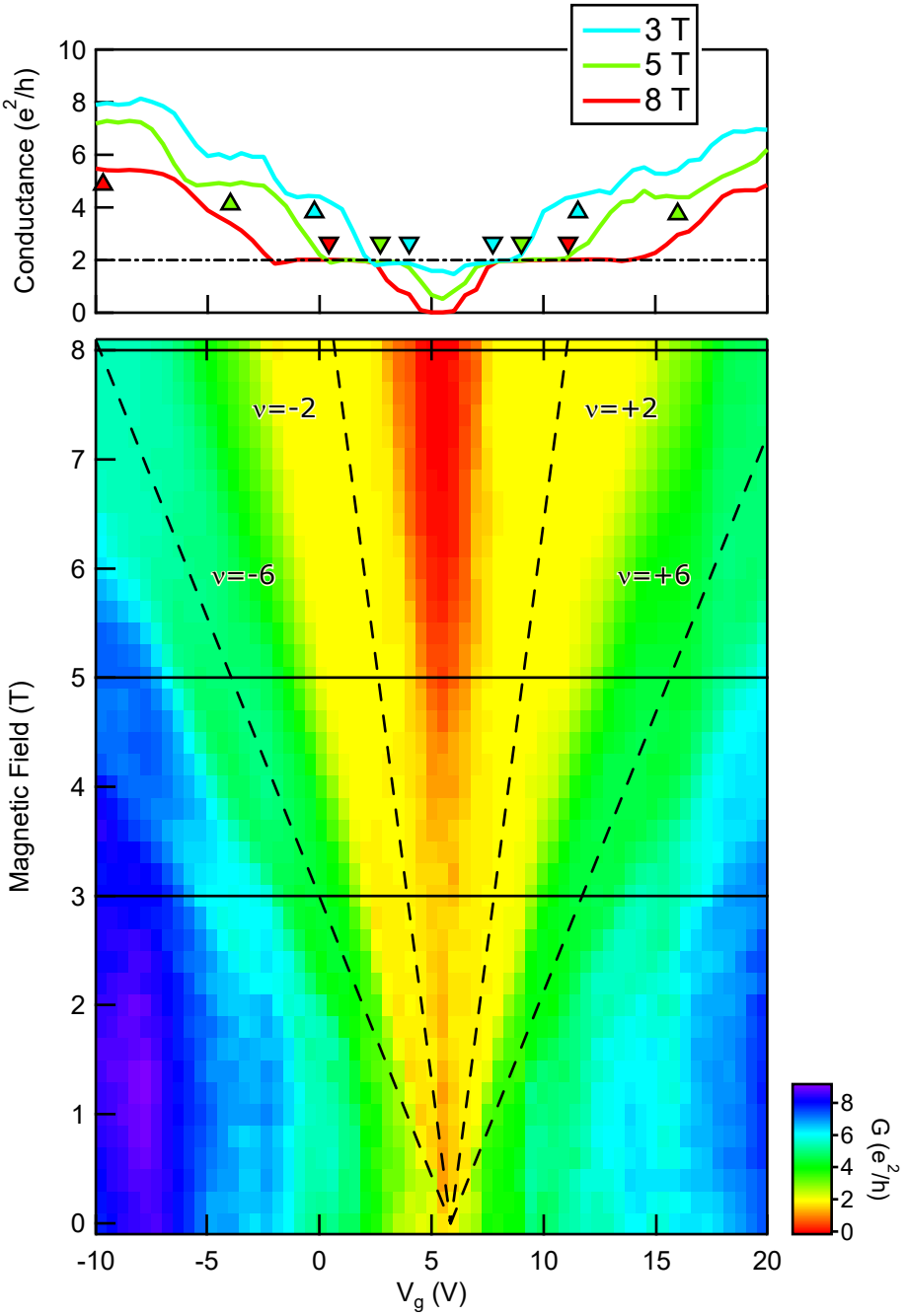

FIGURE 6.11: Landau fan diagram of Gr1. It has a well-quantized conductance at $|\nu| = 2$ regimes. The black dash lines are the slope of the ν/φ_0 for $\nu = \pm 2$ and ± 6. Upper panel; the cross-section of the conductance at 3, 5, and 8 T.

et al. is about 1.3×10^6 V/m [142] at 4 K and 7 T, and in the works of Laitinen *et al.* is about 20 kV/m at 10 mK and 5.6 T [141]. Both are much larger than the case of the GaAs/AlGaAs. We measured the current noise by focusing on the red, black, and blue lines that correspond to $|\nu| < 2$, $|\nu| \simeq 2$, and $|\nu| > 2$, respectively.

The S^V_{meas} gradually increases from the breakdown regime. The gentle

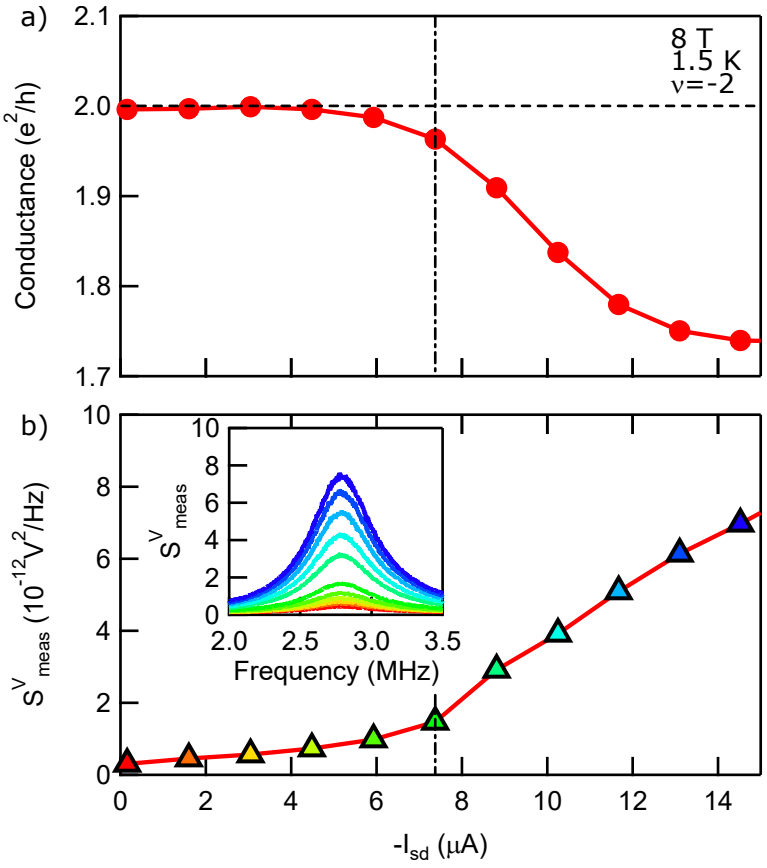

FIGURE 6.12: a) Conductance of the device as a function of I_{sd}. b) Peak of S^V_{meas} as a function of I_{sd}. Inset: noise spectral density at a resonant peak at 2.75 MHz. Each color corresponds to the colored triangles in b).

increases in the noise are characteristics of the graphene sample, while the increases in the GaAs/AlGaAs sample are abrupt [72–74]. The increase in the voltage noise corresponds to the increase in the temperature of the electrons. The details will be discussed later.

Carrier Density Dependence

Here, we discuss the conductance and current noise in two regimes: the p-type and n-type regimes.

- p-type Regime
  Figure 6.13 a) shows the colorscale plot of G as a function of I_{sd} for the p-type regime. We observed the triangular behavior as a function of V_g. The black dashed lines are guides to the eye. The QHEBD regime is almost symmetric regarding $I_{sd} = 0$. The behavior is one of the reasons for QHEBD, which implies that the inter-, and intra- Landau level scattering occur [58, 137, 153].

  We checked that the QHEBD occurs at almost the same value of I_c independent of the direction of the electron injecting source. For the $|\nu| < 2$ regime, the conductance decreases when the quantum Hall

regime breaks down, as shown in Fig. 6.13 b). For the $|\nu| > 2$ regime, the conductance increases at the QHEBD regime. These phenomena have been explained theoretically to occur as the injected electrons from the hotspot of the Ohmic contact collapse the channel in the sample due to puddles of localized electrons [154]. The experimental results may be explained by the theory.

We measured the current noise at the three regimes: the red, black, and blue lines, as shown in Fig 6.13 c). We only argue the current noise as a function of $-I_{sd}$. The current noises for all regimes increase before the QHEBD regime. While the conductance differs between the carrier density, the current noise has almost the same appearance for those regimes.

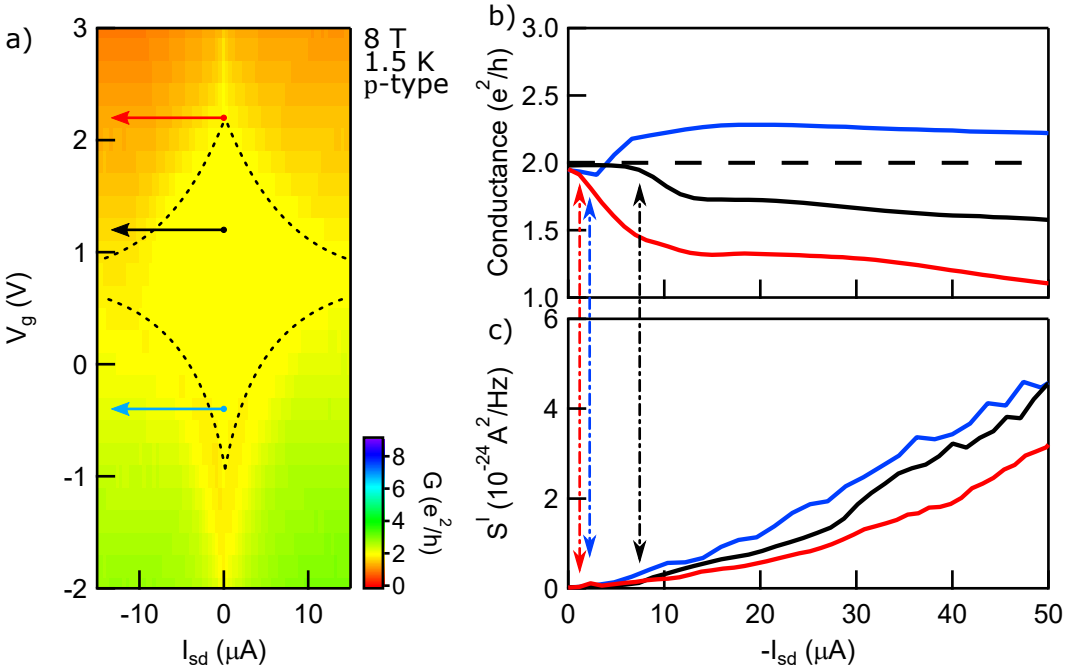

FIGURE 6.13: a) Colorscale plot of G as a function of I_{sd} for the p-type regime at 8 T. The black-dashed lines on the colorscale plot mark the QHEBD region. b) Conductance measurement for the three regimes: $|\nu| < 2$, $|\nu| \simeq 2$, and $|\nu| > 2$, which correspond to the red, black, and blue lines in a). c) Current noise measurement for the three regimes for the same three regimes. The dash-dotted arrows imply when the quantum Hall regimes break down.

- n-type Regime
  Figure 6.14 a) shows the colorscale plot of G as a function of I_{sd} for the n-type regime similar to Fig. 6.13. The triangular behavior also appears in the n-type regime with slightly differed shapes. The increases and decreases in the conductance are observed similar to the p-type regimes.

The current noises for the n-type regime are much larger than those of the p-type regimes. We think the reason is that the n-type regime is applied much higher V_g than the p-type regime. The high V_g may fluctuate the impurities in the Si substrate. S^I may include extrinsic noise at the n-type regime. We did not observe any difference in the noise signal for the carrier density in the same type regime.

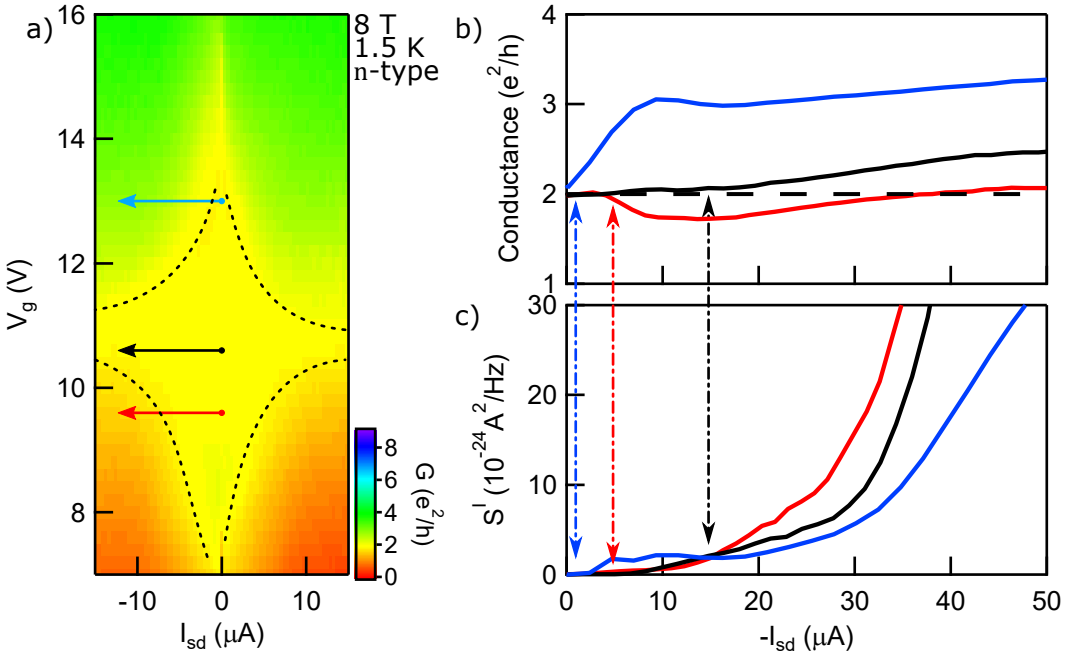

FIGURE 6.14: a) Colorscale plot of G as a function of I_{sd} for the n-type regime at 8 T. The black-dashed lines on the colorscale plot mark the QHEBD region. b) Conductance measurement for the three regimes, $|\nu| < 2$, $|\nu| \simeq 2$, and $|\nu| > 2$, which correspond to the red, black, and blue lines in a). c) Current noise measurement for the three regimes for the same three regimes. The dash-dotted arrows imply when the quantum Hall regimes break down.

Magnetic Field Dependence

We measured the conductance and the current noise at $|\nu| \simeq 2$ by varying magnetic field for 11, 8, and 5 T. Figures 6.15 a), c), e), g), i), and k) show the conductance of the device, G, as a function of $-I_{sd}$. Figures 6.15 b), d), f), h), j), and l) show the current noise at the same regime, S^I, as a function of $-I_{sd}$ in a semi-log plot. The quantized conductance, $2e^2/h$, breaks down at a I_c (dash-dotted line), as shown in Fig. 6.15 a), c), and e) for the p-type regime and g), i), and k) for the n-type regime. The decreases and increases in conductance at the p-type and n-type regimes, respectively, are due to the mismatch with the $\nu = 2$.

All excess noise increases from the QHE regime, as shown in Figs. 6.15 b), d), f), h), j), and l). The same phenomena were observed in Chida *et al.* studies, where the GaAs/AlGaAs Hall bar structure was measured. [72]. They

claimed that this precursor phenomenon occurs due to the electron tunneling process between the edge state and localized bulk state. We think our sample has many localized bulk states. Although the existence of the localized bulk state is plausible due to the fluctuation of the conductance at 0 T and excess noise at QHE regime, it was absent in conductance measurement at quantum Hall regime. The current noise for p-type and n-type regimes at the same magnetic field seems to be the qualitatively same.

To evaluate the Fano factor, $\partial S_I / (2e\partial I_{\rm sd})$, we determined the highest Fano factor as F because the excess noise is nonlinear. Figure 6.16 shows the F as a function of B in the vicinity of the $|\nu| \simeq 2$. The dashed lines are guides to the eyes. Although graphene has a much higher dc current for QHEBD than GaAs/AlGaAs, its Fano factor is much smaller ($100 < F$ at the GaAs/AlGaAs)[74]. The results agree with the previous results by the other groups [141, 142]. Although Laitinen *et al.* showed that the Fano factor is independent of the magnetic field for a monolayer Corbino disk graphene [141], Yang *et al.* showed that it is dependent on the magnetic field for a bi-layer Hall bar graphene [142]. Our study seems similar to that of Yang *et al.*; however, they considered only backscattering current to evaluate the Fano factor. Note that the Fano factor in our study are defined by source-drain current as $\partial S^I / (2e\partial I_{\rm sd})$. Despite the three points of the data, we might claim that the Fano factor linearly depends on the magnetic field. The linear dependence of the Fano factor agrees with the previous work [142].

Electron Temperature

We plotted S^I as a function of $I_{\rm sd}$ [in Fig. 6.15 b), d), f), h), j), and l)] in a log-log scale because of its nonlinearity. Figure 6.17 shows the current noise for vicinity of the $\nu = -2$ and $\nu = 2$ at 5, 8, and 11 T. In the vicinity of the $|\nu| = 2$, the S^I produces the $I_{\rm sd}^2$-dependent increase. We assume that the current noise increases due to Joule heating from the electron collision with the lattice.

We showed the electron temperature for the QHEBD regime. The electron temperature is expressed as

$$T_e = \frac{S^I}{4k_{\rm B}G} \tag{6.3}$$

[see Eq. (6.1)]. Figure 6.18 shows the conductance and the electron temperature at 8 T. The electron temperature for both regimes sharply increases from the breakdown region. While the electron temperature increases up to about 400 K in the vicinity of $\nu = 2$, it increases up to about 7000 K in the vicinity of $\nu = +2$. Note that the electron temperature does not mean the lattice temperature; it corresponds to the carrier temperature.

Our result agrees with the previous result that the interaction of the localized puddle state occurs with increases of the current noise at the precursor regime [72]. We assumed that our sample has localized puddle states, which occur during the process of electrons tunnelling between the edge state and localized puddle. We speculated that the process induces during the heating of the electrons. The results support the assumption of the BSEH model. The

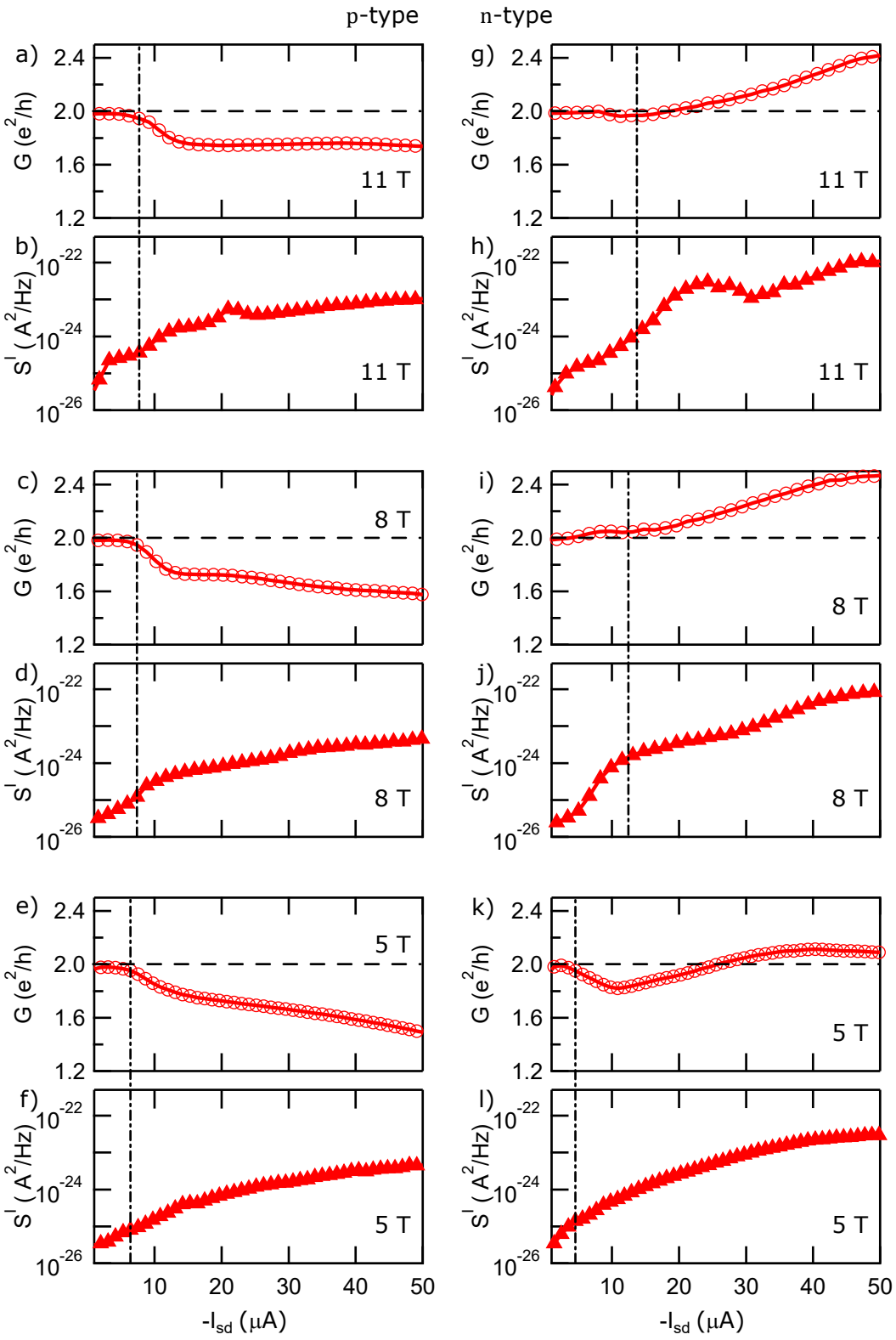

FIGURE 6.15: Conductance and the current noise vicinity of $\nu \simeq -2$ as a function of $-I_{sd}$ [a)∼f)], and the vicinity of $\nu \simeq 2$ [g)∼l)]. The dash line implies $2e^2/h$. The quantized conductance breaks down at a I_c (dash-dotted line).

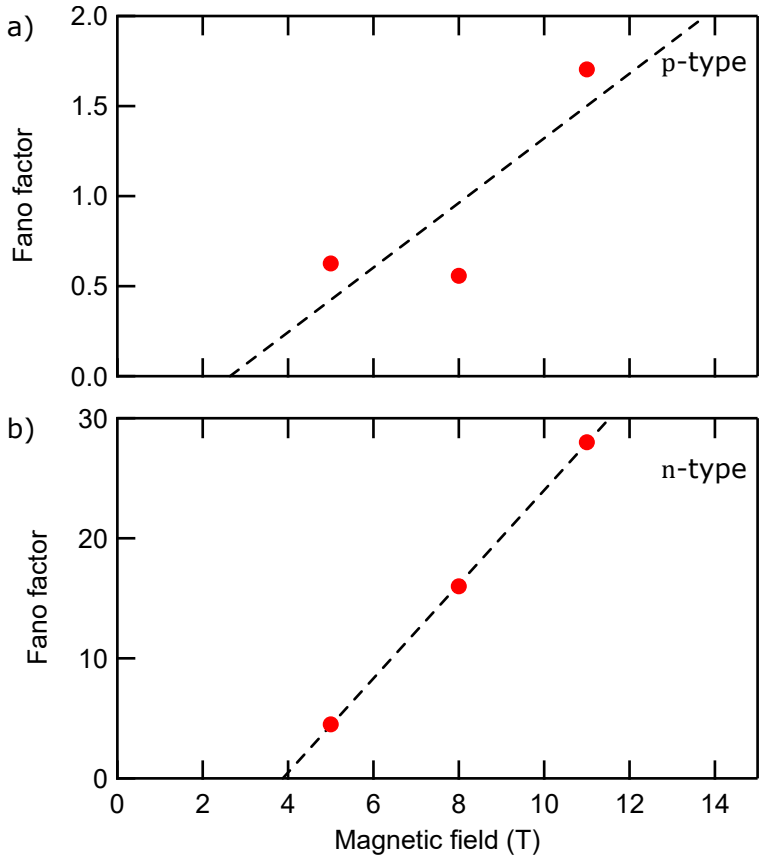

FIGURE 6.16: Fano factor as a function of the magnetic field at p-type regime a) and at n-type regime b). F is determined as the maximum value of the $\partial S^I / (2e\partial I_{\mathrm{sd}})$ because the excess noise exhibits nonlinear behaviour. The dashed line is a guide to the eyes.

BSEH model claims that QHEBD occurs when the bounded electrons collide with the accelerated electrons [59].

6.5 Summary

We conducted the current noise measurements for a monolayer graphene in a non-equilibrium quantum Hall effect regime by varying the magnetic field and the carrier density. From this study, we try to reveal the dominant process of graphene in a non-equilibrium quantum Hall effect regime.

We observed the breakdown of the quantized conductance and the excess noise. We suggested that the bootstrap electron heating model is dominant from the increases in the electron temperature. Further experimental study of QHEBD for the various shapes of samples would clarify the QHEBD mechanisms. One of the examples is the sample length dependence. The experimental conductance measurement has been reported that the quantum Hall effect drastically breaks down when the detector is far from the source [63]. We believe that similar phenomena would occur: the higher excess noise is

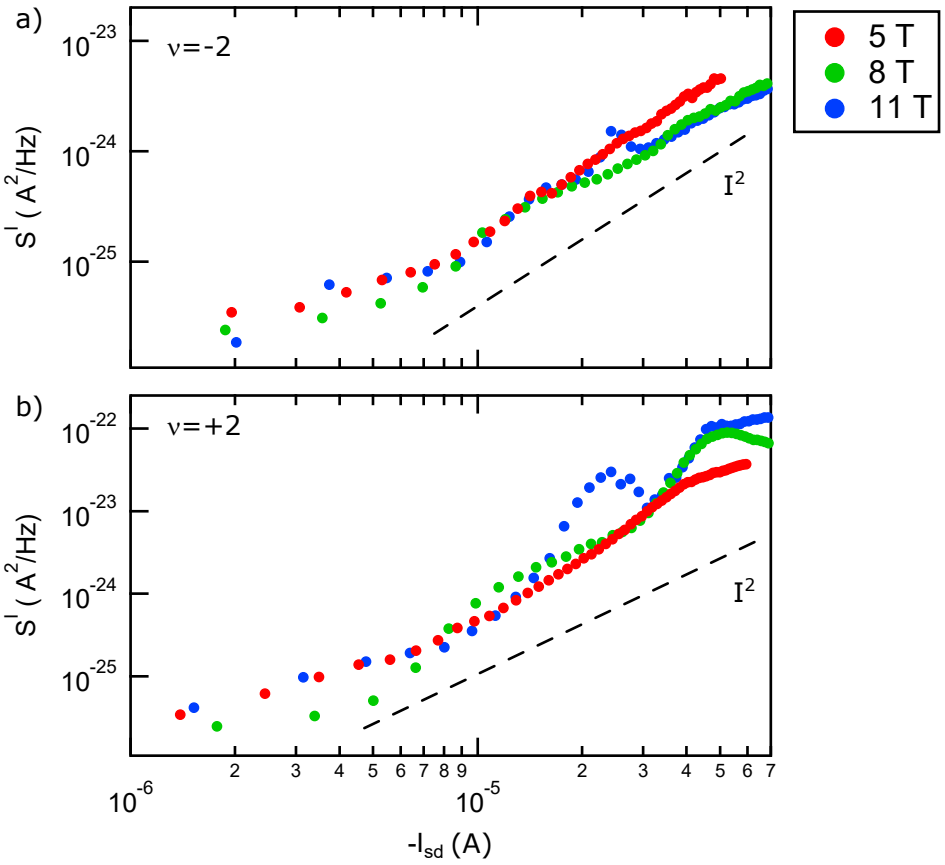

FIGURE 6.17: Log-log plot of the Figs. 6.15 b), d), f), h), j), and l).

measured when the detector is far from the source. It would be correlated with the avalanche phenomena in the classical sandpile model [155].

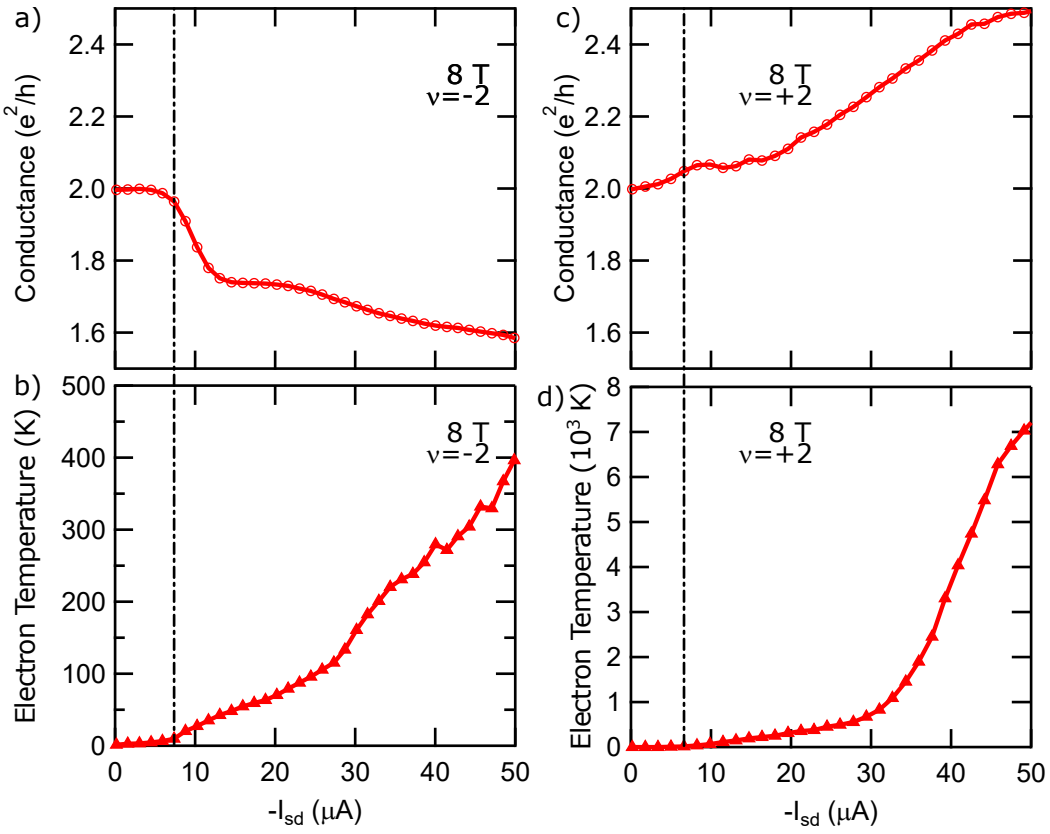

FIGURE 6.18: Conductance and electron temperature as a function of $-I_{\mathrm{sd}}$ at 8 T.

Chapter 7

Conclusion

We considered the mesoscopic device measuring the current noise in this Thesis. We investigated the current noise from two points of view: application and physical properties. We developed the noise measurement system from an application point of view and researched the current noise to investigate the quantum Hall effect breakdown of graphene.

The first achievement was the development of the cryogenic amplifier to measure the high-resolution current noise signal. We successfully measured the higher resolution of the noise signal than the previous reports [12] using the GaAs/AlGaAs HEMT. The results may contribute to probing novel mesoscopic physics, such as anyonic correlations in fractional quantum Hall system [13, 14] and violation of Bell inequalities in an electronic interferometer [15].

The second achievement was current noise measurement in both carrier types, *p*-type and *n*-type, to investigate the quantum Hall effect breakdown of graphene. We fabricated a monolayer graphene Hall bar and observed the excess current noise in the quantum Hall effect breakdown regime. Consequently, we speculated that the results, such as increase electron temperature, support the bootstrap electron heating model. We believed that the results for measuring the current noise would help a deep understanding of the quantum Hall effect breakdown phenomena. The results tell the importance of studying the quantum Hall effect breakdown phenomena on graphene using the current noise.

As we mentioned above, the current noise has useful physical information of the mesoscopic sample. The information does not appear in a conductance measurement only. Developing a cryogenic amplifier may evolve considering the electronic circuits or HEMT optimization. The details of the quantum Hall effect phenomena will be revealed by measuring the various shapes of the graphene devices.

Bibliography

1. V. Klitzing, K., Dorda, G. & Pepper, M. New Method for High-Accuracy Determination of the Fine-Structure Constant Based on Quantized Hall Resistance. *Physical Review Letters* **45,** 494–497 (1980).
2. Landauer, R. Solid-state shot noise. *Physical Review B* **47,** 16427–16432 (1993).
3. Blanter, Y. & Büttiker, M. Shot noise in mesoscopic conductors. *Physics Reports* **336,** 1–166 (2000).
4. Martin, T. Noise in mesoscopic physics. *les Houches Session LXXXI, H. Bouchiat et. al. eds. (Elsevier 2005).* arXiv: `cond-mat/0501208 [cond-mat.mes-hall]` (Jan. 10, 2005).
5. Saminadayar, L., Glattli, D. C., Jin, Y. & Etienne, B. Observation of the $e/3$ Fractionally Charged Laughlin Quasiparticle. *Physical Review Letters* **79,** 2526–2529 (1997).
6. De Picciotto, R. *et al.* Direct observation of a fractional charge. *Nature* **389,** 162–164 (1997).
7. Reznikov, M., de Picciotto, R., Griffiths, T. G., Heiblum, M. & Umansky, V. Observation of quasiparticles with one-fifth of an electron's charge. *Nature* **399,** 238–241 (1999).
8. Hashisaka, M., Ota, T., Muraki, K. & Fujisawa, T. Shot-Noise Evidence of Fractional Quasiparticle Creation in a Local Fractional Quantum Hall State. *Physical Review Letters* **114,** 056802 (2015).
9. Zarchin, O., Zaffalon, M., Heiblum, M., Mahalu, D. & Umansky, V. Two-electron bunching in transport through a quantum dot induced by Kondo correlations. *Physical Review B* **77,** 241303 (2008).
10. Yamauchi, Y. *et al.* Evolution of the Kondo Effect in a Quantum Dot Probed by Shot Noise. *Physical Review Letters* **106,** 176601 (2011).
11. Ferrier, M. *et al.* Universality of non-equilibrium fluctuations in strongly correlated quantum liquids. *Nature Physics* **12,** 230–235 (2016).
12. DiCarlo, L. *et al.* System for measuring auto- and cross correlation of current noise at low temperatures. *Review of Scientific Instruments* **77,** 073906 (2006).
13. Wilczek, F. Magnetic Flux, Angular Momentum, and Statistics. *Physical Review Letters* **48,** 1144–1146 (1982).
14. Bartolomei, H. *et al.* Fractional statistics in anyon collisions. *Science* **368,** 173–177 (2020).

15. Samuelsson, P., Sukhorukov, E. V. & Büttiker, M. Two-Particle Aharonov-Bohm Effect and Entanglement in the Electronic Hanbury Brown–Twiss Setup. *Physical Review Letters* **92,** 026805 (2004).
16. Datta, S. *Electronic Transport in Mesoscopic Systems* 396 pp. ISBN: 0521599431 (Cambridge University Press, Sept. 15, 2014).
17. Mimura, T., Hiyamizu, S., Fujii, T. & Nanbu, K. A New Field-Effect Transistor with Selectively Doped GaAs/n-Al x Ga 1- x As Heterojunctions. *Japanese Journal of Applied Physics* **19,** L225–L227. ISSN: 0021-4922 (1980).
18. Mimura, T. The early history of the high electron mobility transistor (HEMT). *IEEE Transactions on Microwave Theory and Techniques* **50,** 780–782. ISSN: 00189480 (2002).
19. Neto, A. H. C., Guinea, F., Peres, N. M. R., Novoselov, K. S. & Geim, A. K. The electronic properties of graphene. *Reviews of Modern Physics* **81,** 109–162 (2009).
20. Partoens, B. & Peeters, F. M. From graphene to graphite: Electronic structure around theKpoint. *Physical Review B* **74,** 075404 (2006).
21. Mucha-Kruczyński, M. *et al.* Characterization of graphene through anisotropy of constant-energy maps in angle-resolved photoemission. *Physical Review B* **77,** 195403 (2008).
22. Sarma, S. D., Adam, S., Hwang, E. H. & Rossi, E. Electronic transport in two-dimensional graphene. *Reviews of Modern Physics* **83,** 407–470 (2011).
23. Goerbig, M. O. Electronic properties of graphene in a strong magnetic field. *Reviews of Modern Physics* **83,** 1193–1243 (2011).
24. Bena, C. & Montambaux, G. Remarks on the tight-binding model of graphene. *New Journal of Physics* **11,** 095003 (2009).
25. DiVincenzo, D. P. & Mele, E. J. Self-consistent effective-mass theory for intralayer screening in graphite intercalation compounds. *Physical Review B* **29,** 1685–1694 (1984).
26. Semenoff, G. W. Condensed-Matter Simulation of a Three-Dimensional Anomaly. *Physical Review Letters* **53,** 2449–2452 (1984).
27. Novoselov, K. S. *et al.* Two-dimensional gas of massless Dirac fermions in graphene. *Nature* **438,** 197–200 (2005).
28. Zhang, Y., Tan, Y.-W., Stormer, H. L. & Kim, P. Experimental observation of the quantum Hall effect and Berry's phase in graphene. *Nature* **438,** 201–204 (2005).
29. Deacon, R. S., Chuang, K.-C., Nicholas, R. J., Novoselov, K. S. & Geim, A. K. Cyclotron resonance study of the electron and hole velocity in graphene monolayers. *Physical Review B* **76,** 081406 (2007).
30. Jiang, Z. *et al.* Infrared Spectroscopy of Landau Levels of Graphene. *Physical Review Letters* **98,** 197403 (2007).

31. Micolich, A. Double or nothing? *Nature Physics* **9,** 530–531 (2013).
32. Büttiker, M. Quantized transmission of a saddle-point constriction. *Physical Review B* **41,** 7906–7909 (1990).
33. Weissman, M. B. 1fnoise and other slow, nonexponential kinetics in condensed matter. *Reviews of Modern Physics* **60,** 537–571 (1988).
34. Connor, J. On the analytical description of resonance tunnelling reactions. *Molecular Physics* **15,** 37–46 (1968).
35. Goerbig, M. O. Quantum Hall Effects. arXiv: `0909.1998 [cond-mat.mes-hall]` (Sept. 10, 2009).
36. Hall, E. H. On a New Action of the Magnet on Electric Currents. *American Journal of Mathematics* **2,** 287 (1879).
37. Janssen, T. J. B. M., Tzalenchuk, A, Lara-Avila, S, Kubatkin, S & Fal'ko, V. I. Quantum resistance metrology using graphene. *Reports on Progress in Physics* **76,** 104501 (2013).
38. Klaß, U., Dietsche, W., von Klitzing, K. & Ploog, K. Imaging of the dissipation in quantum-Hall-effect experiments. *Zeitschrift für Physik B Condensed Matter* **82,** 351–354 (1991).
39. Zhang, Y. *et al.* Landau-Level Splitting in Graphene in High Magnetic Fields. *Physical Review Letters* **96,** 136806 (2006).
40. Giesbers, A. J. M. *et al.* Quantum-Hall Activation Gaps in Graphene. *Physical Review Letters* **99,** 206803 (2007).
41. Giesbers, A. J. M. *et al.* Gap opening in the zeroth Landau level of graphene. *Physical Review B* **80,** 201403 (2009).
42. Ebert, G, von Klitzing, K, Ploog, K & Weinmann, G. Two-dimensional magneto-quantum transport on GaAs-AlxGa1-xAs heterostructures under non-ohmic conditions. *Journal of Physics C: Solid State Physics* **16,** 5441–5448 (1983).
43. Cage, M. E. *et al.* Dissipation and Dynamic Nonlinear Behavior in the Quantum Hall Regime. *Physical Review Letters* **51,** 1374–1377 (1983).
44. Kuchar, F., Bauer, G., Weimann, G. & Burkhard, H. Non-equilibrium behaviour of the two-dimensional electron gas in the quantized Hall resistance regime of GaAs/Al0.3Ga0.7As. *Surface Science* **142,** 196–202 (1984).
45. Komiyama, S., Takamasu, T., Hiyamizu, S. & Sasa, S. Breakdown of the quantum Hall effect due to electron heating. *Solid State Communications* **54,** 479–484 (1985).
46. Kawaji, S. *et al.* Breakdown of the Quantum Hall Effect in GaAs/AlGaAs Heterostructures Due to Current. *Journal of the Physical Society of Japan* **63,** 2303–2313 (1994).
47. Von Klitzing, K. in *The Quantum Hall Effect: Poincaré Seminar 2004* (eds Douçot, B., Pasquier, V., Duplantier, B. & Rivasseau, V.) 1–21 (Birkhäuser Basel, Basel, 2005). ISBN: 978-3-7643-7393-1.

48. Von Klitzing, K. Metrology in 2019. *Nature Physics* **13,** 198–198 (2017).

49. Heinonen, O., Taylor, P. L. & Girvin, S. M. Electron-phonon interactions and the breakdown of the dissipationless quantum Hall effect. *Physical Review B* **30,** 3016–3019 (1984).

50. Eaves, L, Guimaraes, P. S. S. & Portal, J. C. Hot-electron magnetophonon spectroscopy on micron- and sub-micron-size n^+nn^+GaAs structures. *Journal of Physics C: Solid State Physics* **17,** 6177–6190 (1984).

51. Eaves, L & Sheard, F. W. Size-dependent quantised breakdown of the dissipationless quantum Hall effect in narrow channels. *Semiconductor Science and Technology* **1,** 346–349 (1986).

52. Bliek, L. *et al.* Breakdown of dissipationless quantum hall conduction in narrow channels. *Surface Science* **196,** 156–164 (1988).

53. Balaban, N. Q., Meirav, U., Shtrikman, H. & Levinson, Y. Scaling of the critical current in the quantum Hall effect: A probe of current distribution. *Physical Review Letters* **71,** 1443–1446 (1993).

54. Balaban, N. Q., Meirav, U. & Shtrikman, H. Crossover between different regimes of current distribution in the quantum Hall effect. *Physical Review B* **52,** R5503–R5506 (1995).

55. Makarovsky, O *et al.* Quantum Hall effect breakdown: can the bootstrap heating and inter-Landau-level scattering models be reconciled? *Physica E: Low-dimensional Systems and Nanostructures* **12,** 178–181 (2002).

56. Guimaraes, P., Eaves, L., Sheard, F., Portal, J. & Hill, G. Resonant magnetoresistance measurements in short ($\sim 1\ \mu$m) n^+nn^+GaAs structures: Investigation of the electric field dependence of quasi-elastic inter-Landau level scattering processes. *Physica B+C* **134,** 47–52 (1985).

57. Bliek, L *et al.* Critical current density for the dissipationless quantum Hall effect. *Semiconductor Science and Technology* **1,** 110–112 (1986).

58. Kirtley, J. R. *et al.* Low-voltage breakdown of the quantum Hall state in a laterally constricted two-dimensional electron gas. *Physical Review B* **34,** 1384–1387 (1986).

59. Komiyama, S. & Kawaguchi, Y. Heat instability of quantum Hall conductors. *Physical Review B* **61,** 2014–2027 (2000).

60. Komiyama, S. & Nii, H. Nonequilibrium electron distribution and nonlocal resistance in a two-dimensional electron gas at high magnetic fields. *Physica B: Condensed Matter* **184,** 7–16 (1993).

61. Takamasu, T., Komiyama, S., Hiyamizu, S. & Sasa, S. Effect of finite electric field on the quantum Hall effect. *Surface Science* **170,** 202–208 (1986).

62. Kawaguchi, Y. *et al.* Disappearance of the Breakdown of Quantum Hall Effects in Short Devices. *Japanese Journal of Applied Physics* **34,** 4309–4312 (1995).

63. Komiyama, S., Kawaguchi, Y., Osada, T. & Shiraki, Y. Evidence of Nonlocal Breakdown of the Integer Quantum Hall Effect. *Physical Review Letters* **77,** 558–561 (1996).

64. Boella, G. *et al.* Analysis of time behavior in the breakdown of the integral quantum Hall effect. *Physical Review B* **50,** 7608–7614 (1994).

65. Sagol, B. E., Nachtwei, G., von Klitzing, K., Hein, G. & Eberl, K. Time scale of the excitation of electrons at the breakdown of the quantum Hall effect. *Physical Review B* **66,** 075305 (2002).

66. Li, M.-Y. *et al.* Transition dynamics in the electrical breakdown of the quantum Hall effect. *Physical Review B* **85,** 245315 (2012).

67. Nakajima, T. & Komiyama, S. Lifetime of dissipation-less state of quantum Hall electron systems in the bistable regime. *Physica E: Low-dimensional Systems and Nanostructures* **42,** 1026–1029 (2010).

68. Kawaji, S., Hirakawa, K. & Nagata, M. Device-width dependence of plateau width in quantum Hall states. *Physica B: Condensed Matter* **184,** 17–20 (1993).

69. Alexander-Webber, J. A. *et al.* Phase Space for the Breakdown of the Quantum Hall Effect in Epitaxial Graphene. *Physical Review Letters* **111,** 096601 (2013).

70. Meziani, Y. M. *et al.* Behavior of the contacts of quantum Hall effect devices at high currents. *Journal of Applied Physics* **96,** 404–410 (2004).

71. 加藤, . < 講義ノート > メゾスコピック系の物理: 基礎から最近の話題まで. 物性研究・電子版 **3,** 1. `https://ci.nii.ac.jp/naid/120005373102/en/` (2014).

72. Chida, K. *et al.* Observation of finite excess noise in the voltage-biased quantum Hall regime as a precursor for breakdown. *Physical Review B* **87,** 155313 (2013).

73. Chida, K. *et al.* Avalanche electron bunching in a Corbino disk in the quantum Hall effect breakdown regime. *Physical Review B* **89,** 235318 (2014).

74. Hata, T., Arakawa, T., Chida, K., Matsuo, S. & Kobayashi, K. Giant Fano factor and bistability in a Corbino disk in the quantum Hall effect breakdown regime. *Journal of Physics: Condensed Matter* **28,** 055801 (2016).

75. Kohda, M. *et al.* Spin–orbit induced electronic spin separation in semiconductor nanostructures. *Nature Communications* **3,** 1 (Jan. 2012).

76. Arakawa, T. *et al.* Shot Noise Induced by Nonequilibrium Spin Accumulation. *Physical Review Letters* **114,** 016601 (2015).

77. Nakamura, S. *et al.* Nonequilibrium Fluctuation Relations in a Quantum Coherent Conductor. *Physical Review Letters* **104,** 080602 (2010).

78. Henny, M. The Fermionic Hanbury Brown and Twiss Experiment. *Science* **284,** 296–298 (1999).

79. Oliver, W. D. Hanbury Brown and Twiss-Type Experiment with Electrons. *Science* **284,** 299–301 (1999).
80. Dubois, J. *et al.* Minimal-excitation states for electron quantum optics using levitons. *Nature* **502,** 659–663 (2013).
81. Bocquillon, E. *et al.* Coherence and Indistinguishability of Single Electrons Emitted by Independent Sources. *Science* **339,** 1054–1057 (2013).
82. Balandin, A. A. Low-frequency $1/f$ noise in graphene devices. *Nature Nanotechnology* **8,** 549–555 (2013).
83. Johnson, J. B. The Schottky Effect in Low Frequency Circuits. *Physical Review* **26,** 71–85 (1925).
84. FLINN, I. Extent of the $1/f$ Noise Spectrum. *Nature* **219,** 1356–1357 (1968).
85. Schoelkopf, R. J. The Radio-Frequency Single-Electron Transistor (RF-SET): A Fast and Ultrasensitive Electrometer. *Science* **280,** 1238–1242 (1998).
86. Balandin, A. *Noise and fluctuations control in electronic devices* ISBN: 1588830055 (American Scientific Publishers, Stevenson Ranch, Calif, 2002).
87. Dutta, P. & Horn, P. M. Low-frequency fluctuations in solids:$1/f$noise. *Reviews of Modern Physics* **53,** 497–516 (1981).
88. Bernamont, J. Fluctuations de potentiel aux bornes d'un conducteur métallique de faible volume parcouru par un courant. *Annales de physique* **11,** 71–140 (1937).
89. Galperin, Y. M., Gurevich, V. L & Kozub, V. I. Disorder-Induced Low-Frequency Noise in Small Systems: Point and Tunnel Contacts in the Normal and Superconducting State. *Europhysics Letters (EPL)* **10,** 753–758 (1989).
90. Dmitriev, A. P., Levinshtein, M. E. & Rumyantsev, S. L. On the Hooge relation in semiconductors and metals. *Journal of Applied Physics* **106,** 024514 (2009).
91. Hooge, F. $1/f$ noise is no surface effect. *Physics Letters A* **29,** 139–140 (1969).
92. Xu, G. *et al.* Effect of Spatial Charge Inhomogeneity on 1/fNoise Behavior in Graphene. *Nano Letters* **10,** 3312–3317 (2010).
93. Takeshita, S. *et al.* Anomalous behavior of 1/f noise in graphene near the charge neutrality point. *Applied Physics Letters* **108,** 103106 (2016).
94. Clauss, W *et al.* Self-Organized Critical Behaviour in the Low-Temperature Impact Ionization Breakdown of p-Ge. *Europhysics Letters (EPL)* **12,** 423–428 (1990).
95. Johnson, J. B. Thermal Agitation of Electricity in Conductors. *Physical Review* **32,** 97–109. ISSN: 0031-899X (1928).
96. Nyquist, H. Thermal Agitation of Electric Charge in Conductors. *Physical Review* **32,** 110–113 (1928).

97. Muro, T. *et al.* Finite shot noise and electron heating at quantized conductance in high-mobility quantum point contacts. *Physical Review B* **93,** 195411 (2016).

98. kobayashi, K. What can we learn from noise? — Mesoscopic nonequilibrium statistical physics —. *Proceedings of the Japan Academy, Series B* **92,** 204–221 (2016).

99. Hashisaka, M. *et al.* Development of a measurement system for quantum shot noise at low temperatures. *physica status solidi (c)* **5,** 182–185 (2008).

100. Hashisaka, M *et al.* Measurement for quantum shot noise in a quantum point contact at low temperatures. *Journal of Physics: Conference Series* **109,** 012013 (2008).

101. Hashisaka, M. *et al.* Noise measurement system at electron temperature down to 20 mK with combinations of the low pass filters. *Review of Scientific Instruments* **80,** 096105 (2009).

102. Arakawa, T., Nishihara, Y., Maeda, M., Norimoto, S. & Kobayashi, K. Cryogenic amplifier for shot noise measurement at 20 mK. *Applied Physics Letters* **103,** 172104 (2013).

103. Kumar, A., Saminadayar, L., Glattli, D. C., Jin, Y. & Etienne, B. Experimental Test of the Quantum Shot Noise Reduction Theory. *Physical Review Letters* **76,** 2778–2781 (1996).

104. Sampietro, M., Fasoli, L. & Ferrari, G. Spectrum analyzer with noise reduction by cross-correlation technique on two channels. *Review of Scientific Instruments* **70,** 2520–2525 (1999).

105. Hashisaka, M. *et al.* Bolometric detection of quantum shot noise in coupled mesoscopic systems. *Physical Review B* **78,** 241303 (2008).

106. Reznikov, M., Heiblum, M., Shtrikman, H. & Mahalu, D. Temporal Correlation of Electrons: Suppression of Shot Noise in a Ballistic Quantum Point Contact. *Physical Review Letters* **75,** 3340–3343 (1995).

107. Liu, R. C., Odom, B., Yamamoto, Y. & Tarucha, S. Quantum interference in electron collision. *Nature* **391,** 263–265 (1998).

108. Roche, P. *et al.* Fano Factor Reduction on the 0.7 Conductance Structure of a Ballistic One-Dimensional Wire. *Physical Review Letters* **93,** 116602 (Sept. 2004).

109. DiCarlo, L. *et al.* Shot-Noise Signatures of 0.7 Structure and Spin in a Quantum Point Contact. *Physical Review Letters* **97,** 036810 (2006).

110. Nakamura, S. *et al.* Conductance anomaly and Fano factor reduction in quantum point contacts. *Physical Review B* **79,** 201308 (2009).

111. Nishihara, Y. *et al.* Shot noise suppression in InGaAs/InGaAsP quantum channels. *Applied Physics Letters* **100,** 203111 (2012).

112. Steinbach, A. H., Martinis, J. M. & Devoret, M. H. Observation of Hot-Electron Shot Noise in a Metallic Resistor. *Physical Review Letters* **76,** 3806–3809 (1996).

113. Henny, M., Oberholzer, S., Strunk, C. & Schönenberger, C. 1/3-shot-noise suppression in diffusive nanowires. *Physical Review B* **59,** 2871–2880 (1999).

114. Zarchin, O., Chung, Y. C., Heiblum, M., Rohrlich, D. & Umansky, V. Electron Bunching in Transport through Quantum Dots in a High Magnetic Field. *Physical Review Letters* **98,** 066801 (2007).

115. Okazaki, Y., Sasaki, S. & Muraki, K. Shot noise spectroscopy on a semiconductor quantum dot in the elastic and inelastic cotunneling regimes. *Physical Review B* **87,** 041302 (2013).

116. Gustavsson, S. *et al.* Counting Statistics of Single Electron Transport in a Quantum Dot. *Physical Review Letters* **96,** 076605 (2006).

117. Onac, E., Balestro, F., Trauzettel, B., Lodewijk, C. F. J. & Kouwenhoven, L. P. Shot-Noise Detection in a Carbon Nanotube Quantum Dot. *Physical Review Letters* **96,** 026803 (2006).

118. Safonov, S. S. *et al.* Enhanced Shot Noise in Resonant Tunneling via Interacting Localized States. *Physical Review Letters* **91,** 136801 (2003).

119. Sekiguchi, K. *et al.* Nonreciprocal emission of spin-wave packet in FeNi film. *Applied Physics Letters* **97,** 022508 (2010).

120. Arakawa, T. *et al.* Sub-Poissonian shot noise in CoFeB/MgO/CoFeB-based magnetic tunneling junctions. *Applied Physics Letters* **98,** 202103 (2011).

121. Jehl, X., Sanquer, M., Calemczuk, R. & Mailly, D. Detection of doubled shot noise in short normal-metal/ superconductor junctions. *Nature* **405,** 50–53 (2000).

122. Chida, K. *et al.* Shot noise induced by electron-nuclear spin-flip scattering in a nonequilibrium quantum wire. *Physical Review B* **85,** 041309 (2012).

123. Delattre, T. *et al.* Noisy Kondo impurities. *Nature Physics 5, 208 (2009)* **5,** 208–212. arXiv: `1010.4815 [cond-mat.mes-hall]` (Oct. 22, 2010).

124. Hashisaka, M., Ota, T., Yamagishi, M., Fujisawa, T. & Muraki, K. Cross-correlation measurement of quantum shot noise using homemade transimpedance amplifiers. *Review of Scientific Instruments* **85,** 054704 (2014).

125. Dong, Q. *et al.* Ultra-low noise high electron mobility transistors for high-impedance and low-frequency deep cryogenic readout electronics. *Applied Physics Letters* **105,** 013504 (2014).

126. Liang, Y. X., Dong, Q., Gennser, U., Cavanna, A. & Jin, Y. Input Noise Voltage Below 1 nV/Hz1/2 at 1 kHz in the HEMTs at 4.2 K. *Journal of Low Temperature Physics* **167,** 632–637 (2012).

127. Landauer, R. Spatial Variation of Currents and Fields Due to Localized Scatterers in Metallic Conduction. *IBM Journal of Research and Development* **1,** 223–231 (1957).

128. Ziel, A. V. D. & Chenette, E. in *Advances in Electronics and Electron Physics Volume 46* 313–383 (Elsevier, 1978).

129. Hooge, F. $1/f$ noise in the conductance of ions in aqueous solutions. *Physics Letters A* **33,** 169–170 (1970).

130. Schurr, J., Moser, H., Pierz, K., Ramm, G. & Kibble, B. P. Johnson–Nyquist Noise of the Quantized Hall Resistance. *IEEE Transactions on Instrumentation and Measurement* **60,** 2280–2285 (2011).

131. Schurr, J., Ahlers, F. & Callegaro, L. Noise and Correlation Study of Quantum Hall Devices. *IEEE Transactions on Instrumentation and Measurement* **62,** 1574–1580 (2013).

132. Baker, A. M. R., Alexander-Webber, J. A., Altebaeumer, T. & Nicholas, R. J. Energy relaxation for hot Dirac fermions in graphene and breakdown of the quantum Hall effect. *Physical Review B* **85,** 115403 (2012).

133. Baker, A. M. R. *et al.* Energy loss rates of hot Dirac fermions in epitaxial, exfoliated, and CVD graphene. *Physical Review B* **87,** 045414 (2013).

134. Betz, A. C. *et al.* Hot Electron Cooling by Acoustic Phonons in Graphene. *Physical Review Letters* **109,** 056805 (2012).

135. Tan, Z. *et al.* Shubnikov-de Haas oscillations of a single layer graphene under dc current bias. *Physical Review B* **84,** 115429 (2011).

136. Betz, A. C. *et al.* Supercollision cooling in undoped graphene. *Nature Physics* **9,** 109–112 (2012).

137. Singh, V. & Deshmukh, M. M. Nonequilibrium breakdown of quantum Hall state in graphene. *Physical Review B* **80,** 081404 (2009).

138. Yanık, C. & Kaya, I. Local breakdown of the quantum Hall effect in narrow single layer graphene Hall devices. *Solid State Communications* **160,** 47–51 (2013).

139. Laitinen, A., Kumar, M., Hakonen, P. & Sonin, E. Gyrotropic Zener tunneling and nonlinear IV curves in the zero-energy Landau level of graphene in a strong magnetic field. *Scientific Reports* **8,** 1 (2018).

140. Kubakaddi, S. S. Interaction of massless Dirac electrons with acoustic phonons in graphene at low temperatures. *Physical Review B* **79,** 075417 (2009).

141. Laitinen, A. *et al.* Breakdown of Zero-Energy Quantum Hall State in Graphene in the Light of Current Fluctuations and Shot Noise. *Journal of Low Temperature Physics* **191,** 272–287 (2018).

142. Yang, W. *et al.* Landau Velocity for Collective Quantum Hall Breakdown in Bilayer Graphene. *Physical Review Letters* **121,** 136804 (2018).

143. Novoselov, K. S. *et al.* Electric Field Effect in Atomically Thin Carbon Films. *Science* **306,** 666–669 (2004).

144. Novoselov, K. S. & Neto, A. H. C. Two-dimensional crystals-based heterostructures: materials with tailored properties. *Physica Scripta* **T146,** 014006 (2012).

145. Zomer, P. J., Dash, S. P., Tombros, N. & van Wees, B. J. A transfer technique for high mobility graphene devices on commercially available hexagonal boron nitride. *Applied Physics Letters* **99,** 232104 (2011).

146. Wang, L. *et al.* One-Dimensional Electrical Contact to a Two-Dimensional Material. *Science* **342,** 614–617 (2013).

147. Nistor, R. A., Kuroda, M. A., Maarouf, A. A. & Martyna, G. J. Doping of adsorbed graphene from defects and impurities in SiO2substrates. *Physical Review B* **86,** 041409 (2012).

148. Hwang, E. H., Adam, S. & Sarma, S. D. Carrier Transport in Two-Dimensional Graphene Layers. *Physical Review Letters* **98,** 186806 (2007).

149. Moser, J., Verdaguer, A., Jiménez, D., Barreiro, A. & Bachtold, A. The environment of graphene probed by electrostatic force microscopy. *Applied Physics Letters* **92,** 123507 (2008).

150. Lafkioti, M. *et al.* Graphene on a Hydrophobic Substrate: Doping Reduction and Hysteresis Suppression under Ambient Conditions. *Nano Letters* **10,** 1149–1153 (2010).

151. Bolotin, K. I., Ghahari, F., Shulman, M. D., Stormer, H. L. & Kim, P. Observation of the fractional quantum Hall effect in graphene. *Nature* **462,** 196–199 (2009).

152. Abanin, D. A. & Levitov, L. S. Conformal invariance and shape-dependent conductance of graphene samples. *Physical Review B* **78,** 035416 (2008).

153. Kirtley, J. R. *et al.* Voltage-controlled dissipation in the quantum Hall effect in a laterally constricted two-dimensional electron gas. *Physical Review B* **34,** 5414–5422 (1986).

154. Kramer, T. *et al.* Theory of the quantum Hall effect in finite graphene devices. *Physical Review B* **81,** 081410 (2010).

155. Bak, P. *How nature works : the science of self-organized criticality* ISBN: 9781475754261 (Springer New York, New York, NY, USA, 1996).

List of Publications

1. **Sanghyun Lee**, Masayuki Hashisaka, Takafumi Akiho, Kensuke Kobayashi, and Koji Muraki, "Homemade cryogenic GaAs-HEMT amplifier for current noise measurements", (submitted to *Review of Scientific Instruments*)

2. **Sanghyun Lee**, Excess noise at quantum Hall effect regime of graphene. (in preparation)

3. T. Hata, R. Delagrange, T. Arakawa, **S. Lee**, R. Deblock, H. Bouchiat, K. Kobayashi, and M. Ferrier, "Enhanced Shot Noise of Multiple Andreev Reflections in a Carbon Nanotube Quantum Dot in SU(2) and SU(4) Kondo Regimes", *Physical Review Letters* **121**, 247703 (2018).

4. Mori Watanabe, **Sanghyun Lee**, Takuya Asano, Takashi Ibe, Masashi Tokuda, Hiroki Taniguchi, Daichi Ueta, Yoshinori Okada, Kensuke Kobayashi, and Yasuhiro Niimi, "Quantum oscillations with magnetic hysteresis observed in CeTe3 thin films", *Applied Physics Letters* **117**, 072403/1-5 (2020).